

**COHERENT STRUCTURES IN THE AXISYMMETRIC
TURBULENT JET MIXING LAYER**

by

Mark N. Glauser

A Dissertation submitted to the Faculty
of the Graduate School of the State University
of New York at Buffalo in partial fulfillment
of the requirements for the degree of
Doctor of Philosophy

September 1987

TABLE OF CONTENTS

Acknowledgements	-----	i
Abstract	-----	ii
List of Figures	-----	iv
Nomenclature	-----	ix
Chapter		
1	Introduction	----- 1
2	Theory - Orthogonal Decomposition	----- 4
	2.1 The General Inhomogeneous Problem	----- 4
	2.2 Dealing With Stationary, Homogeneous or Periodic Directions	----- 6
	2.3 The Experimental Approach	----- 8
3	The Experiment	----- 11
	3.1 The Facility	----- 11
	3.2 Instrumentation	----- 15
	3.3 Calibration	----- 19
	3.4 Cross-Wire Calibration	----- 22
	3.5 Sampling Information	----- 25
4	Instantaneous and Mean Velocity Flow Characteristics and Spectral Analysis	----- 33
	4.1 Instantaneous Velocities	----- 33
	4.2 Velocity Moments Across the Mixing Layer	----- 33
	4.3 Spectral Analysis Technique	----- 35
	Spectral and Cross-Spectral Results	----- 49

5	Results and Discussion - - - - -	69
5.1	Phase 1- - - - -	69
	The Numerical Approximation- - - - -	69
	Results of the Orthogonal Decomposition Analysis for Phase 1 - - - - -	71
5.2	Phase 2- - - - -	75
5.3	Azimuthal Problem Streamwise Velocity Only - Phase 3 - - - - -	79
	5.3.1 Results of the Azimuthal Decomposition Analysis - Phase 3- - - - -	79
	5.3.2 Results of the Orthogonal Decomposition Phase 3 - - - - -	87
5.4	Azimuthal Problem Streamwise and Radial Velocity - Phase 4 - - - - -	94
	5.4.1 Results of the Azimuthal Decomposition Analysis - Phase 4- - - - -	95
	The High Speed Side of the Mixing Layer - - - - -	96
	The Center Region of the Mixing Layer - - - - -	96
	5.4.2 Results of the Orthogonal Decomposition Phase 4 - - - - -	98
	5.4.3 Phase 3 and 4 - Discussion- - - - -	116
	5.4.4 A Proposed Mechanism- - - - -	116
6	Conclusion - - - - -	120
7	Recommendations for Further Study- - - - -	122
	References - - - - -	126

ACKNOWLEDGEMENTS

I would like to thank my mentor, Professor William K. George for his guidance and friendship throughout my graduate school tenure. I express thanks to Professor Parvis Moin, my advisor at NASA/Ames, for his continued interest and support for this work. I thank my wife, Gina and my colleagues in the TRL for many enlightening discussions (not all technical) and for their support and encouragement while I was working on this dissertation. Finally, a special note of thanks goes to Eileen Graber for typing the manuscript and being so helpful through the years.

This research was initiated under support from the National Science Foundation under Grant No. ENG7617466 and the Air Force Office of Scientific Research under Contract Nos. F4962078C0047 and F4962080C0053. Work was continued under NSF Grant No. 8316833 and with the support of the NASA trainee program at NASA/Ames.

the potential core but with the fourth, fifth and sixth modes dominating from the center of the mixing layer and outward toward the low-speed side of the mixing layer. The Reynolds-stress azimuthal correlations and their breakdown into azimuthal modes show that the incoherent turbulence is transported to the center of the coherent structure as suggested by Hussain (1986). The results are shown to be consistent with the vortex ring-type instability investigated by Widnall and Sullivan (1973).

A life-like cycle is proposed for the evolution of coherent structures in the jet mixing layer which begins with inception of rings of concentrated vorticity from an instability of the mean flow, then a vortex-ring type instability arising from the interaction of two different rings, and finally a cascade of energy to small scales by vortex breakup and stretching. A view of the orthogonal decomposition (Lumley 1967, 1970) is proposed in which the large eddy is not necessarily identified with the lowest order eigenfunctions, but rather the eigenfunctions define in an optimal manner the evolution in time and space of large scale vorticity concentrations.

LIST OF FIGURES

<u>Figure No.</u>	<u>Figure Title</u>	<u>Page No.</u>
2.1.1		4
3.1.1	Jet Facility Schematic	12
3.1.2	Spectrum of Streamwise Velocity at Exit of Jet	13
3.1.3	Traversing System	16
3.2.1(a)	Single Wire arrangement for 13 wire probe	17
3.2.1(b)	Cross-wire arrangement	17
3.3.1	Flow chart showing method used to obtain streamwise velocities	21
3.4.1	Cross-wire geometry	23
3.4.2	Rig for performing angle calibration of a rake of cross-wires	26
3.4.3	Flow chart showing method used to obtain u and v velocities on disk	27
3.5.1	Probe roll-off example	29
3.5.2	Linear plot of streamwise velocity spectrum near center of mixing layer at $x/D=3$	30
4.1.1	Instantaneous streamwise velocities for 7 radial locations at $x/D=3$	34
4.2.1	Mean streamwise velocity at $x/D=3$ vs. radius in the jet mixing layer	36
4.2.2	RMS streamwise velocity at $x/D=3$ vs. radius in the jet mixing layer	37
4.2.3	RMS radial velocity at $x/D=3$ vs. radius in jet mixing layer	38
4.2.4	\overline{uv} at $x/D=3$ vs. radius in the jet mixing layer.	39
4.2.5	Mean values of Glauser on those of Hussain and Clark	40

4.2.6	Streamwise RMS velocities of Glauser super-imposed on those of Hussain and Clark	41
4.2.7	Radial RMS velocities of Glauser super-imposed on those of Hussain and Clark	42
4.3.1	Unfiltered velocity spectrum near center of mixing layer at $x/D=3$ showing extended $k^{-5/3}$ range	43
4.3.2(a)	Boxcar function for the FFT	46
4.3.2(b)	Sample time history of length T	46
4.3.3	Effective filter shape with no tapering	46
4.3.4(a)	Streamwise velocity spectrum at $r/D=0.13$, $x/D=3$	51
4.3.4(b)	Streamwise velocity spectrum at $r/D=0.29$, $x/D=3$	52
4.3.4(c)	Streamwise velocity spectrum at $r/D=0.35$, $x/D=3$	53
4.3.4(d)	Streamwise velocity spectrum at $r/D=0.46$, $x/D=3$	54
4.3.4(e)	Streamwise velocity spectrum at $r/D=0.57$, $x/D=3$	55
4.3.4(f)	Streamwise velocity spectrum at $r/D=0.68$, $x/D=3$	56
4.3.4(g)	Streamwise velocity spectrum at $r/D=0.79$, $x/D=3$	57
4.3.4(h)	Streamwise velocity spectrum at $r/D=0.90$, $x/D=3$	58
4.3.5(a)	Radial velocity spectrum at $r/D=0.13$, $x/D=3$	59
4.3.5(b)	Radial velocity spectrum at $r/D=0.29$, $x/D=3$	60
4.3.5(c)	Radial velocity spectrum at $r/D=0.35$, $x/D=3$	61
4.3.5(d)	Radial velocity spectrum at $r/D=0.46$, $x/D=3$	62

4.3.5(e)	Radial velocity spectrum at $r/D=0.57, x/D=3$	63
4.3.5(f)	Radial velocity spectrum at $r/D=0.68, x/D=3$	64
4.3.5(g)	Radial velocity spectrum at $r/D=0.79, x/D=3$	65
4.3.5(h)	Radial velocity spectrum at $r/D=0.90, x/D=3$	66
4.3.6(a)	Co-spectrum between 2 radial locations ($r/D=0.68, r/D=0.79$) at $x/D=3$	67
4.3.6(b)	Quad-spectrum between 2 radial locations ($r/d=0.68, r/D=0.79$) at $x/D=3$	68
5.1.1	Eigenspectra showing how energy is distributed among the first three eigenvalues	72
5.1.2	Individual contributions to the power spectrum from first 2 modes.	72
5.1.3	Convergence of power spectrum	73
5.1.4	Real part of F.T. of original signal	73
5.1.5	First mode superimposed on original	74
5.1.6	First 2 modes superimposed on original	74
5.1.7	First 3 modes superposed on original	74
5.2.1(a)	$\overline{u^2}$ as a function of radius in the jet mixing layer for the 7 wire case with the contribution from the first eigen- function superimposed on it	77
5.2.1(b)	$\overline{u^2}$ as a function of radius in the jet mixing layer for the 13 wire case with the contribution from the first eigen- function superimposed on it	78
5.3.1(a)	$R_{11}(\theta)$ at $x/D=3, r/D=0.13$	83
5.3.1(b)	$B_{11}(m)$ at $x/D=3, r/D=0.13$	83
5.3.2(a)	$R_{11}(\theta)$ at $x/D=3, r/D=0.26$	84
5.3.2(b)	$B_{11}(m)$ at $x/D=3, r/D=0.26$	84
5.3.3(a)	$R_{11}(\theta)$ at $x/D=3, r/D=0.39$	85

5.3.3(b)	$B_{11}(m)$ at $x/D=3$, $r/D=0.39$	85
5.3.4(a)	$R_{11}(\theta)$ at $x/D=3$, $r/D=0.52$	86
5.3.4(b)	$B_{11}(m)$ at $x/D=3$, $r/D=0.52$	86
5.3.5	First 3 eigenspectra for mode 0	88
5.3.6	First 3 eigenspectra for mode 1	88
5.3.7	First 3 eigenspectra from phase 1 (radius and time only)	90
5.3.8	(-.-.) B_{11} for mode 0, (....) contribution from 1 term	93
5.3.9	(-.-.) $\overline{u^2}$, (....) contribution from first term to u^2	93
5.4.1(a)	$R_{11}(\theta)$ at $r/D=0.13$, $x/D=3$	99
5.4.1(b)	$B_{11}(m)$ at $r/D=0.13$, $x/D=3$	99
5.4.2(a)	$R_{22}(\theta)$ at $r/D=0.13$, $x/D=3$	100
5.4.2(b)	$B_{22}(m)$ at $r/D=0.13$, $x/D=3$	100
5.4.3(a)	$R_{12}(\theta)$ at $r/D=0.13$, $x/D=3$	101
5.4.3(b)	$B_{12}(m)$ at $r/D=0.13$, $x/D=3$	101
5.4.4(a)	$R_{11}(\theta)$ at $r/D=0.35$, $x/D=3$	102
5.4.4(b)	$B_{11}(m)$ at $r/D=0.35$, $x/D=3$	102
5.4.5(a)	$R_{22}(\theta)$ at $r/D=0.35$, $x/D=3$	103
5.4.5(b)	$B_{22}(m)$ at $r/D=0.35$, $x/D=3$	103
5.4.6(a)	$R_{12}(\theta)$ at $r/D=0.35$, $x/D=3$	104
5.4.6(b)	$B_{12}(m)$ at $r/D=0.35$, $x/D=3$	104
5.4.7(a)	$R_{11}(\theta)$ at $r/D=0.46$, $x/D=3$	105
5.4.7(b)	$B_{11}(m)$ at $r/D=0.46$, $x/D=3$	105
5.4.8(a)	$R_{12}(\theta)$ at $r/D=0.57$, $x/D=3$	106
5.4.8(b)	$B_{12}(m)$ at $r/D=0.57$, $x/D=3$	106
5.4.9	First 3 eigenspectra, mode 0	107

5.4.10	First 3 eigenspectra, mode 1	108
5.4.11	First 3 eigenspectra, mode 2	109
5.4.12	First 3 eigenspectra, mode 3	110
5.4.13	First 3 eigenspectra, mode 4	111
5.4.14	First 3 eigenspectra, mode 5	112
5.4.15	First 3 eigenspectra, mode 6	113
5.4.16	First 3 eigenspectra, mode 7	114
5.4.17	First 3 eigenspectra, mode 8	115
5.4.18	The proposed 4 stages of turbulence production	117
7.1	Characteristic eddy calculated from shot-noise decomposition	124

NOMENCLATURE

a	Random coefficients in transform domain
A_{ij}	Azimuthal complex coefficients
A_n	Hot wire calibration coefficients
B_{ij}	A_{ij} summed over frequency
C_{ij}	Cross-correlation tensor
D_0-D_7	Logic '0' or '1' (frequency select)
D	Exit diameter of jet
E	Mean voltage from hot wire bridge
f	frequency in Hz
f_c	Corner frequency
f_s	A/D sampling frequency
i	Square root of -1
k_1	axial coefficients wire 1
k_2	axial coefficients wire 2
L	Total span of finite energy
\mathcal{L}	Integral scale
l_w	Sensing length of hot wire
m	Azimuthal mode number
R	Radius 1 of project
R_{ij}	2-point velocity tensor
r	Radius in jet mixing layer
S	Power spectrum
T	Finite time record length
t	Time
U	Mean streamwise velocity

U_{eff_1}	Effective velocity seen by wire 1 of the cross wire
U_{eff_2}	Effective velocity seen by wire 2 of the cross wire
U_0	Velocity vector seen by x-wire
u	Instantaneous velocity vector
\hat{u}_i	Fourier transform of instantaneous velocity
u'	RMS streamwise velocity
\overline{uv}	Reynolds stress
v'	RMS radial velocity
W	Weighting function
W_T	Spectral window
Σ	Inhomogeneous directions
a	Random coefficients
β	Angle between U_0 and probe axis
δ	Kroneker delta function
$\delta\beta$	Angle between probe axis and flow axis
η	Kolmogorov length scale
θ	Azimuthal angle in jet
θ_m	Momentum thickness
$\lambda(n)$	Eigenvalues
τ	Time difference in stationery field
\hat{Q}	Eigenvector
ϕ_1	Angle between U_0 and normal to wire 1
ϕ_2	Angle between U_0 and normal to wire 2
Φ_{ij}	Cross spectral tensor
\hat{U}	Eigenvectors in transform domain

CHAPTER 1

1.1 Introduction

Qualitative models for the large scale structures in a number of turbulent flows were formulated by Grant (1958) and Townsend (1956). These structures were assumed to be responsible for finite correlation at large lags (i.e. bigger than the integral scale) and to account for 10-20% of the total energy. They were believed to be responsible for intermittency and entrainment but were not believed to be very involved (at least directly) in the energetics of the flow. Large eddies were viewed as rather passive contributors to the dynamics of the turbulence.

In the early 1970's the turbulence community discovered coherent structures (v. Crowe and Champagne 1971, Brown and Roshko 1974). Unlike Townsend's passive eddies these coherent structures were very active phenomena. They were visible clearly with flow visualization where they were seen to pair and explode (v. Hussain and Clark 1981). Like Townsend's (1956) big eddies these coherent structures were responsible for entrainment and mixing. It was alleged that turbulence could not be modelled, much less understood, without explicitly accounting for the existence of coherent structures (v. Liepmann (1979)). Averaging, at least of the conventional form, was considered outdated since it smeared out such events. It was suggested that conditional averaging was the thing to do (v. Cantwell 1981). This approach has been extensively exploited over the past decade (v. Hussain 1986).

Where has this approach taken us? We have seen many coherent structures but we still do not have a very good idea as to why they arise nor do we understand their dynamics. In addition, a practical

modelling scheme which incorporates them has yet to be developed.

What is a coherent structure? To this point the turbulence community has been unable to provide a definition which can be exploited in a dynamical model of the turbulence. The situation has been nicely summed up by Lumley (1982) who draws an analogy to the definition of pornography, i.e., "it is hard to define but you know it when you see it!" Such has indeed been the case with coherent structures in turbulence.

In 1967 Lumley proposed that a coherent structure should be that structure which has the largest mean square projection on the velocity field. This structure is identified by correlating the proposed structure in the mean square sense with an ensemble of realizations of the flow field. This maximization leads to a well-defined integral eigenvalue problem which has as its kernel the velocity cross-correlation tensor. Because this velocity tensor is symmetric the solutions to the integral eigenvalue problem are governed by the Hilbert-Schmidt theory (v. Lumley (1967)). These solutions allow a representation of any one of the original realizations in terms of the orthogonal eigenfunctions extracted from the eigenvalue problem. It also allows for objective determination of the contributions of the individual orthogonal eigenmodes to the kinetic energies and Reynolds stresses. A small number of researchers have applied this decomposition to various flows: Payne (1966), Bakewell (1967), Lemmerman (1976), Moin (1984) and Herzog (1986).

In this current work the decomposition is applied to the near field mixing layer of the axisymmetric jet. The earliest investigations of the statistical characteristics of jet shear layer

were carried out by Lawrence (1956), Davies et al. (1963) and Bradshaw et al. (1964). Crowe and Champagne (1971) found identifiable structures in a jet which resembled large scale vortical puffs. These experiments, however, contained much less information about the two-point correlation tensor than is needed to solve the integral eigenvalue problem. Hence the goal of this work has been to acquire the necessary data to apply the General Orthogonal Decomposition to the near field jet mixing layer.

The measurements were performed in the axisymmetric jet facility of the Turbulence Research Laboratory at the University at Buffalo, SUNY. This facility is described in detail in Chapter 3. The initial data reduction was performed using the Vax Cluster System of the University at Buffalo. The eigenvalue problem was solved at NASA/Ames using the Cray XMP.

CHAPTER 2

THEORY - ORTHOGONAL DECOMPOSITION

2.1 The General Inhomogeneous Problem

In 1967 Lumley proposed that the coherent structure should be that structure which has the largest mean square projection on the velocity field. If $\phi(\underline{x}, t)$ is our candidate structure, then ϕ should be chosen to maximize

$$\overline{|\underline{u} \cdot \phi|^2} = |\alpha|^2 \quad (2.1.1)$$

where $\underline{u} = u(\underline{x}, t)$ is the instantaneous velocity and the overbar denotes the ensemble average. The above expression is assumed to be normalized by the modulus of ϕ so that (2.1.1) depends only on the degree of projection and not the magnitude. ϕ is then, in the averaged mean square sense, the most likely occurrence of \underline{u} . To get a physical sense of what has been suggested examine Figure 2.1.1

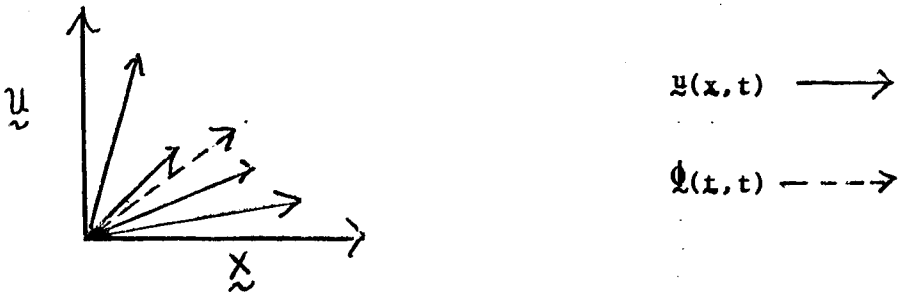


Figure 2.1.1

In this figure the solid line vectors correspond to different realizations of \underline{u} , the random velocity, and the dashed line vector corresponds to ϕ , the candidate structure.

Maximizing $\overline{|\alpha|^2}$ can be done by using the methods of variational calculus. This leads to the following integral eigenvalue problem (Lumley 1970):

$$\iint R_{ij}(\mathbf{x}, \mathbf{x}', t, t') \phi_j(\mathbf{x}', t') d\mathbf{x}' dt' = \lambda \phi_i(\mathbf{x}, t) \quad (2.1.2)$$

where

$$R_{ij}(\mathbf{x}, \mathbf{x}', t, t') = \overline{u_i(\mathbf{x}, t) u_j(\mathbf{x}', t')} \quad (2.1.3)$$

is the two-point correlation tensor, and

$$\lambda = \overline{|a|^2} \quad (2.1.4)$$

Because R_{ij} is a symmetric function the solution of (2.1.2) can be discussed using the Hilbert-Schmidt theory (Lumley 1967). Also, if the random vector field is of finite extent so that the integral in (2.1.2) is over a finite area then the following hold (Lumley 1967):

1. There are not one, but a discrete set of solutions so that (2.1.2) becomes

$$\begin{aligned} \iint R_{ij}(\mathbf{x}, \mathbf{x}', t, t') \phi_j^{(n)}(\mathbf{x}', t') d\mathbf{x}' dt' \\ = \lambda^n \phi_i^{(n)}(\mathbf{x}, t), \quad (n=1, 2, 3, \dots) \end{aligned} \quad (2.1.5)$$

2. This discrete set can be chosen so that the $\phi_i^{(n)}$ are orthogonal, i.e.,

$$\int \phi_i^{(p)}(\mathbf{x}, t) \phi_i^{(q)}(\mathbf{x}, t) d\mathbf{x} dt = \delta_{pq} \quad (2.1.6)$$

3. The original random vector field u_i may be expressed in terms of the $\phi_i^{(n)}$ as

$$u_i(\mathbf{x}, t) = \sum \alpha_n \phi_i^{(n)}(\mathbf{x}, t) \quad (2.1.7)$$

where

$$\alpha_n = \int u_i(\mathbf{x}, t) \phi_i^{(n)*}(\mathbf{x}, t) d\mathbf{x} dt \quad (2.1.8)$$

The series converges in mean square and the coefficients in (2.1.8) are uncorrelated, i.e.,

$$\overline{\alpha_n \alpha_m} = \begin{cases} 0 & n \neq m \\ \lambda^{(n)} & n = m \end{cases} \quad (2.1.9)$$

4. The kernel R_{ij} can be decomposed into a double series in the $\phi_i^{(n)}$ and the series is uniformly and absolutely convergent, i.e.,

$$R_{ij}(\underline{x}, \underline{x}', t, t') = \sum_{i=1}^{\infty} \sum_{j=1}^{\infty} \lambda^{(n)} \phi_i^{(n)}(\underline{x}, t) \phi_j^{(n)*}(\underline{x}', t') \quad (2.1.10)$$

5. The $\lambda^{(n)}$ are positive and their sum is finite

$$\lambda^{(n)} > 0, \quad \sum \lambda^{(n)} < \infty \quad (2.1.11)$$

and

$$\lambda^{(1)} > \lambda^{(2)} > \lambda^{(3)} > \dots > \lambda^{(n)} \quad (2.1.12)$$

The Orthogonal Decomposition is a non-prejudicial way of extracting organized structures from an inhomogeneous random function on an energy-weighted basis. The structures obtained are those that contribute the most to the energy because the representation converges optimally fast - the first term (or largest structure according to Lumley) is as large as possible (in a mean-square sense), the next term as large as possible, and so on.

2.2 Dealing With Stationary, Homogeneous or Periodic Directions

The Orthogonal Decomposition Theorem reduces to the Harmonic Decomposition Theorem if the process is stationary, homogeneous or periodic. If the process is stationary, homogeneous, or periodic in one or more variables, then the eigenfunction are harmonic functions in these directions. Since the eigenfunctions are known for these

variables, it is convenient usually to carry out a Fourier analysis in these directions first.

In the axisymmetric jet being studied the time 'direction' is stationary and the azimuthal direction is periodic as well as symmetric (v. Sreenivasan (1984)) so that $R_{ij}(\mathbf{x}, \mathbf{x}', t, t')$ in equation (2.1.3) breaks down in the following manner. First the time direction is removed by using the Fourier transform

$$\Phi_{ij}(\mathbf{x}, \mathbf{x}', \theta, f) = \int_{-\infty}^{\infty} e^{-i2\pi f\tau} R_{ij}(\mathbf{x}, \mathbf{x}', \tau, \theta) d\tau \quad (2.2.1)$$

resulting in

$$R_{ij}(\mathbf{x}, \mathbf{x}', \tau, \theta) \longrightarrow \Phi_{ij}(\mathbf{x}, \mathbf{x}', \theta, f)$$

where Φ_{ij} is the cross-spectral tensor. Second, a decomposition (of the cross-spectral tensor now) over the periodic and symmetric direction gives

$$\Phi_{ij}(\mathbf{x}, \mathbf{x}', \theta, f) = \sum_{m=0}^{\infty} A_{ij}(\mathbf{x}, \mathbf{x}', f, m) \cos m\theta \quad (2.2.2)$$

where m is the azimuthal mode number, θ is the difference in azimuthal angle, and \mathbf{x} denotes the remaining inhomogeneous variables. The complex coefficients of the above series are defined by

$$A_{ij}(\mathbf{x}, \mathbf{x}', f, 0) = \frac{1}{\pi} \int_0^{\pi} \Phi_{ij}(\mathbf{x}, \mathbf{x}', \theta, f) d\theta \quad (2.2.3)$$

and by

$$A_{ij}(\mathbf{x}, \mathbf{x}', f, m) = 2/\pi \int_0^{\pi} \Phi_{ij}(\mathbf{x}, \mathbf{x}', \theta, f) \cos m\theta d\theta, m > 0 \quad (2.2.4)$$

Finally, the inhomogeneous direction is decomposed by using

A_{ij} in equation (2.1.5), thus

$$\int A_{ij}(\mathbf{x}, \mathbf{x}', f, m) \Psi_j^{(n)}(\mathbf{x}', f, m) d\mathbf{x}'$$

$$= \lambda^{(n)}(f, m) \Psi_i^{(n)}(\mathbf{x}, f, m). \quad (2.2.5)$$

The eigenvalues have now become frequency and azimuthal mode dependent eigenspectra, i.e.,

$$\lambda^{(n)} \longrightarrow \lambda^{(n)}(f, m) \quad (2.2.6)$$

and the eigenvectors are frequency and mode number dependent, i.e.,

$$\phi_i^{(n)}(\mathbf{x}, t) \longrightarrow \Psi_i^{(n)}(\mathbf{x}, f, m). \quad (2.2.7)$$

2.3 The Experimental Approach

The choice of the near field mixing layer of the turbulent axisymmetric jet for this study was made for several reasons. In particular, since the purpose of this work was to utilize and evaluate the Orthogonal Decomposition theorem, the flow to be studied had to be relatively easy to set up, the measuring techniques standard, and capable of working well in the environment. The axisymmetric jet mixing layer is a relatively simple flow to generate (based on previous experience) and stationary hot wires are known to work reasonably well in this environment.

Obtaining sufficient information on the two-point cross-spectral tensor to apply the Orthogonal Decomposition in the jet (or any flow for that matter) is an ambitious and difficult task. Because of this an approach was devised that consisted of doing the experiment in several phases. This allowed for a gain of experience from each phase. The effects of grid density, sampling rate, spectral

convergence, time record length and other relevant questions could be ascertained from the first few phases before the final experiment was performed.

The first phase (v. Glauser et al. 1987) involved using a rake of seven hot-wire probes radially spanning the jet mixing layer at $x/D=3$. This arrangement gave instantaneous streamwise velocity data as a function of radius in the jet mixing layer. From this data $\Phi_{11}(r,r',f)$ was computed and the integral eigenvalue problem solved using it (see Equation 2.2.1). In this case r (the radius in the mixing layer) is the inhomogeneous variable.

The second phase involved using a rake of 13 hot-wire probes across the same span as in phase 1. Again this arrangement gave instantaneous streamwise velocity data as a function of radius in the jet mixing layer, only now at 13 positions. The second phase was performed because of a grid density question that arose from the first experiment. This will be discussed in greater detail in Chapter 5.

The third phase (v. Glauser and George (1987)) involved adding the azimuthal variation to the problem in phase 1. The azimuthal correlations were realized in the following manner: one rake of seven hot-wire probes (same as in phase 1) was fixed at an arbitrarily chosen azimuthal position (since the flow was axisymmetric) while another rake of 7 hot-wire probes was moved azimuthally. In all, 16 azimuthal positions were measured over a span of 180 degrees. The addition of the azimuthal variation to the streamwise correlations gave $\Phi_{11}(r,r',\theta,f)$ where θ is the difference in azimuthal angle.

The fourth phase (v. Glauser and George (1987)) involved measuring, in addition to the streamwise velocity, the radial velocity

component. In effect, phases 1 and 3 were essentially repeated, only now including the radial velocity. This final phase involved using two rakes of probes with 4 cross-wires on each rake. In all, 25 azimuthal positions were measured over a span of 180 degrees. The results of phase 3 suggest that the grid used (16 azimuthal positions) was too coarse so that 25 azimuthal positions were used in phase 4 (see Section 5.3). From this data $\phi_{11}(r, r', f, \theta)$, $\phi_{12}(r, r', f, \theta)$, $\phi_{22}(r, r', f, \theta)$ and $\phi_{21}(r, r', f, \theta)$ were calculated, the integral eigenvalue problem was solved and the results compared to those in the previous phases.

CHAPTER 3

THE EXPERIMENT

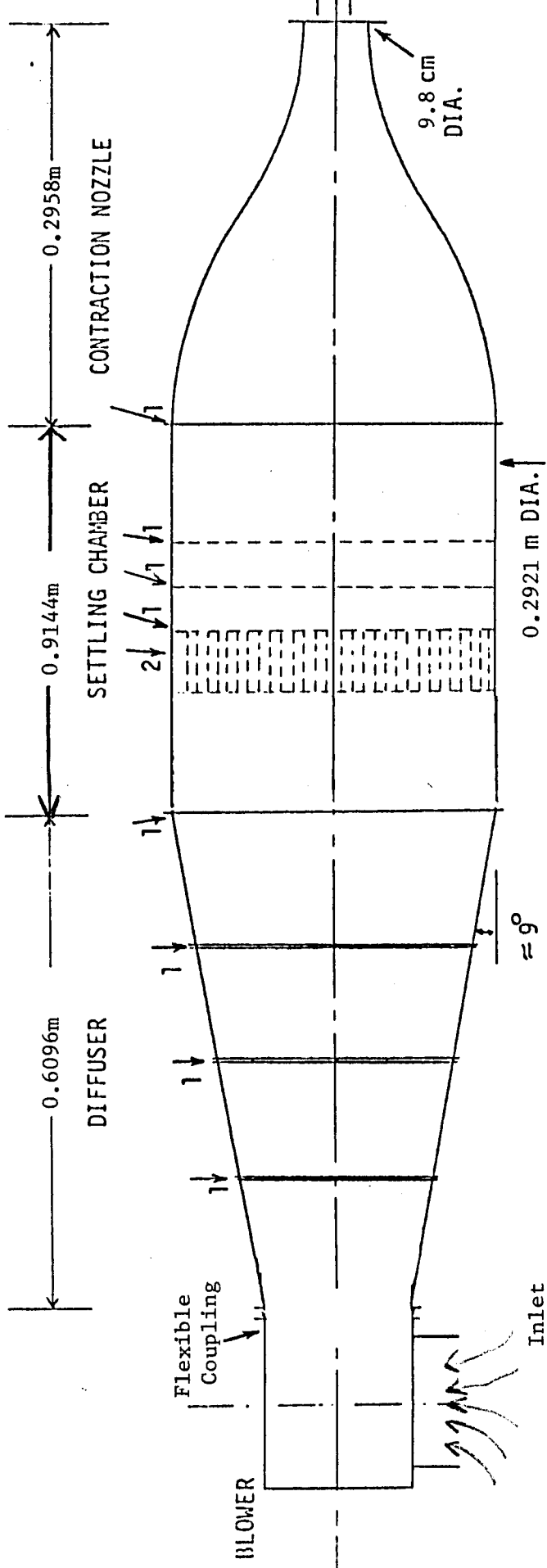
3.1 The Facility

The facility for producing an isothermal, incompressible, axisymmetric air jet is shown schematically in Figure 3.1.1. This facility can be used to create exit velocities of from 0.5 m/s to 40 m/s.

The exit conditions of the jet in this experiment were as follows: the turbulence intensity was 0.35%, the Reynolds number based on exit diameter was 110,000, the boundary layer at the exit was turbulent with an approximate thickness of 0.0012 m (based on $U=0.99U_e$) and the mean velocity profile was flat to within 0.1%. A spectrum of the fluctuating velocity at the exit plane is shown plotted in Figure 3.1.2.

The blower is a Dayton Model No. 4C108 with a 10-5/8" wheel containing six blades. It is directly driven by a 1 HP, 3 phase AC motor which, in turn is controllable by a Toshiba Esp-130 transistor inverter motor controller. The blower is rigidly mounted to a heavy table in order to minimize vibrations.

The diffuser is connected to the blower with flexible mounts to isolate the blower from the rest of the facility. The diffuser is 0.6096m long with the final diameter being 0.2521m. This combination results in a total diffuser angle of approximately 19 degrees. The diffuser consists of 3 equal length sections, the first of which allows for a conversion of rectangular (the exit of the blower is rectangular) to circular. In between each of the first two sections



- 1. SCREEN.
- 2. HONEYCOMB.

FIG. 3.1.1 JET FACILITY SCHEMATIC.

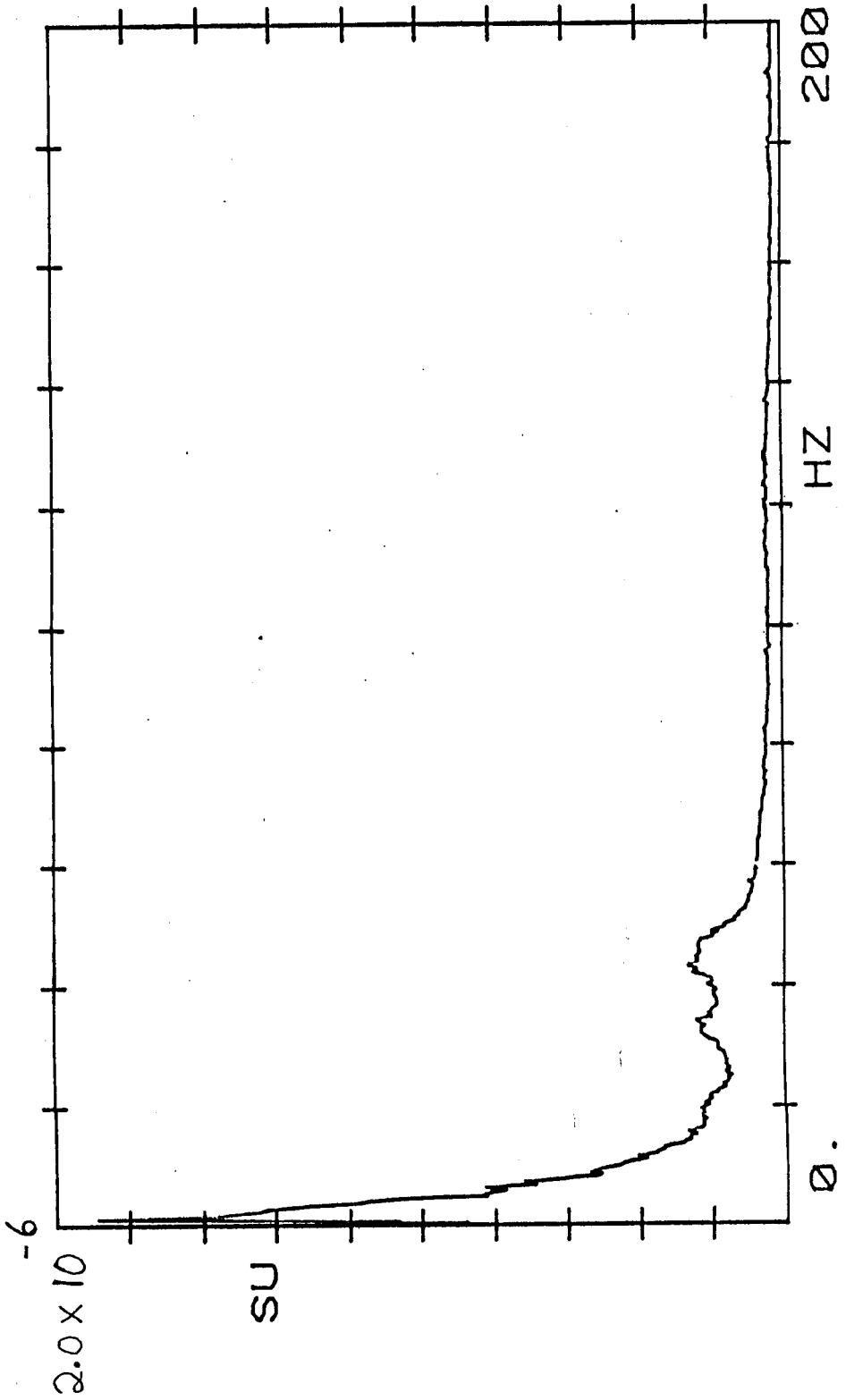


Figure 3.1.2 Spectrum of streamwise velocity at exit of jet.

is a 20 mesh, 25% solidity screen. At the point where the diffuser joins the settling chamber there is a 30 mesh, 35% solidity screen. This arrangement was chosen to avoid flow separation over the flow ranges obtainable from this facility. The basis for this design was taken from NACA Report No. 949.

Downstream of the diffuser is a 0.9144m long, 0.2921m in diameter settling chamber. At 0.254m downstream from the entrance of the settling chamber a 5cm long honeycomb section begins. This honeycomb section is fabricated from approximately 4000, 4.5 mm in diameter soda pop straws packed neatly together and aligned with the flow axis. A 20 mesh, 25% solidity screen is used to keep the straws from being carried downstream by flow induced drag forces and at a distance 0.3m downstream of the honeycomb section a final 30 mesh, 35% solidity screen is located.

A jet nozzle is connected to the end of the settling chamber. This nozzle is of fifth order polynomial design, has an exit diameter of 0.098m, and an area contraction ratio of 10:1. The nozzle was fabricated from fiberglass cloth and marine polyester resin. The fabrication procedure was as follows: a polyurethane mold was machined to a predetermined matched fifth order polynomial. The fiberglass cloth, soaked in the polyester resin mix, was then draped over the mold and allowed to harden. After the mold was removed the imperfections on the inside surface were filled using auto body finishing putty. Since irregularities on the inner surface could trip the boundary layer and increase the turbulence levels at the exit, great care was taken to keep the undulations on the inner surface small (less than 0.1 mm typically).

The traversing system used is shown in Fig. 3.1.3. The hot-wire rakes were held in place by the two plexiglass rigs as shown. One rig was free to move azimuthally to realize the correlations in that direction.

The entire axisymmetric jet facility is centered in a large 5m x 5m x 20m mylar covered enclosure. The enclosure is located in a larger 7m x 10m x 30m laboratory which houses the computers and other hardware utilized in the experiment.

3.2 Instrumentation

The transducers used for sensing velocities were hot-wire probes. These probes were grouped together on a rake that consisted of four 13 single-wire probes or 4 cross-wires (see Figure 3.2.1). Each individual sensor was 5 microns in diameter and had a sensing length of 1.2 mm giving a length-to-diameter ratio of 220. The wires, 3 mm in length, were made of tungsten with copper plating utilized on the inactive length that was soldered to the prongs. These specially designed probes were fabricated in the following manner: A double-sided printed circuit board was cut to a form to minimize aerodynamic interference. The copper printed circuit boards were then etched to form the appropriate circuit. This consisted of a place to connect a card-edge connector and a position to allow the prongs to be soldered to the printed circuit board. The prongs were jewelers broaches manufactured by Vigor-Bergeon. Once these prongs were soldered to the P.C. board they could be bent to achieve the appropriate dimensions between the prongs. 30 lb. dacron fishing line, glued to the prongs, was used to stiffen the prongs so that the sensing elements themselves would be less susceptible to vibration and sagging.

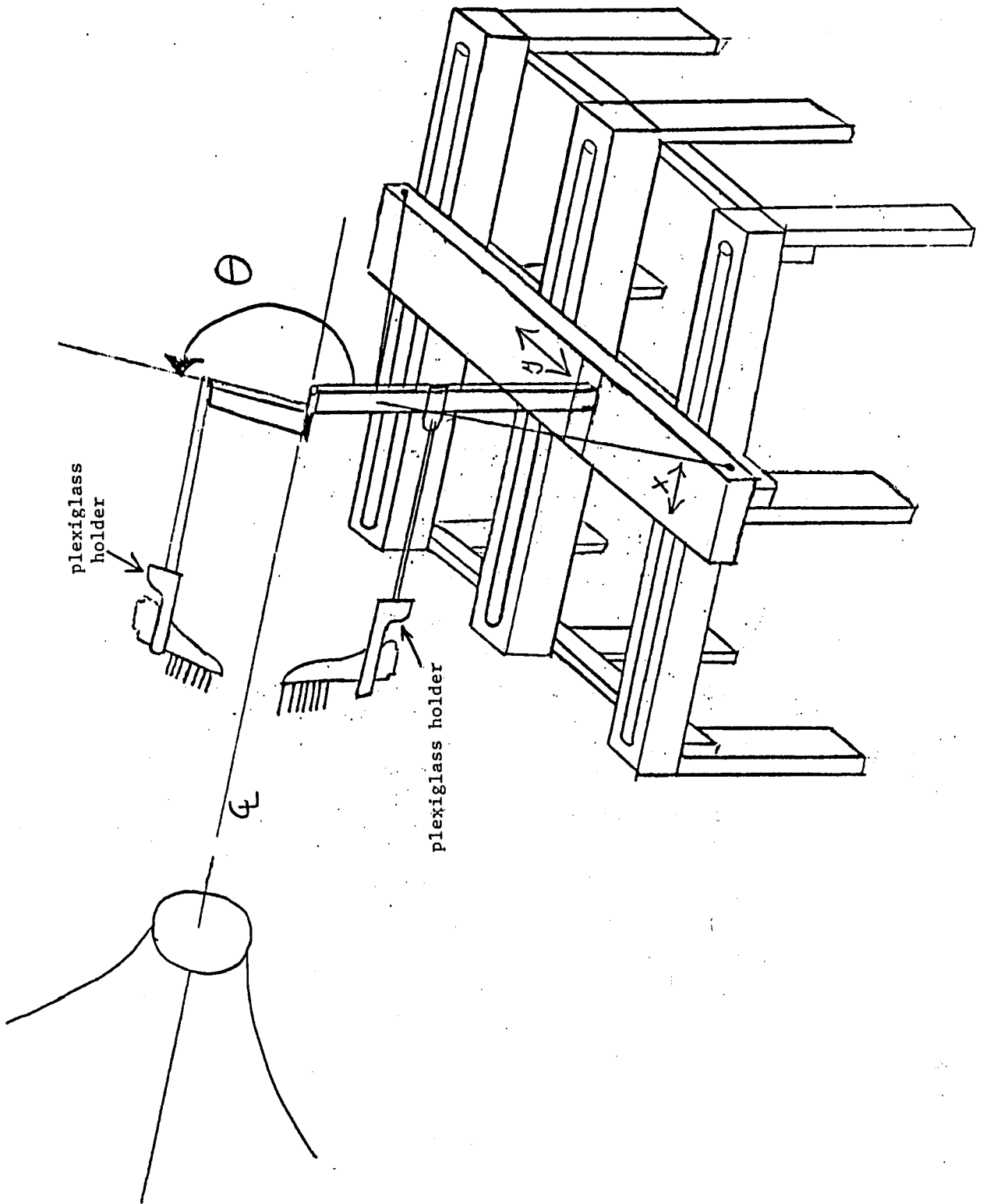


Figure 3.1.3 Traversing system.

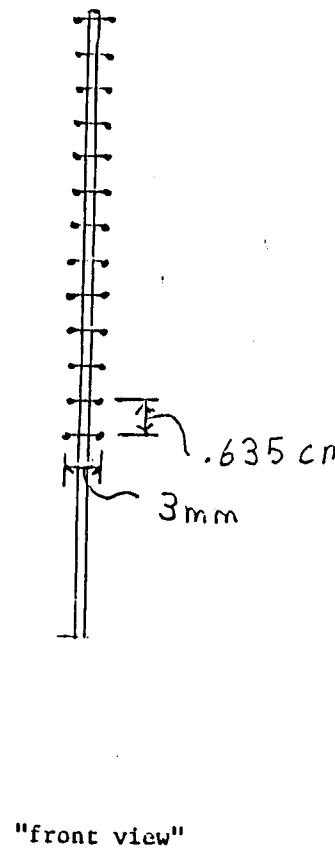
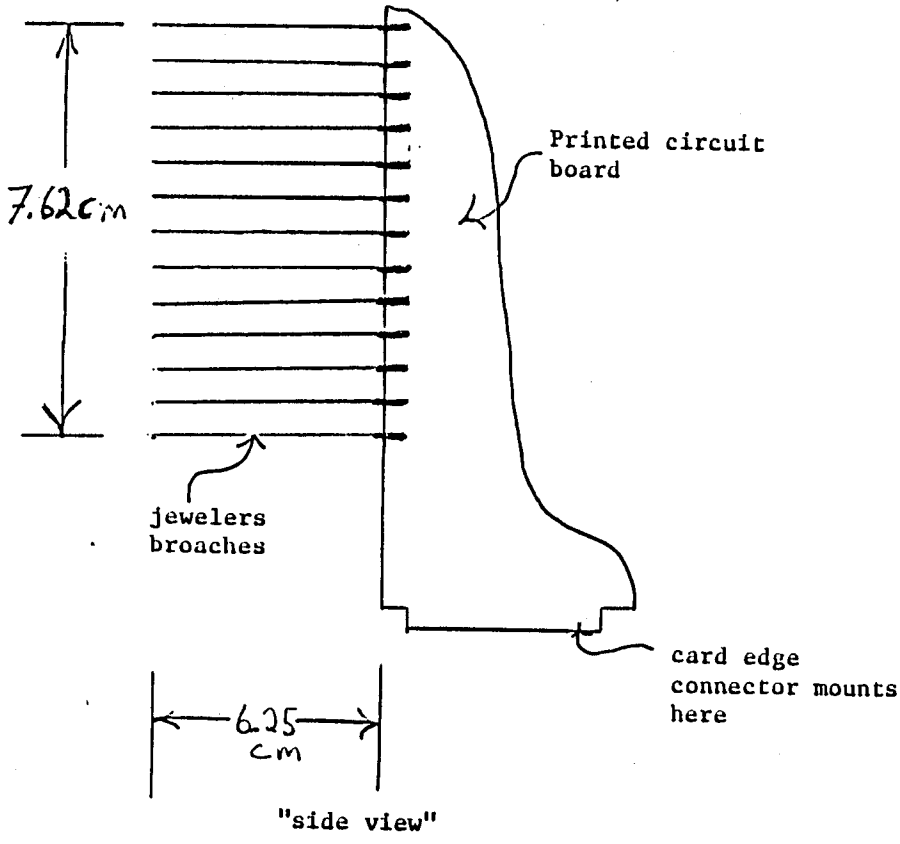


Figure 3.2.1(a) Single wire arrangement for 13 wire probe.

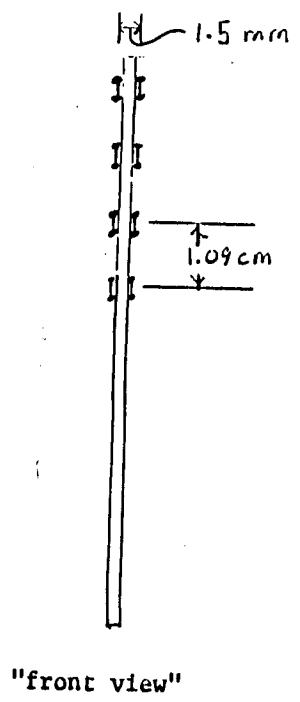
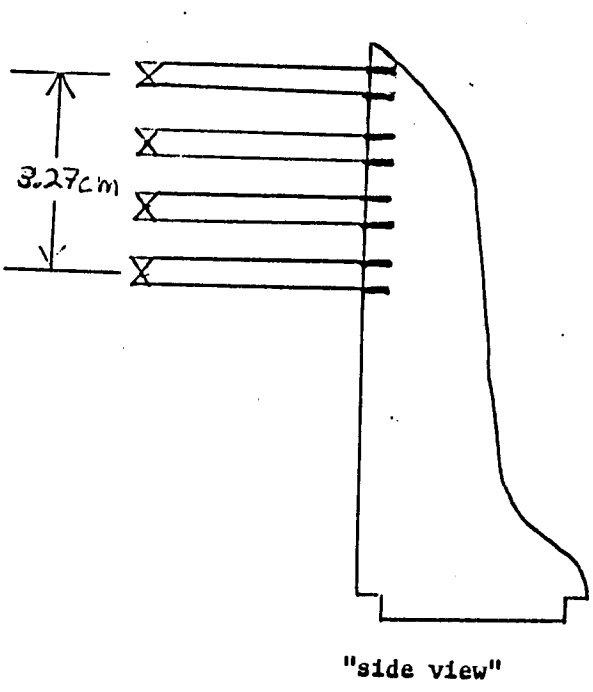


Figure 3.2.1(b) Cross-wire arrangement.

Each probe formed one arm of either a Dantec (DISA) 55M10 or 56C16 CTA standard bridge used in conjunction with a Dantec 55M01 or 56C01 Main Unit respectively. The individual bridges were each set to give a wire overheat ratio of 0.8. Either 5m or 20m long cables were incorporated in the probe arm of the particular bridge. The response of each system (including probes, prongs, printed circuit boards, card edge connector and cables) to a square wave test was tuned so that there was less than 10% overshoot. This allowed for stable operation over the bandwidth of interest (DC-6kHz).

The bridge top voltage of each anemometer was connected to a 8-pole Bessel low pass anti-aliasing filter manufactured by Frequency Devices. These 848P8L-5 Bessel low-pass active filters are tunable over a 200 Hz to 51.2KHz frequency range. These units have been digitally configured to transfer frequency control input data.

The digital tuning interface circuits are two 4042 quad CMOS latches which accept the following CMOS compatible inputs: eight tuning bits (D_0 - D_7), a latch Strobe bit (C), and a transition polarity bit (P). The system has been set up to operate with (P) tied low so that the frequencies are latched on the rising edge of the strobe. The filter tuning follows the tuning equation given below:

$$f_c = 200[1 + D_7x2^7 + D_6x2^6 + D_5x2^5 + D_4x2^4 + D_3x2^3 + D_2x2^2 + D_1x2^1 + D_0x2^0]$$

where D_0 - D_7 = logic "0" or "1" and f_c = corner frequency. The minimum tunable frequency is 200 Hz and the minimum frequency step is 200 Hz. A control module board was designed and built to program the above filters.

The purpose of the control module board is to allow the user to select the corner frequency and particular channel. It is configured to operate as follows: The user selects the corner frequency and particular channel, and then strobes to set the corner frequency on that channel. This operation can be performed from either the front panel with LOC (for local) selected or from the DEC DR11-C interface with REM (for remote) selected on the front panel.

Each of the filtered anemometer signals was digitized using a 16 channel, 150 KHz maximum sampling rate, 15 bit, simultaneous sample and hold A/D converter unit manufactured by Phoenix Data Inc. The model number of the A/D is DAS6915-10055-1. The A/D converter is interfaced to a DEC PDP11/84 minicomputer using a DEC DR11-B,W DMA interface module. A DEC RA81 500 M byte disk drive and a DEC TU81 high speed tape drive are used for storage of the data.

3.3 Calibration

The hot wires were calibrated using the digital linearizing scheme detailed by George et al. (1987). In its simplest form the velocity is expressed as the sum of powers of the voltages, that is

$$U = \sum_{n=0}^N A_n E^n \quad (3.3.1)$$

The principal advantages of this type of expression over the earlier schemes (Kings law, etc.) are two fold: First of all, linear least squares can be directly applied to equation (3.3.1) since the coefficients occur linearly and the principal uncertainty in the experimentally measured quantities is U which appears on the left side of (3.3.1). Second, application of the calibration to measured

voltage data is straightforward and essentially involves only recursive multiplication. In this set of experiments the exponent, N , was chosen as 4 so that (3.3.1) becomes

$$U = A_0 + A_1 E + A_2 E^2 + A_3 E^3 + A_4 E^4 \quad (3.3.2)$$

From experience in the Turbulence Research Laboratory it has been found that there is little to be gained by going beyond the 4th order.

The calibrations of the single wire rakes as well as the cross-wire rakes were performed in the same jet facility that the experiments were done in. This was justified because the exit turbulence intensity of the jet is very low as discussed in Section 3.1. This is important for calibration of hot wires because of the non linear relationship between bridge top voltage and velocity.

The calibration scheme for the single wire rakes was as follows. A calibrated pressure transducer was used to measure pressure drop through the contraction of the jet. The particular rake of probes to be calibrated was set up so that all of the individual hot-wire sensors were at the exit of the contraction. The blower RPM was then varied to achieve the velocity range of interest. The various sensor voltages and the pressure transducer voltage were digitized for each particular velocity in the range. With this set up, up to 15 probes could be calibrated at the same time. The velocity calibration range covered the entire range of velocities encountered in the experiment, and was typically 1 m/s -- 25 m/s. A flow chart showing the complete scheme needed to get real streamwise velocity values on disk is shown in Figure 3.3.1.

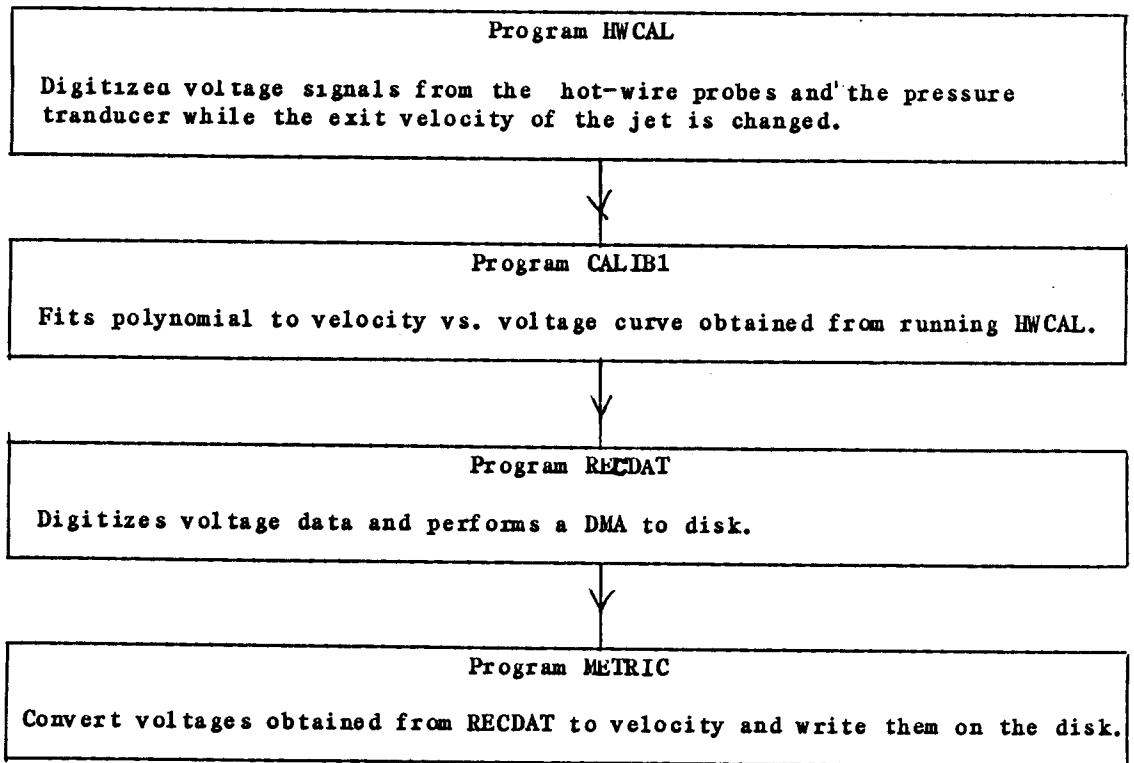


Figure 3.3.1 Flow chart showing method used to obtain streamwise velocities.

3.4 Cross-Wire Calibration

The calibration of the cross-wires utilized the same methods of Section 3.3 with the addition of an angle calibration scheme.

The cross-wire geometry is shown in Figure 3.4.1. Ang is the angle between the normals to the wires and β is the angle between U_0 and the flow axis. $\delta\beta$ is the misalignment angle which must be included because of the multiple probe rakes. Only one of the probes on the rake could be lined up with the flow axis because it is not feasible to fabricate the probes so that they all line up. In order to overcome this problem, one probe was chosen (as the reference) to line up with the flow axis. Any deviations from this reference by the remaining probes on the rake were then accounted for by the misalignment angle.

A form of Champagne-Sleicher Law was utilized to extract the u and v components of velocity from the cross-wire data. According to this formula, (Champagne and Sleicher 1967)

$$U_{\text{eff}1} = U_0 (\cos^2\phi_1 + k_1 \sin^2\phi_1)^{1/2} \quad (3.4.1)$$

$$U_{\text{eff}2} = U_0 (\cos^2\phi_2 + k_2 \sin^2\phi_2)^{1/2} \quad (3.4.2)$$

where $U_{\text{eff}1}$ and $U_{\text{eff}2}$ are the effective velocities seen by probes 1 and 2 respectively, k_1 and k_2 are the axial coefficients related to heat transfer for probes 1 and 2 respectively, and ϕ_1 and ϕ_2 are the angles between the vector U_0 and the normals to the respective probes.

Taking equation (3.4.1) dividing by (3.4.2) and then squaring, the following equation is found:

$$\frac{U_{\text{eff}1}^2}{U_{\text{eff}2}^2} = \frac{(\cos^2\phi_1 + k_1 \sin^2\phi_1)}{(\cos^2\phi_2 + k_2 \sin^2\phi_2)} \quad (3.4.3)$$

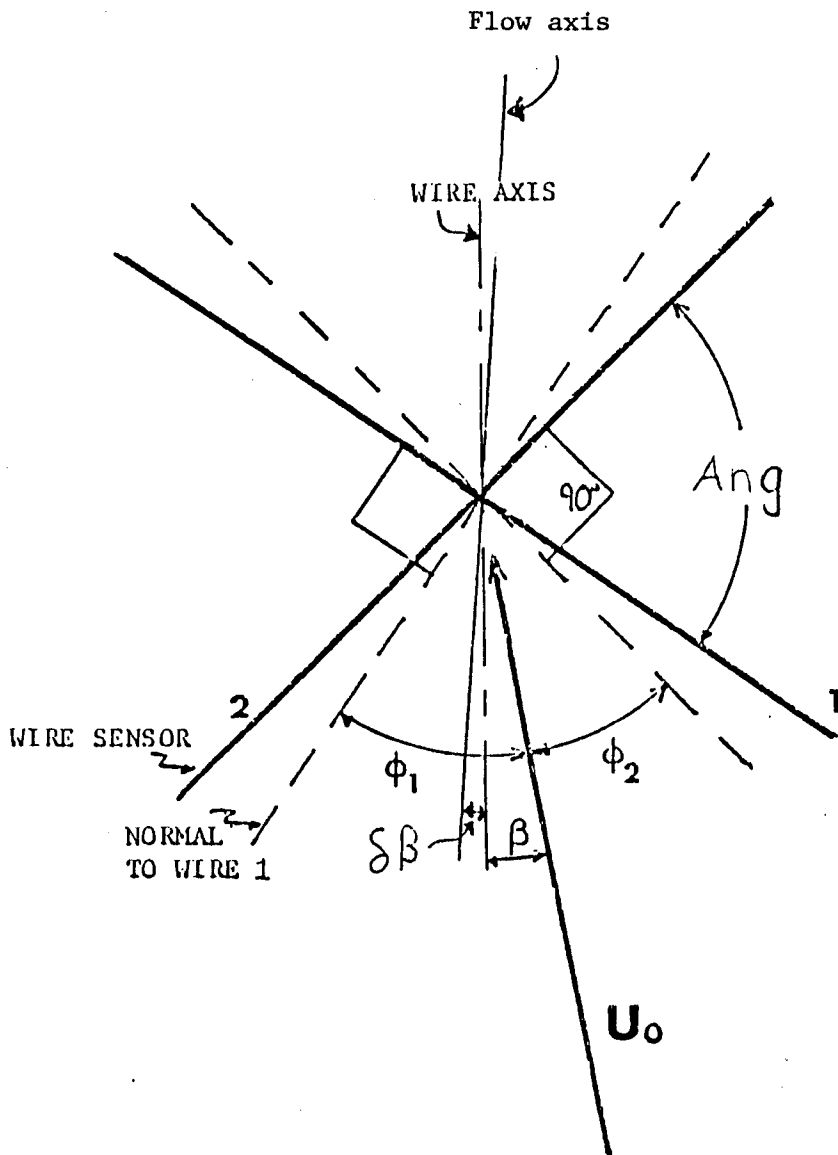


Figure 3.4.1 Cross-wire geometry.

Letting $\phi_2 = \text{Ang} - \phi_1$ using trigonometric identities, and several other manipulations, the following quadratic equations in $\tan \phi_1$ results:

$$D \tan^2 \phi_1 + E \tan \phi_1 + C = 0$$

where

$$D = (Bk_2 \cos^2(\text{Ang}) + B \sin^2(\text{Ang}) - k_1)$$

$$C = (B \cos^2(\text{Ang}) + B \sin^2(\text{Ang})k_2 - 1)$$

$$E = 2(B(1-k_2) \cos(\text{Ang}) \sin(\text{Ang}))$$

and

$$B = \left(\frac{U_{\text{eff}1}}{U_{\text{eff}2}} \right)^2 \quad (3.4.4)$$

Solving for $\tan \phi_1$ results in

$$\frac{-E + \sqrt{E^2 - 4DC}}{2D} \quad (3.4.5)$$

Since the physics of the probe imply that $\tan \phi_1$ must be greater than zero, the positive root of (3.4.5) is used. If the value under the square root sign is negative the solution cannot be determined. This situation has been termed dropout by Beuther et al. (1987). This generally occurs in regions of high local turbulence intensity such as positions on the low speed side of the jet mixing layer where flow reversals and/or any electronic noise, digital or analog can result in values that are not resolvable. The dropout in this experiment was at most 7% of the total number of data points in any single realization. These unresolvable points were replaced by the nearest resolvable point. This method was shown by Buchhave (1978) to bias the spectrum the least when compared to replacing the unresolvable points with zeros or the mean value of the particular realization.

Once ϕ_1 was solved for, U_0 and β could be calculated, then the particular velocity components become

$$U = U_0 \cos (\beta + \delta\beta) \quad (3.4.6)$$

$$V = U_0 \sin (\beta + \delta\beta) \quad (3.4.7)$$

where the sign of $\delta\beta$ depends on the particular probe misalignment with respect to the reference probe.

The angle calibration was performed in the following manner. Each probe was placed at 90 deg. to the flow axis and left there. The calibration for voltage versus velocity was then obtained in the same manner as for the single wire case discussed in Section 3.3. The angle calibration was carried out for each probe using the rig shown in Figure 3.4.2. First a voltage vs. angle curve was generated. Second, the voltage was converted to velocity using the previously obtained voltage versus velocity curve. This resulted in a curve of velocity vs. angle. This curve was then fitted with a form like equation (3.4.1) in order to obtain k for each wire. Once k was found for each wire the calibration was complete. It should be noted that k has been seen to be a function of velocity for velocities less than 1 m/s (Beuther et al. 1987). Over the range of velocities seen in this experiment however, k was essentially constant. A flow chart showing the complete scheme used to get u or v velocity values from the effective voltages is shown in Fig. 3.4.3.

3.5 Sampling Information

One of the major problems with digital sampling is the phenomenon of aliasing (Otnes and Enochson 1978). If, for instance, a sinusoid

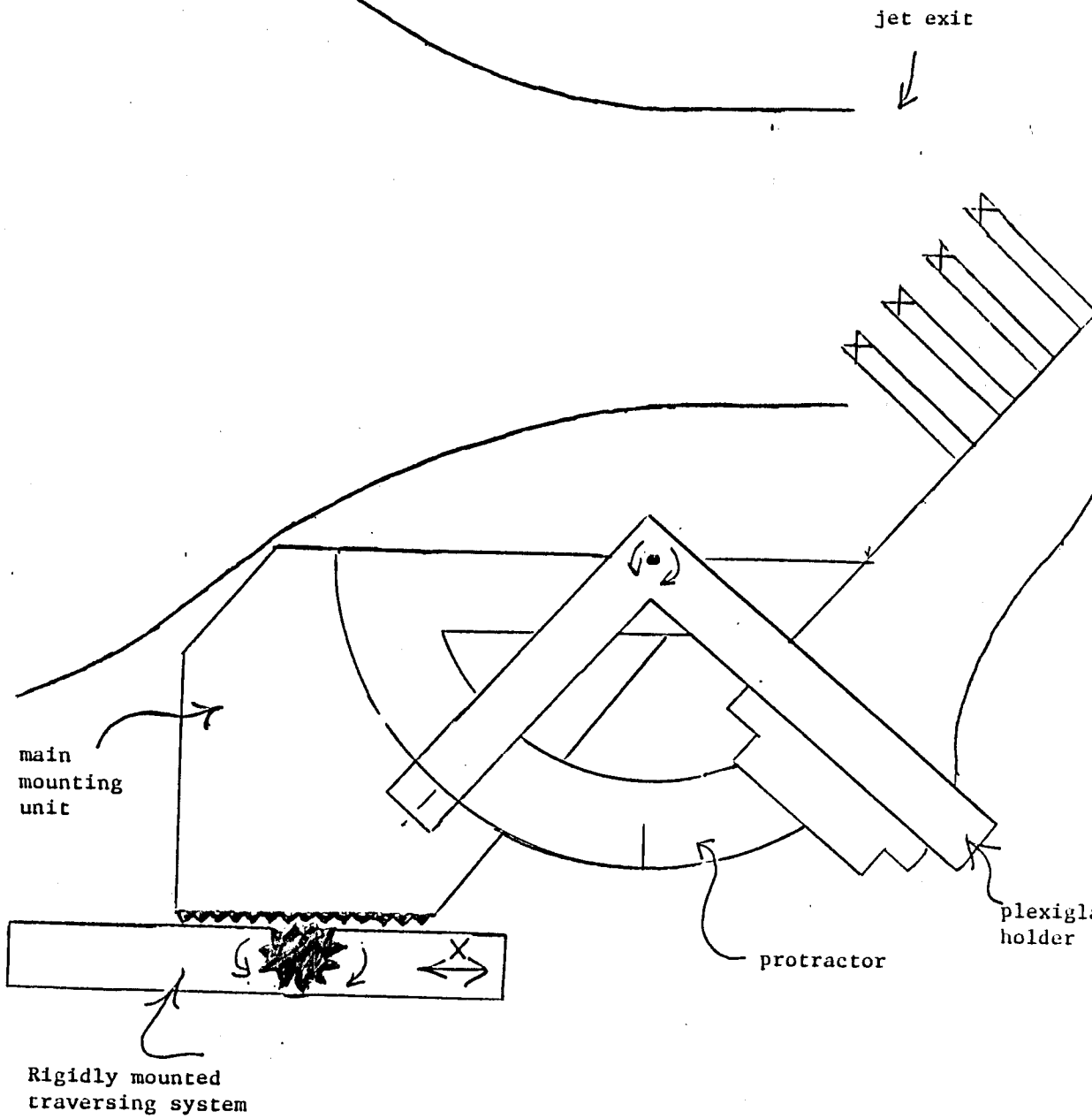


Figure 3.4.2 Rig for performing angle calibration of a rake of cross-wires.

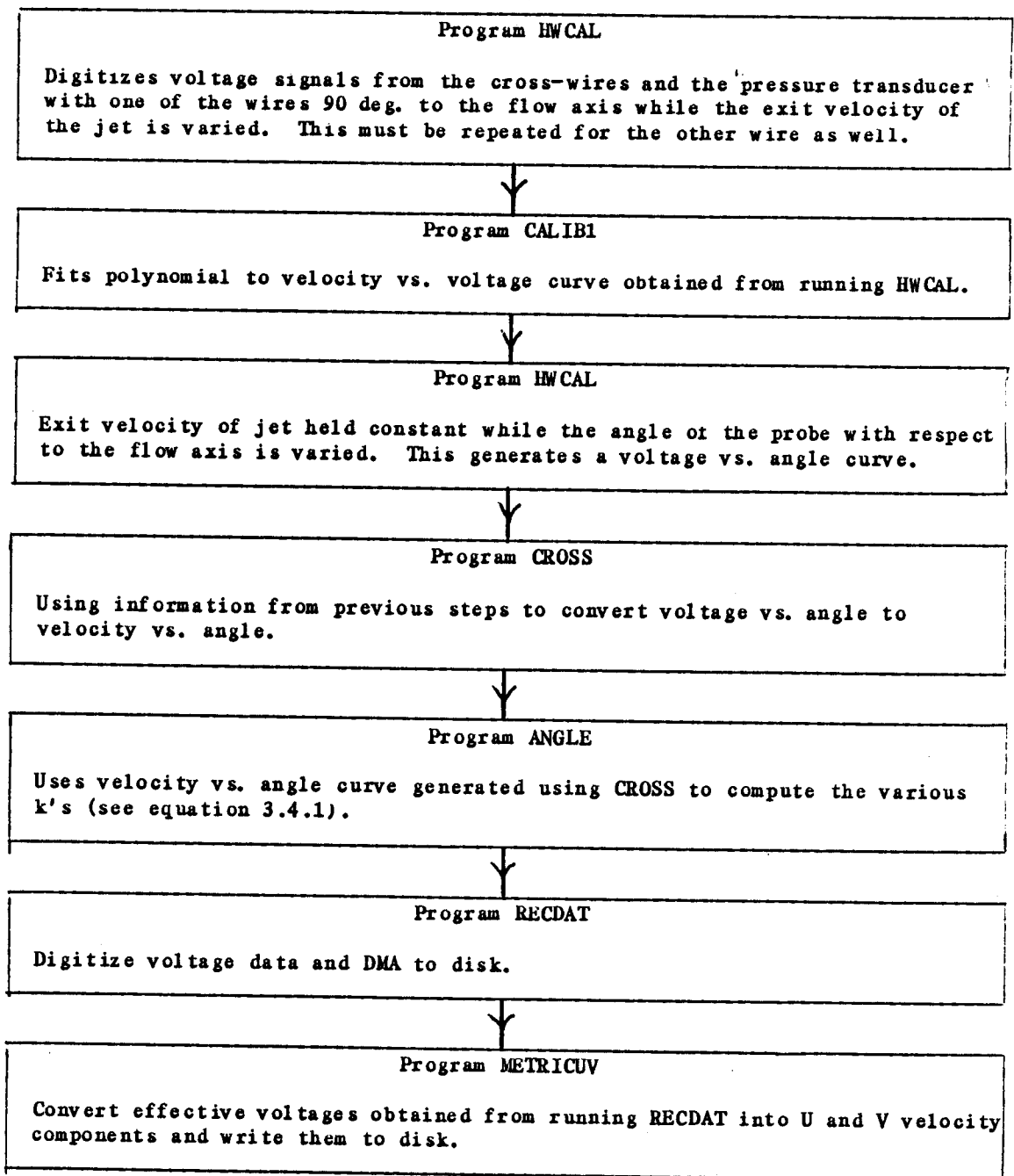


Figure 3.4.3 Flow chart showing method used to obtain u and v velocity values on disk.

whose frequency f is greater than one half the sampling frequency f_s , is sampled at f_s it will appear as a lower frequency. Because of this aliasing problem one should insure that either the sampling rate be twice the highest frequency in the flow or low pass filter at less than or equal to one-half the sampling rate. This constraint has been termed the Nyquist criterion.

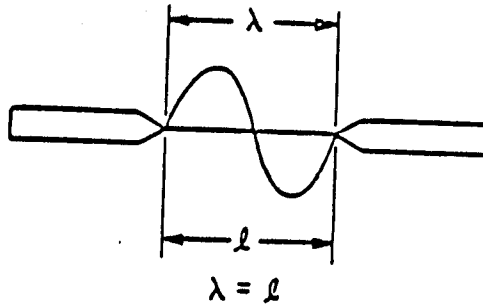
In the jet flow under consideration here the highest frequency can be estimated using the Kolmogorov length scale η to be about 7000 Hz. (i.e., $f_k = U_c / 2\pi\eta$). This would suggest that the sampling rate should be about 14,000 samples/sec. However, probe attenuation must be considered in this experiment. A sensor is only sensitive to disturbances with spatial scales that are larger than twice the largest dimension of the sensor. See Figure 3.5.1. Thus for a hot wire of length l_w and in a flow of convection velocity U_c ,

$$f_c = \frac{U_c}{2 l_w}$$

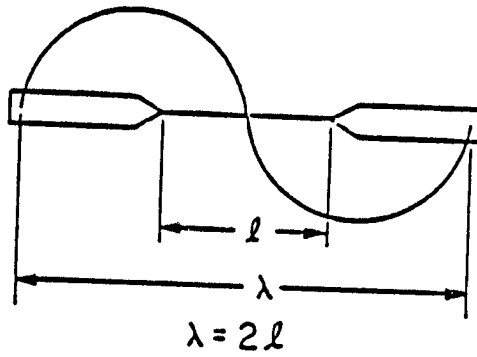
where f_c is the effective corner frequency due to the probe acting on a low pass filter. For the probes used in this experiment $l_w = 0.0012$ m and $U_c = 12$ m/s giving

$$f_c = 5000 \text{ Hz}$$

This would suggest that the sampling frequency should be above 10,000 Hz. This sampling rate was used in an initial experiment. When the spectra from this initial experiment were examined (see Figure 3.5.2) the energy content was seen to be small beyond 200 Hz. Since the thrust of this experiment has been to identify large eddies on an energy-weighted basis, anything beyond 400 to 500 Hz was considered



(b) - Non-resolvable Signal



(a) - Resolvable Signal

Figure 3.5.1 Probe roll-off example.

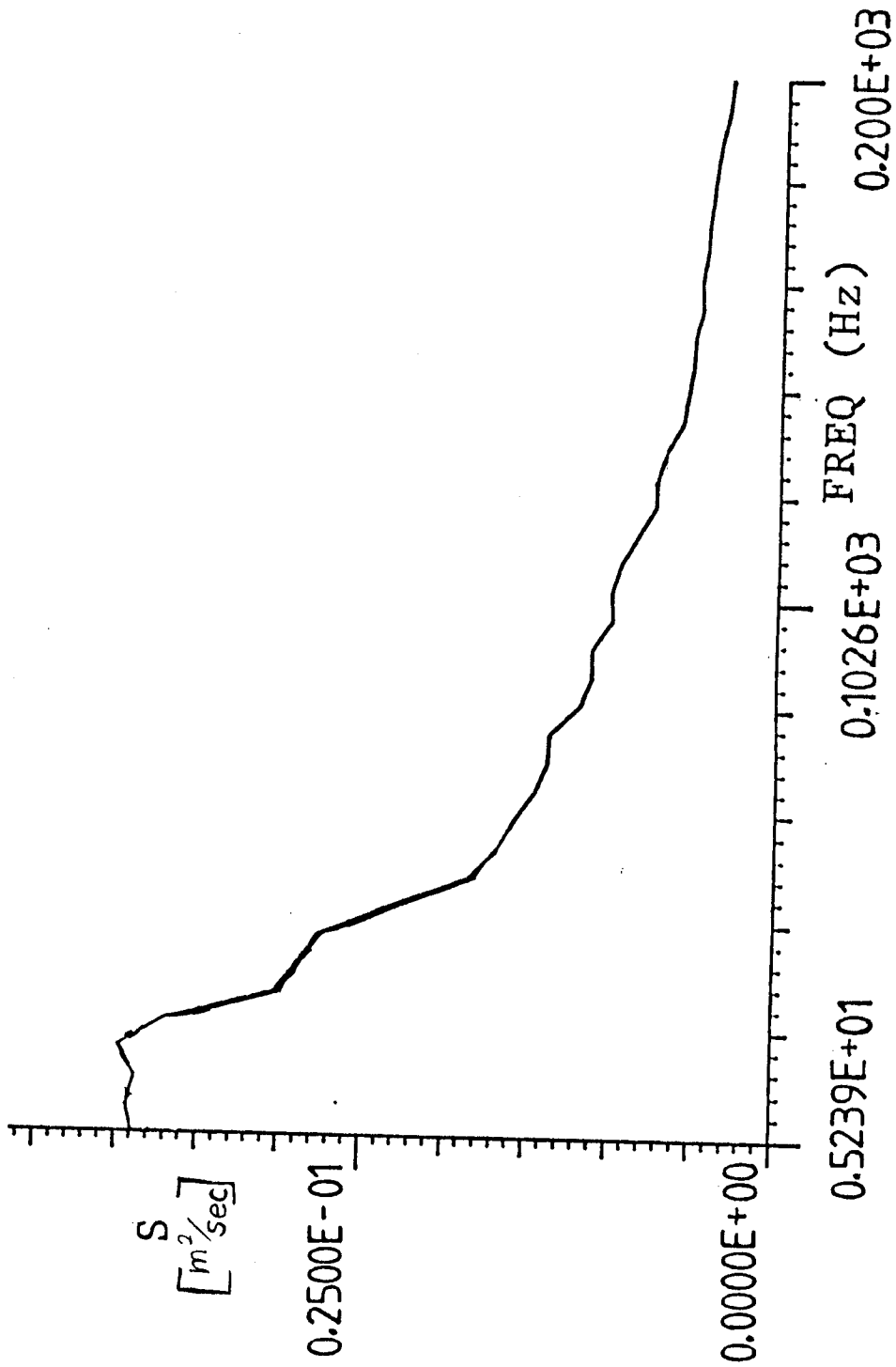


Figure 3.5.2 Linear plot of streamwise velocity spectrum near center of mixing layer at $x/D=3$. Note very little energy beyond 200 Hz.

negligible as far as its contribution to the large eddies is concerned. It should be noted that this is well into the $k^{-5/3}$ range of the velocity spectrum. Also, the smallest time scale for a typical eddy that can be resolved is dictated by the probe spacing and the appropriate convection velocity (since eddies smaller than this would not be seen by both probes). If it is assumed that the turbulence field is frozen then the time scale is approximately equal to $\Delta t \sim \Delta r / U_c$ where Δr is the probe spacing and U_c is the convection velocity. For the conditions of this experiment $\Delta t \approx 0.0015$ sec., and the resolvable bandwidth in frequency is approximately $1/\Delta t$ or 800 Hz. As was mentioned in This prompted the low pass filter cut off frequency to be set at 800 Hz for each filter. All 16 filters were phase matched to within 1 degree. The sampling rate was then set at 2 kHz which satisfies the above mentioned constraints (i.e. the signal should be low-passed at a maximum of one-half the sampling rate).

The number of samples taken per data block was 2048 for phases 1-3. This gave a total time record of 1 sec. This 1 sec. record length gave a bandwidth of $1/T = 1$ Hz. 300 such blocks were taken for each channel of anemometry. In order to insure statistical independence between blocks, the time interval between blocks was more than two integral time scales.

In phase 4 of the experiment, 1024 samples were taken for each block. It was determined from the previous phases that a one-half second record length (a bandwidth of 2 Hz) was adequate. The reduction by one-half of the number of points reduced by one-half the amount of storage needed and significantly reduced the computation time required. The time integral scale in this flow is approximately

equal to 0.0013 sec. so that the number of integral scales per time record was large for all phases (typically greater than 50).

CHAPTER 4

INSTANTANEOUS AND MEAN VELOCITY FLOW CHARACTERISTICS AND SPECTRAL ANALYSIS

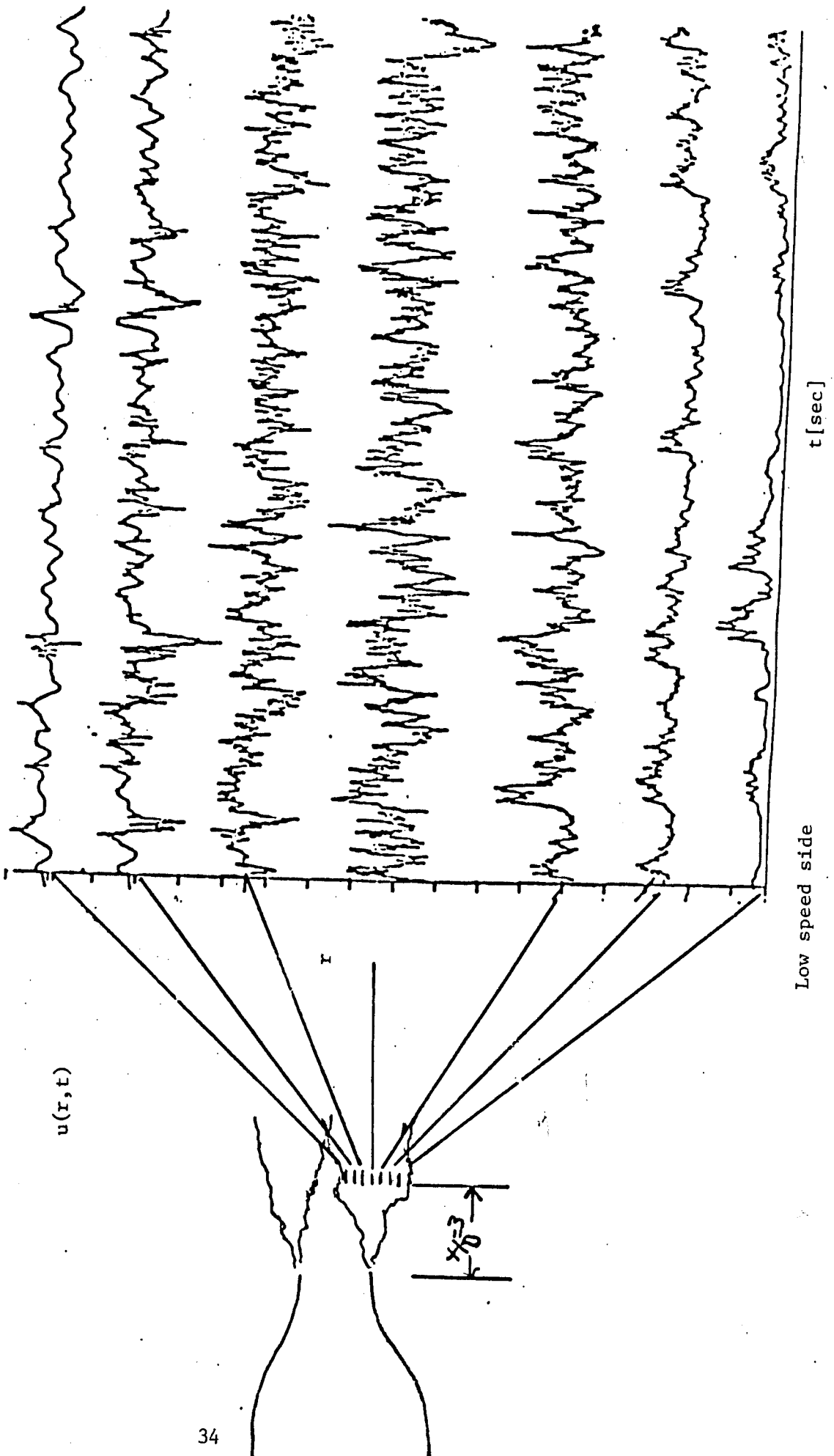
4.1 Instantaneous Velocities

At the high Reynolds numbers of the flow studied here ($Re_o \sim 10^5$), flow visualization experiments show little evidence of the well organized structures present at lower Reynolds numbers. The reason for this is not that they are not present (as is evident from the conditional sampling experiments of Hussain and co-workers (1986)), but that the flow is considerably more complex. One can appreciate the complexity of this flow by examining Figure 4.1.1 where one block of instantaneous streamwise velocities for seven radial locations are shown plotted as a function of time. The marked difference in the amplitude and frequency content of the signals is obvious. Note the increasing intermittency toward the outer edges and the lack of any obvious organized events. These plots should convince even the most skeptical of the need for a statistical approach to turbulence, and to the search for coherent structures.

4.2 Velocity Moments Across the Mixing Layer

The mean flow characteristic at $x/D=3$ are examined and compared with those of other researchers to insure that the data base is valid. It should be noted that the following profiles are from a single azimuthal position. Measurements were taken at twenty-five azimuthal positions at an axial position of $x/D=3$. The profiles shown are typical results, the other profiles at different azimuthal positions being within 8% of these.

Potential core

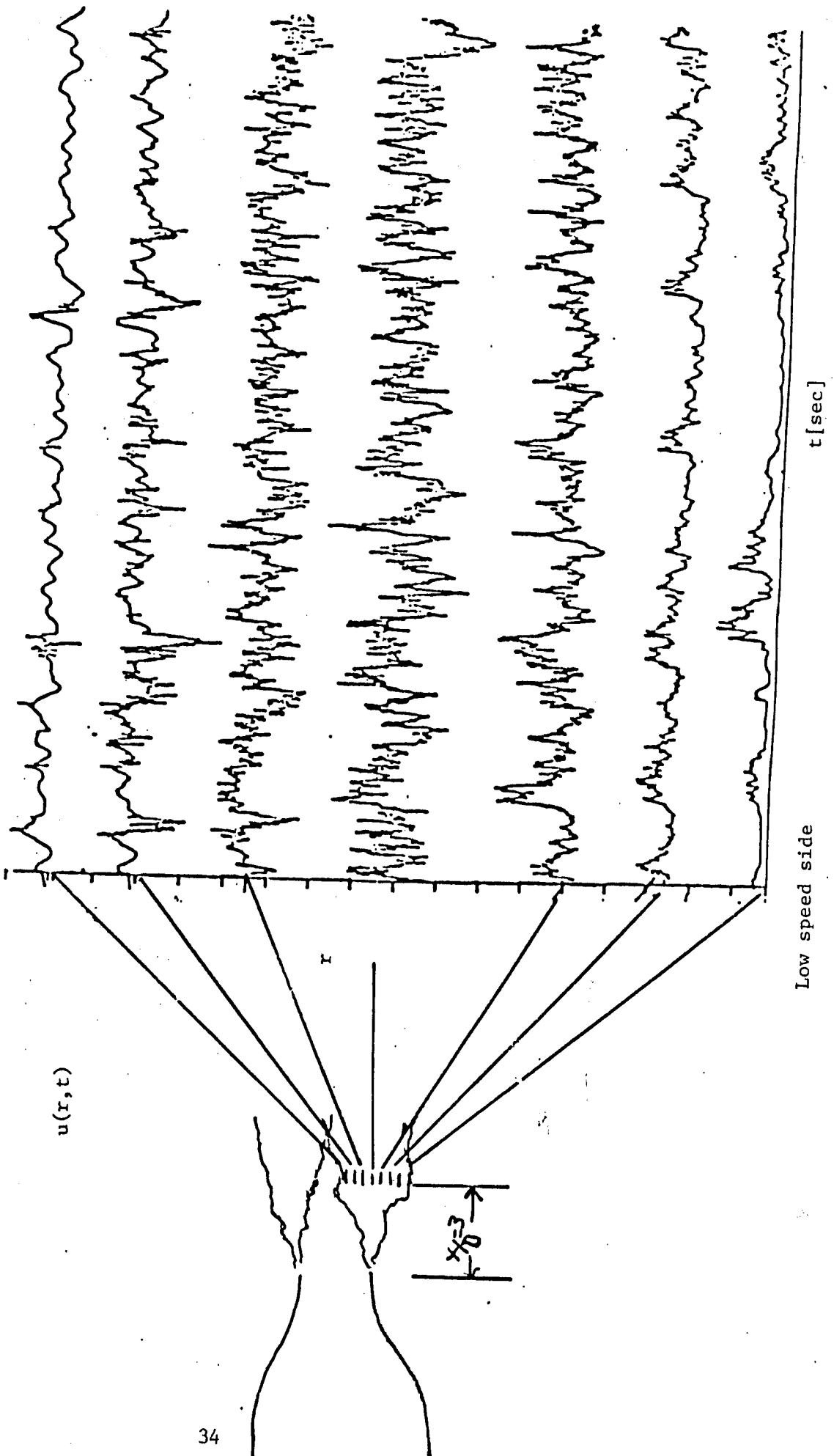


Low speed side

t [sec]

Figure 4.1.1 Instantaneous streamwise velocity

Potential core



Low speed side

t [sec]

Figure 4.1.1 Instantaneous streamwise velocity

Figures 4.2.1 - 4.2.4 show measurements of the mean velocity, U , the streamwise and cross-stream rms velocity fluctuations, u', v' , and the Reynolds stress, \overline{uv} , respectively as a function of radius. U , u' , and v' have been normalized by the exit velocity, U_e and \overline{uv} by U_e^2 . The above moments were calculated using more than 1000 statistically independent samples.

The measurements are compared to those of Hussain and Clark (1981) in Figures 4.2.5-4.2.7. They used the local momentum thickness defined as

$$\theta_m = \int_0^{\infty} (U/U_m)(1-U/U_m)dr \quad (4.2.1)$$

to check for similarity in the jet shear layer. In order to compare this latest data with that of Hussain and Clark (1981) the momentum thickness was calculated at $x/D=3$. The value of θ_m in our experiment at $x/D=3$ was found to be 1.37 cm, corresponding to $\theta_m/x = .046$. From Figures 4.2.5-4.2.7 it can be seen that the various quantities compare quite well with those of Hussain and Clark (1981).

4.3 Spectral Analysis Technique

As has been mentioned earlier, the goal of this experiment was to apply and evaluate the General Orthogonal Decomposition in a high Reynolds number flow. In order to demonstrate that indeed this is a high Reynolds number flow, a streamwise spectrum at the center of the mixing layer at $x/D=3$ is shown plotted in Figure 4.3.1. It should be noted that this spectrum is not low-pass filtered so that it had to be sampled at 11 kHz (as was discussed in Chapter 3) in order to avoid aliasing. This spectrum shows at least two decades of a $k^{-5/3}$ range indicating a high Reynolds flow. The rolloff in this case can be

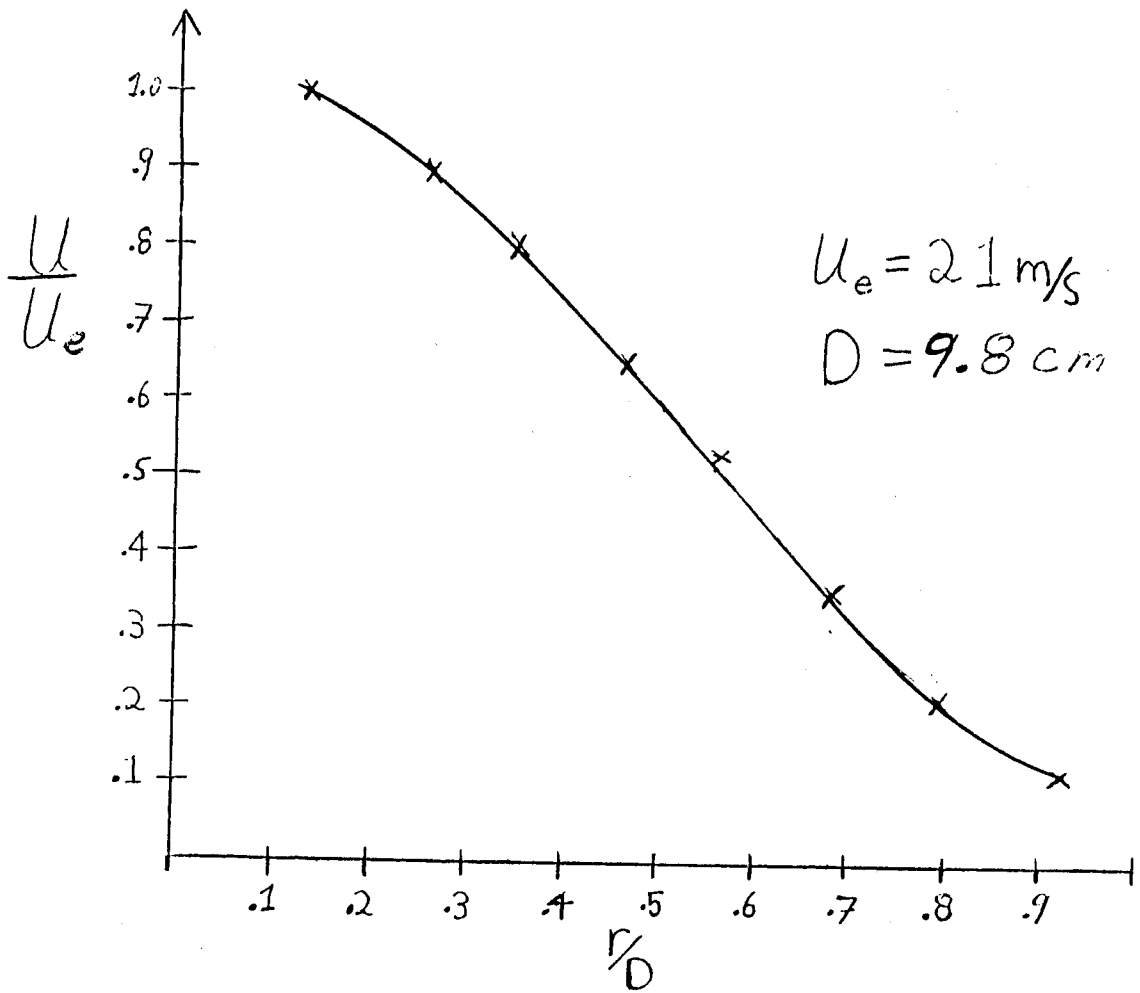


Figure 4.2.1 Mean Streamwise Velocity at $x/D=3$ vs. Radius in the Jet Mixing Layer.

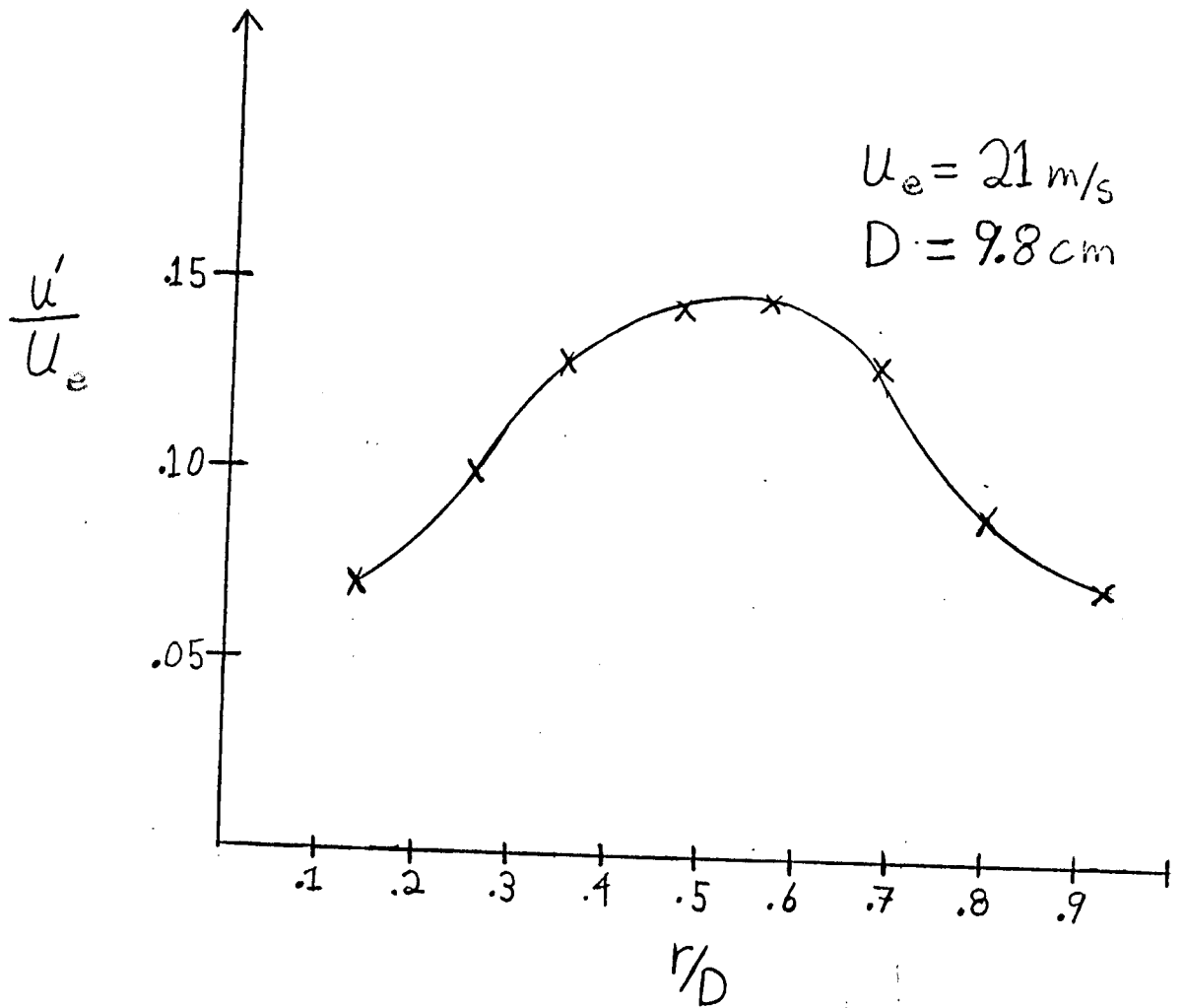


Figure 4.2.2 RMS Streamwise Velocity at $x/D=3$ vs. Radius in the Jet Mixing Layer.

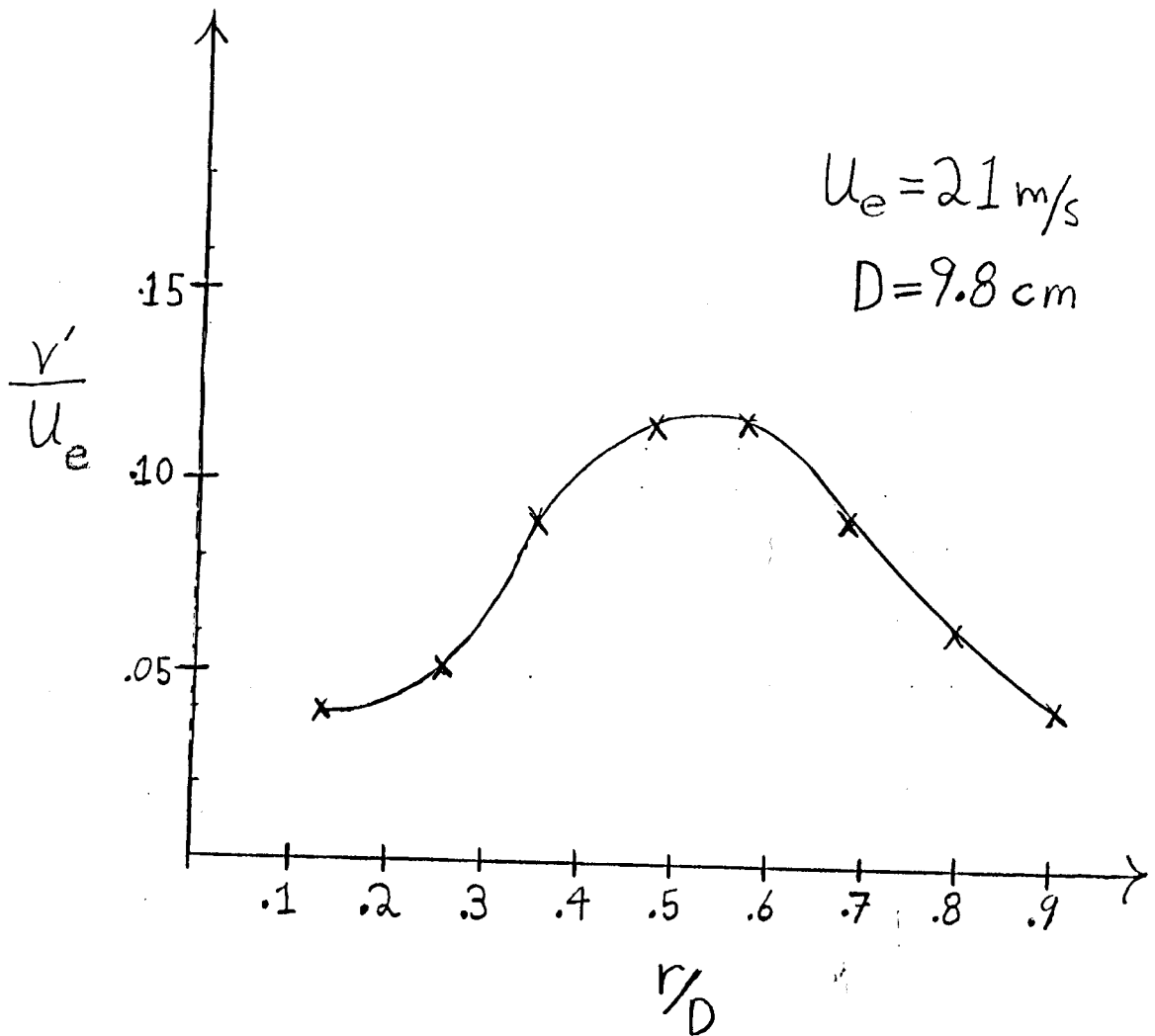


Figure 4.2.3 RMS Radial Velocity at $x/D=3$ vs. Radius in the Jet Mixing Layer.

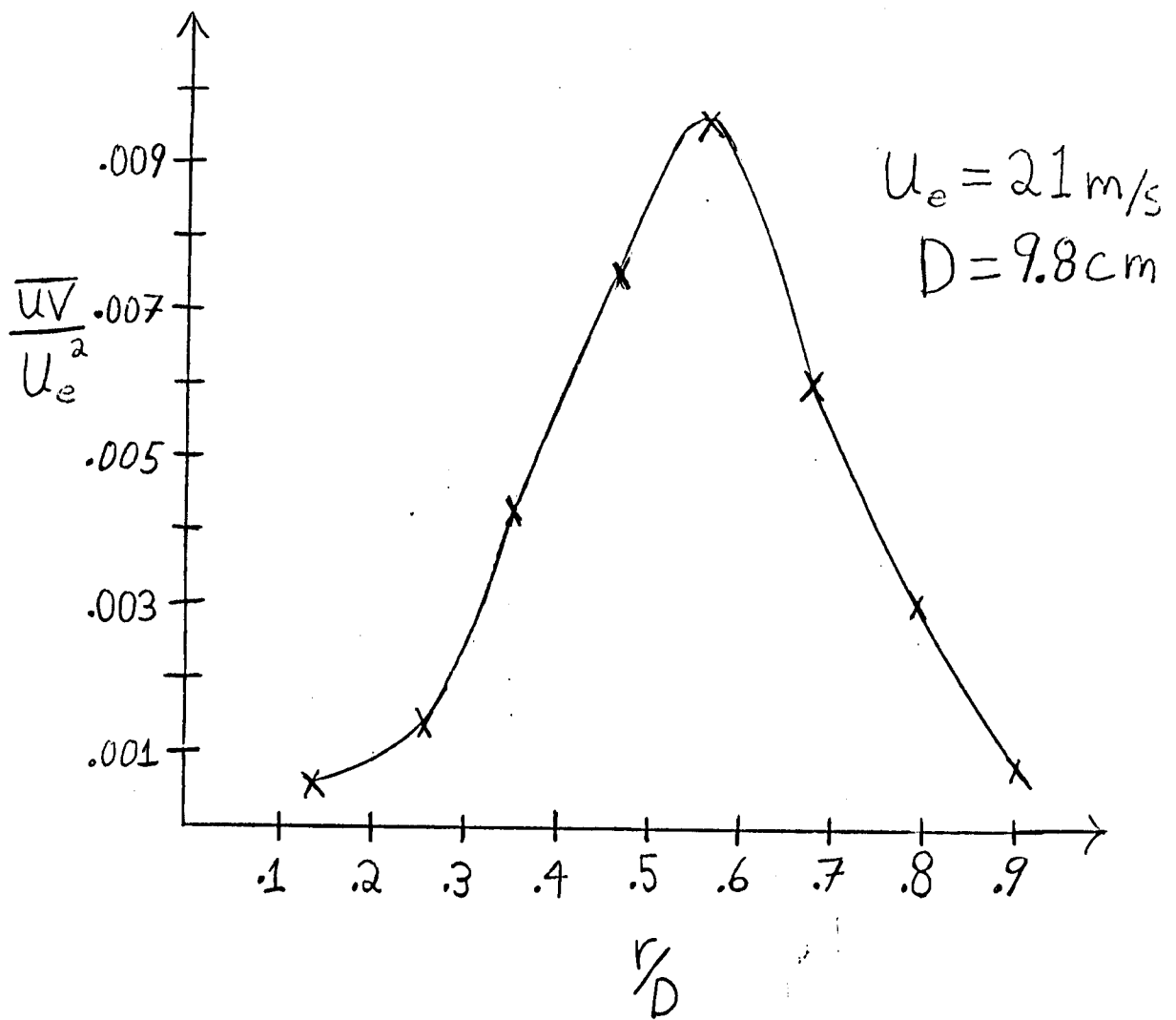


Figure 4.2.4 \overline{uv} at $x/D=3$ vs Radius in the Jet Mixing Layer.

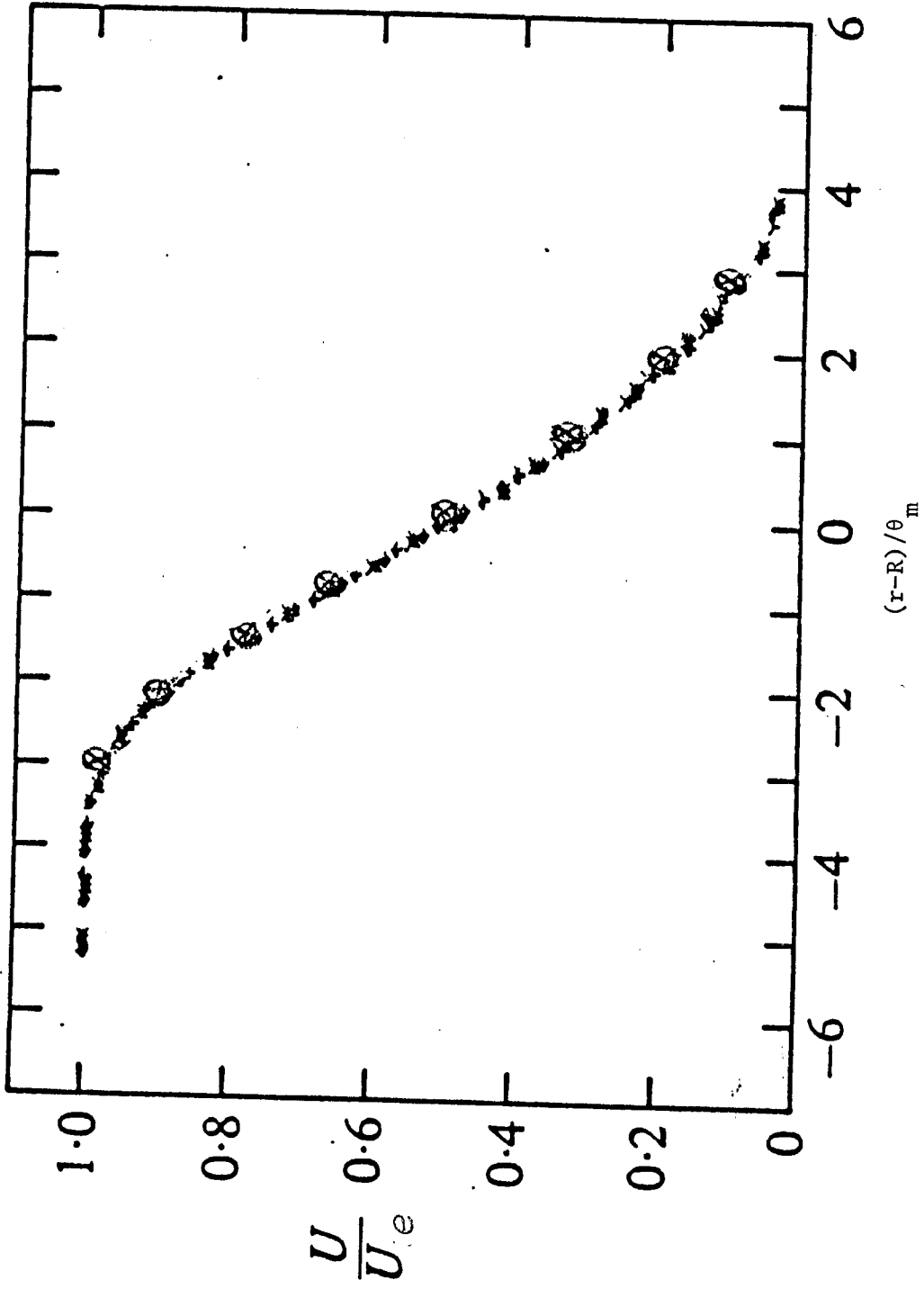



Figure 4.2.5 Mean values of Glauser  super-imposed on those of Hussain and Clark.

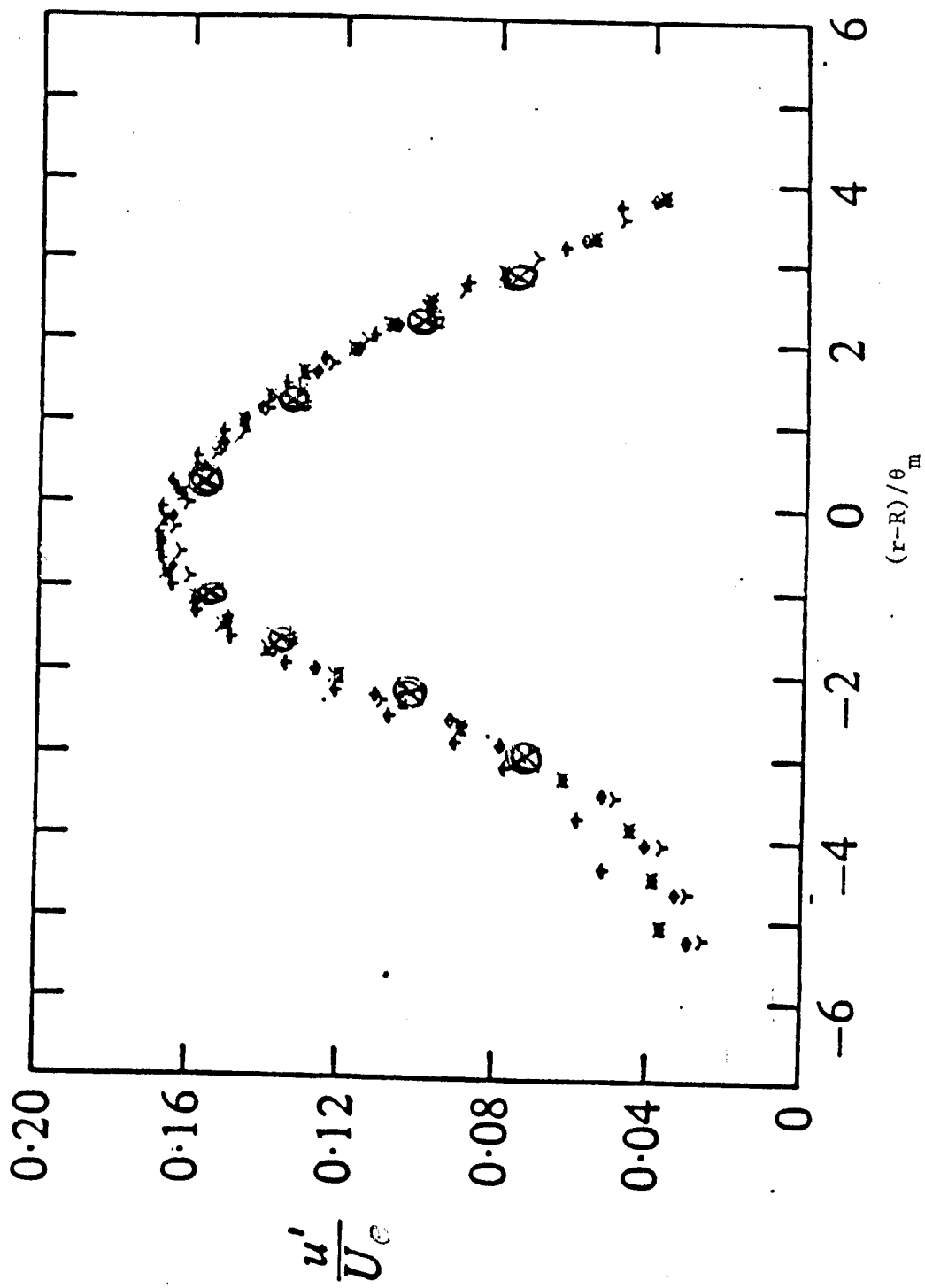


Figure 4.2.6 Streamwise R.M.S. velocities of Glauser \otimes super-imposed on those of Hussain and Clark.

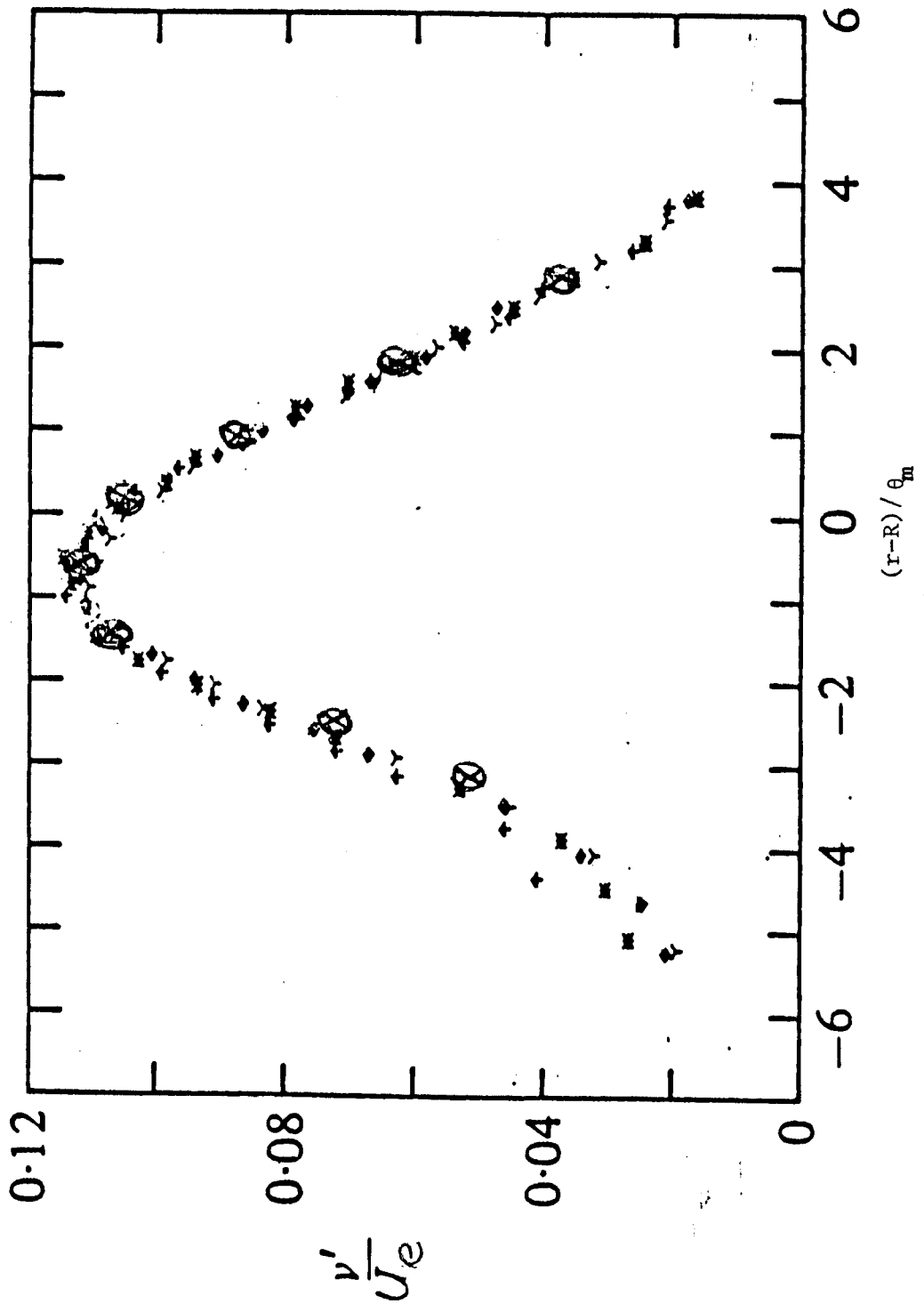


Figure 4.2.7 Radial R.M.S. velocities of Glauser ⊗ super-imposed on those of Hussain and Clark.

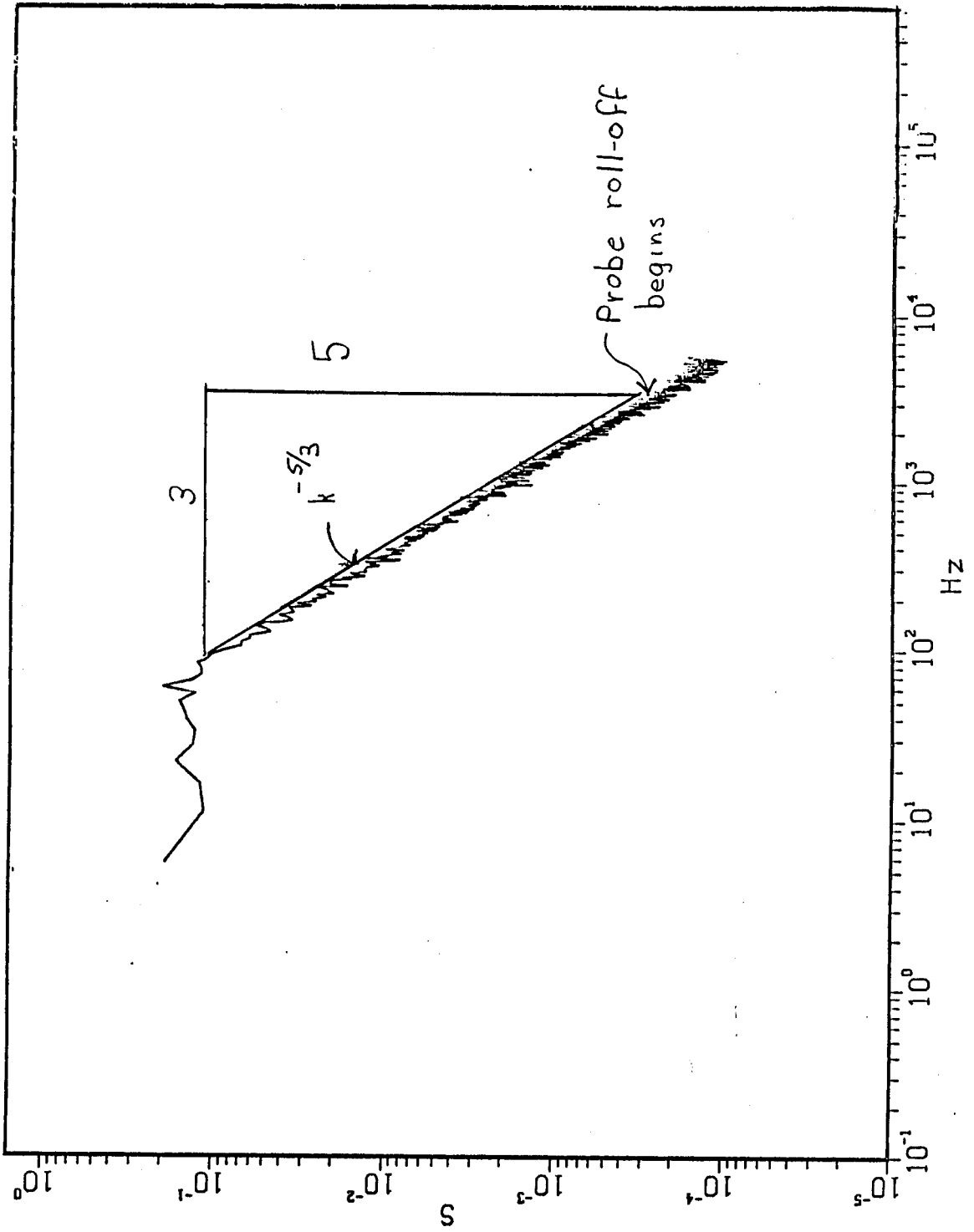


Figure 4.3.1 Unfiltered velocity spectrum near center of mixing layer at $x/D=3$ showing extended $k^{-5/3}$ range.

attributed to probe filtering as discussed in Chapter 3.

The time 'direction' in the jet being studied is stationary so that the general orthogonal decomposition reduces to the harmonic decomposition in this case. This motivates the use of Fourier analysis. Since the eigenfunction in the time domain are known, it is more convenient to directly form the Fourier transform of the incoming data (via FFT) and compute the space-frequency cross-spectrum than to work with the space-time cross correlation.

The Fourier transforms of a stationary random signal can be written as

$$\hat{u}(f) = \int_{-\infty}^{\infty} e^{i2\pi ft} u(t) dt \quad (4.3.1)$$

For the transform to exist in the normal sense $u(t)$ must satisfy certain conditions such as smoothness and vanishing at infinity. Stationary random signals do not in general satisfy the conditions necessary for the transforms to exist. If, however, one agrees to work in the domain of generalized functions, the infinite length signal is then approached as the limit of a sequence of functions whose Fourier transforms exist. The Fourier transform of the stationary random signal is then defined as the limit of the Fourier transforms of the members of the sequence. Under a certain set of conditions (v. Lighthill 1964) this limit can be assumed to exist. Therefore the Fourier transforms of $u(t)$ can be written as in equation (4.3.1) if it is understood that this is the Fourier transform of $u(t)$ in the sense of generalized functions (Lighthill 1964, George 1978, Lumley 1970)

It can be shown that a consequence of stationarity is that the Fourier coefficients are uncorrelated at different frequencies, i.e.

$$\overline{\hat{u}(f) \hat{u}^*(f')} = 0 \quad f \neq f' \quad (4.3.2)$$

$$\text{or } \overline{\hat{u}(f) \hat{u}^*(f')} = S(f) \delta(f-f') \quad (4.3.3)$$

where $S(f)$ is the spectrum of the signal $u(t)$ and $\delta(f-f')$ is the delta function.

The random signals obtained in the lab cannot be of infinite length so that a finite time Fourier transform must be defined (George 1978),

$$\hat{u}_T(f) = \int_{T/2}^{T/2} e^{i2\pi ft} u(t) dt \quad (4.3.4)$$

One can view equation (4.3.4) as the product of a finite length boxcar window i.e. $W_T(t)$ (Figure 4.3.2a) and an infinitely long time history $u(t)$ as shown in Figure 4.3.2b. Therefore, equation (4.3.4) can be written as

$$\hat{u}_T(f) = \int_{-\infty}^{\infty} u(t) W_T(t) e^{i2\pi ft} dt \quad (4.3.5)$$

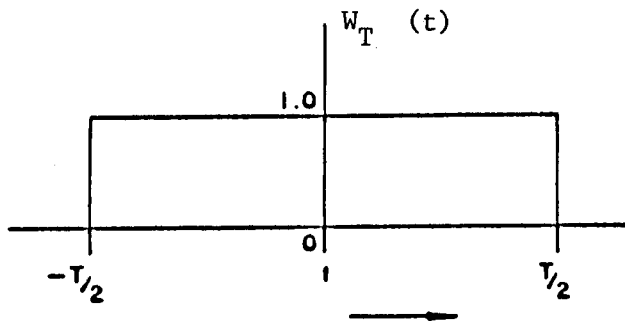
Using the fact that products in time transform into convolutions in frequency the Fourier transform of equation (4.3.5) can be written as

$$\hat{u}_T(f) = \hat{u}(f) * W_T(f) \quad (4.3.6)$$

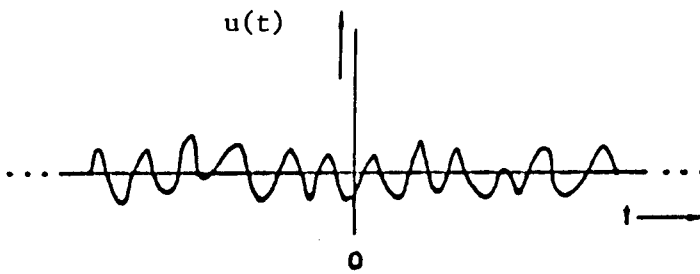
where

$$W_T(f) = \int_{-T/2}^{T/2} W_T(t) e^{i2\pi ft} dt \quad (4.3.7)$$

From equation (4.3.7) the effective filter shape is as seen in Figure 4.3.3. Because of the convolution of the true transform with



(a)



(b)

Fig.4.3.2 (a) Boxcar function for the FFT; (b) Sample time history of length T .

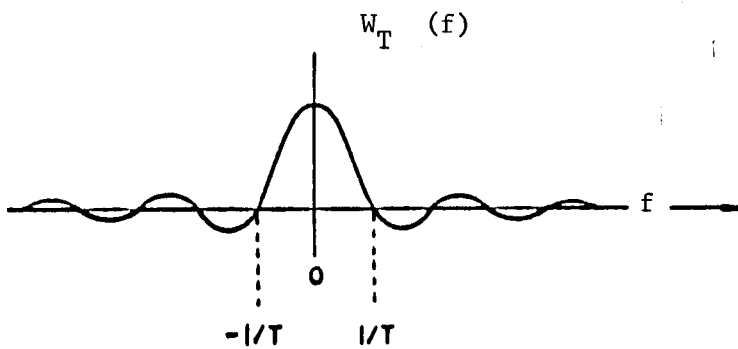


Fig.4.3.3 Effective filter shape with no tapering.

the window, there is a leakage of spectral information from a single frequency into a band of frequencies. Since the initial experiments showed the effects of this window on the measured spectrum to be negligible, no attempt was made to improve on the negative effect of this window by tapering or selection of a different window (v. Otnes and Enochson, 1978).

The discrete form of equation (4.3.4) (shifted in time by $T/2$) can be written as

$$\hat{u}_k = \Delta t \sum_{i=0}^{N-1} u_i \exp \left[j \frac{2\pi i k}{N} \right], \quad k=0,1,\dots,N-1 \quad (4.3.8)$$

where $f = k \cdot \frac{1}{T}$ and $t = i\Delta t$. The discrete transform equation (4.3.8) was carried out on VAX 8600 computer using a Fast Fourier Transform algorithm (from Moin at NASA Ames). The spectra were then computed using the discrete form of equation (4.3.2) which is (George 1978, Tan-atichat and George 1985)

$$\frac{\overline{\hat{u}_k \hat{u}_k^*}}{T} = S_k(r, f, \theta) \quad (4.3.9)$$

where the overbar denotes ensemble average and T is the record length.

In short the process was as follows:

- 1) Compute \hat{u}_k using the FFT.
- 2) Multiply \hat{u}_k times its complex conjugate and divide by T to get the spectrum.
- 3) Ensemble average over many (300 typically) independent spectral estimates as suggested by equation (4.3.9) to obtain S_k . The rate of convergence of our spectral estimate (George

1978) is the same as for any ensemble average (i.e. $\epsilon \sim \frac{1}{\sqrt{N}}$) where N is the number of independent spectral estimates and ϵ is the percent variability of our spectral estimator.

The cross spectra (between different components of velocity and spatially separated velocity components) were computed using an equation similar to (4.3.9) written as

$$\frac{\overline{\hat{u}_i \hat{u}_j^*}}{T} = \Phi_{ij}(r, r', f, \theta, \theta') \quad (4.3.10)$$

where i and j denote vector components and the prime emphasizes that the transformed signals come from different spatial points.

As with the standard spectra, these cross-spectra must be block-averaged to reduce the variability. The constraints on minimum record length can be more severe than that for the spectrum and a significantly longer record may be required for cross-spectra than for spectra (v. Tan-atchat and George 1985). This can be seen from the finite time cross-spectral estimator which can be shown to be given by

$$\Phi_{ij}(f) = \int_{T/2}^{T/2} C_{ij}(\tau) e^{-i2\pi f \tau} \left[1 - \left|\frac{\tau}{T}\right|\right] d\tau \quad (4.3.11)$$

where C_{ij} is the cross-correlation tensor. Unlike the autocorrelation, the cross-correlation does not in general peak at $\tau=0$ and in fact may have its peak far from the origin. Thus, the record length must be long enough to insure that the factor $(1 - \frac{\tau}{T})$ makes a negligible contribution over any region where C_{ij} differs from zero. Since the experiments in the jet were performed at one streamwise location ($x/D=3$) this record length effect is not severe because the phase differences across the shear layer and in the azimuthal direction are small. This results in the cross-correlation peaking near the origin.

A 20 percent bandwidth digital smoothing filter was then utilized to reduce the fluctuations even further. This filter did not affect the phase over the frequency band of interest in this experiment (v. Oppenheim et al. 1983).

Spectral and Cross-Spectral Results

Spectra of the streamwise and radial velocity fluctuations for eight radial positions in the jet shear layer ($r/D=.13$ - $r/D=.9$) are shown plotted in Figures 4.3.4 and 4.3.5 respectively. All of the spectra around the center of the mixing layer and on the low speed side of the shear layer have at least one full decade of a $k^{-5/3}$ range. The reason that the $k^{-5/3}$ range does not extend further is due to the effect of the low pass filter described in Chapter 3.

In and near the potential core ($r/D=.13$, $r/D=.24$, $r/D=.35$) all of the various spectra have a maximum away from the origin. As one progresses away from the potential core toward the center of the mixing layer ($r/D=.46$) the radial velocity spectrum still exhibit this maximum away from the origin. The streamwise spectrum, however, now has its maximum at the origin.

Just to the low speed side of the center of the mixing layer ($r/D=.57$) the streamwise spectrum has its maximum at the origin. The radial velocity spectrum, however, still exhibits a maximum away from the origin. At the remaining positions on the low speed side of the shear layer ($r/D=.68$, $r/D=.79$, $r/D=.90$) all of the various spectra have their maximum at the origin.

The Reynolds stress cross-spectrum between two positions ($r/D=.68$, $r/D=.79$ at $\Theta=0$) is shown plotted in Figure 4.3.6. Figure 4.3.6(a) is a plot of the co-spectrum and Figure 4.3.6(b) is a plot of

the quad spectrum. 4800 such cross-spectra were computed (between all r , r' , θ , θ' and different velocity components combinations). This one example is given to show that the cross-spectra are reasonably smooth. This indicates that an adequate number of independent cross-spectral estimates were obtained.

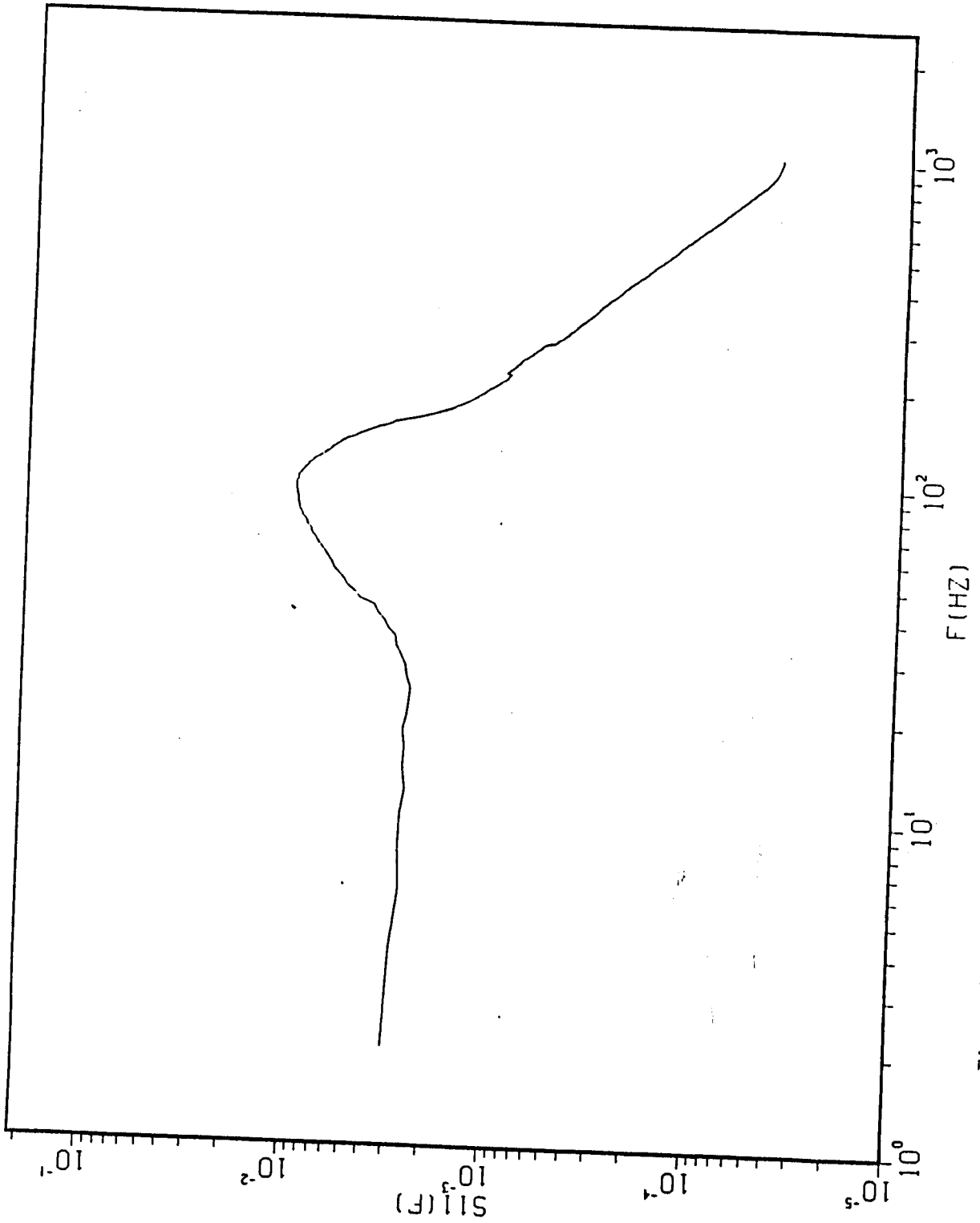


Figure 4.3.4 (b) Streamwise velocity spectrum at $r/D=.24$, $x/D=3$.

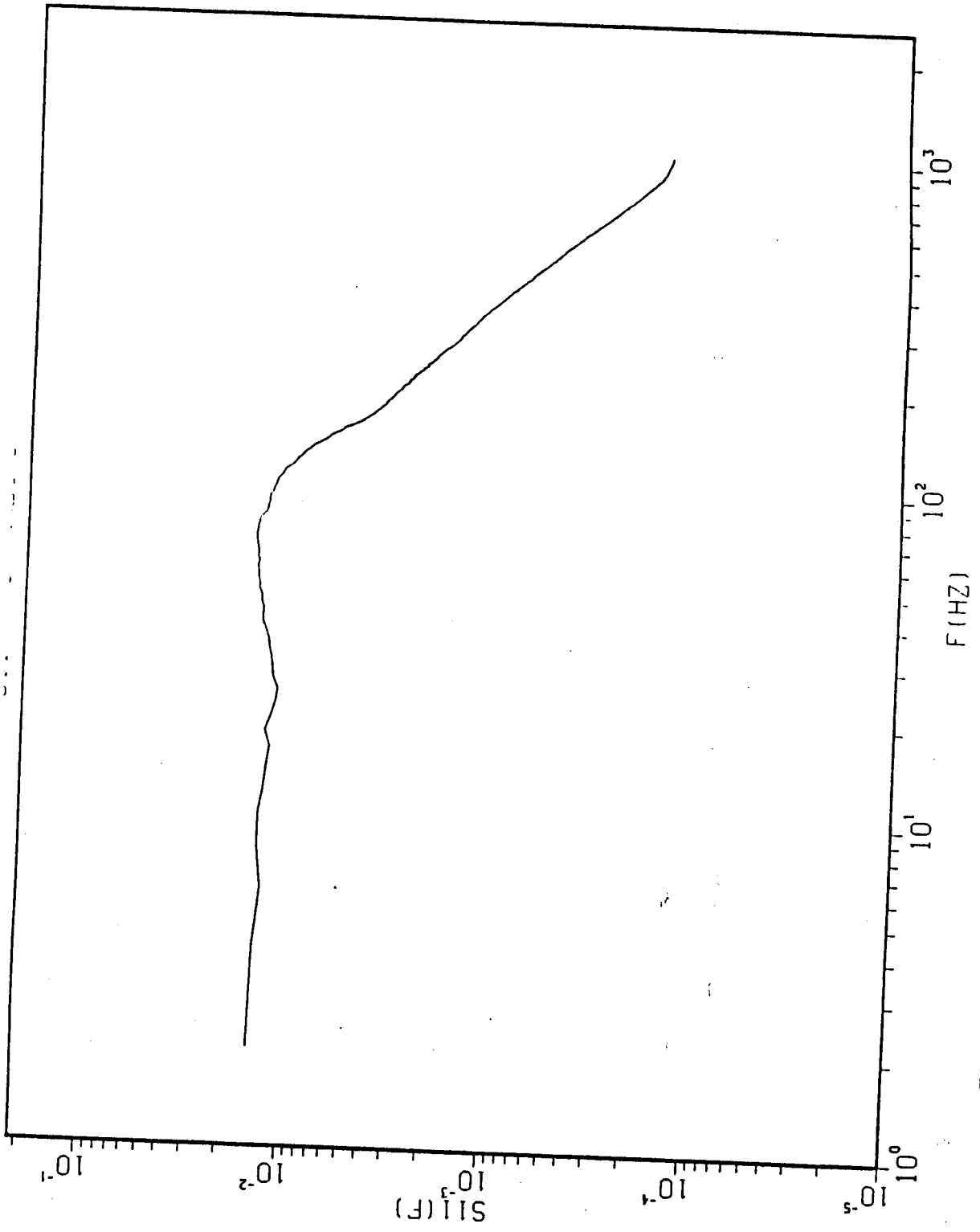


Figure 4.3.4(c) Streamwise velocity spectrum at $r/D=0.35$, $x/D=3$.

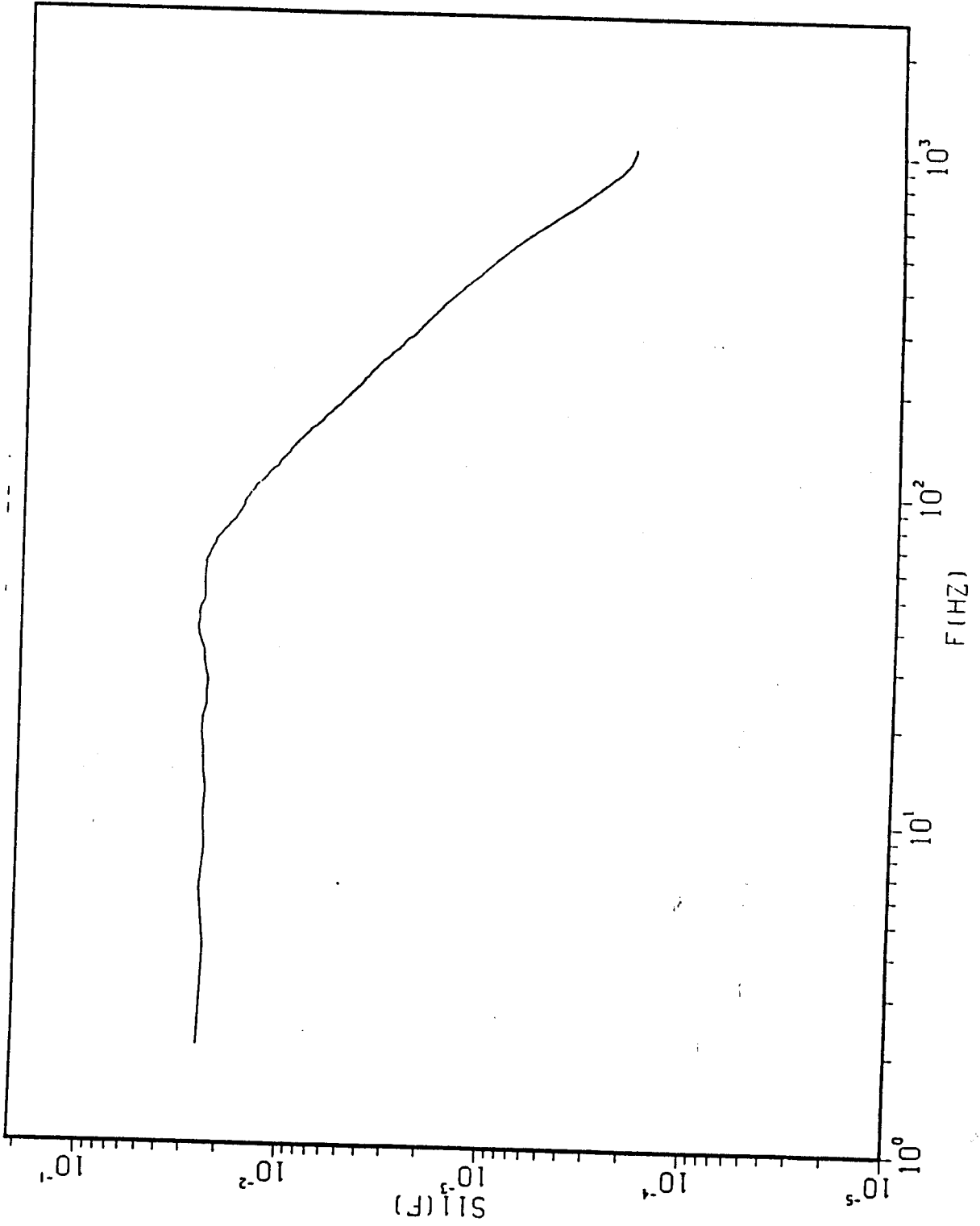


Figure 4.3.4(d) Streamwise velocity spectrum at $r/D=.46$, $x/D=3$.

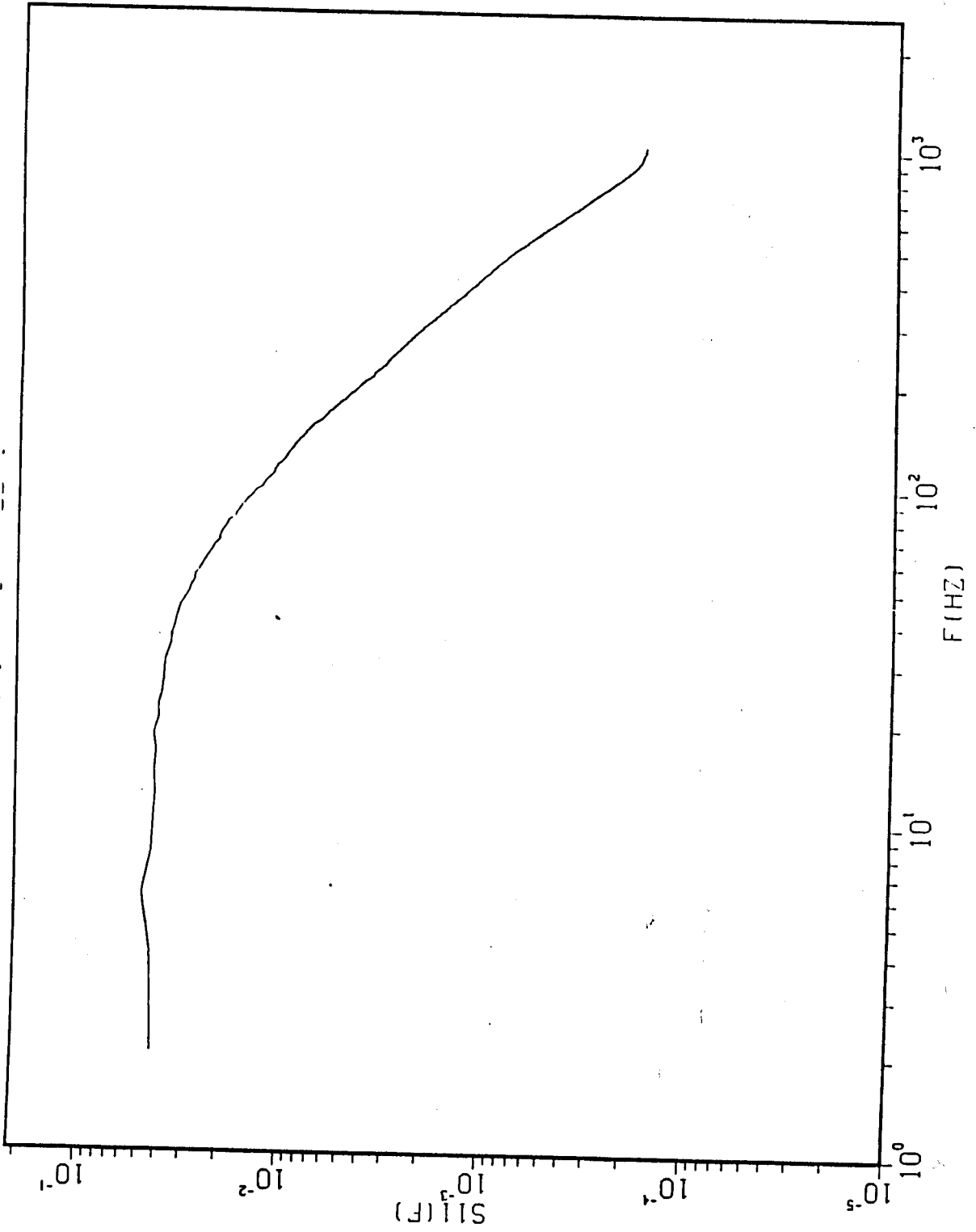


Figure 4.3.4 (e) Streamwise velocity spectrum at $r/D=0.57$, $x/D=3$

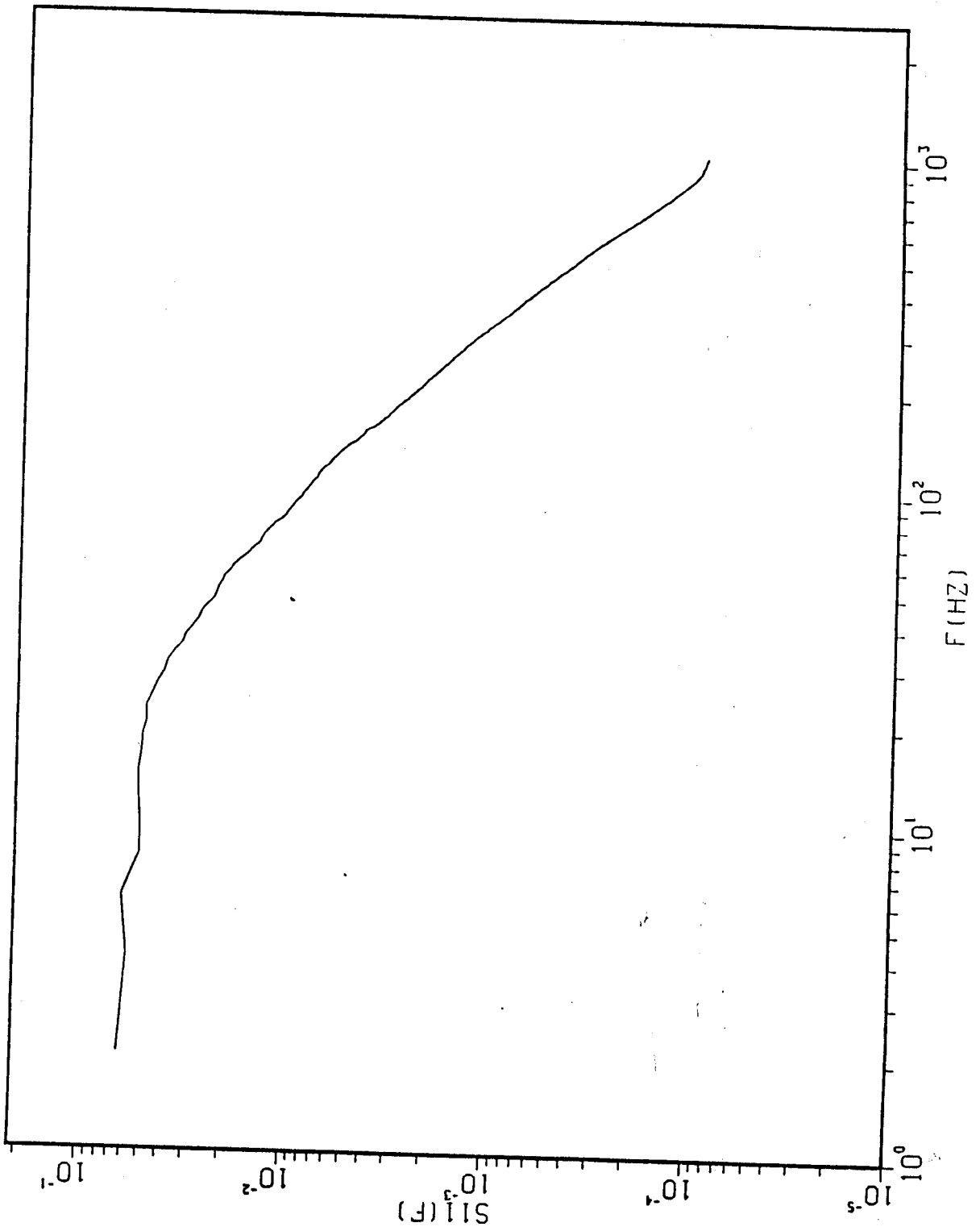


Figure 4.3.4 (E) Streamwise velocity

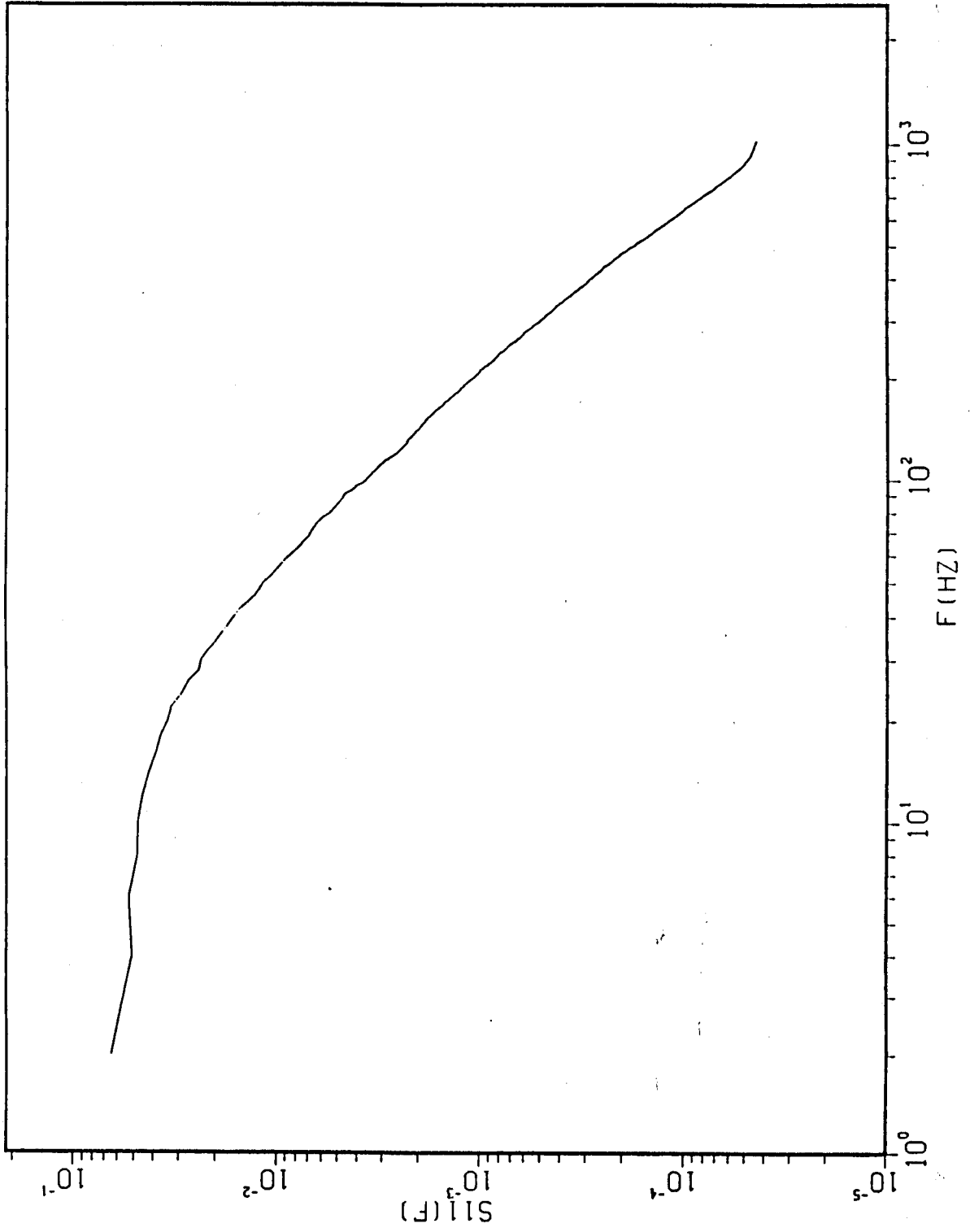


Figure 4.3.4(g) Streamwise velocity spectrum at $r/D=.79$, $x/D=3$.

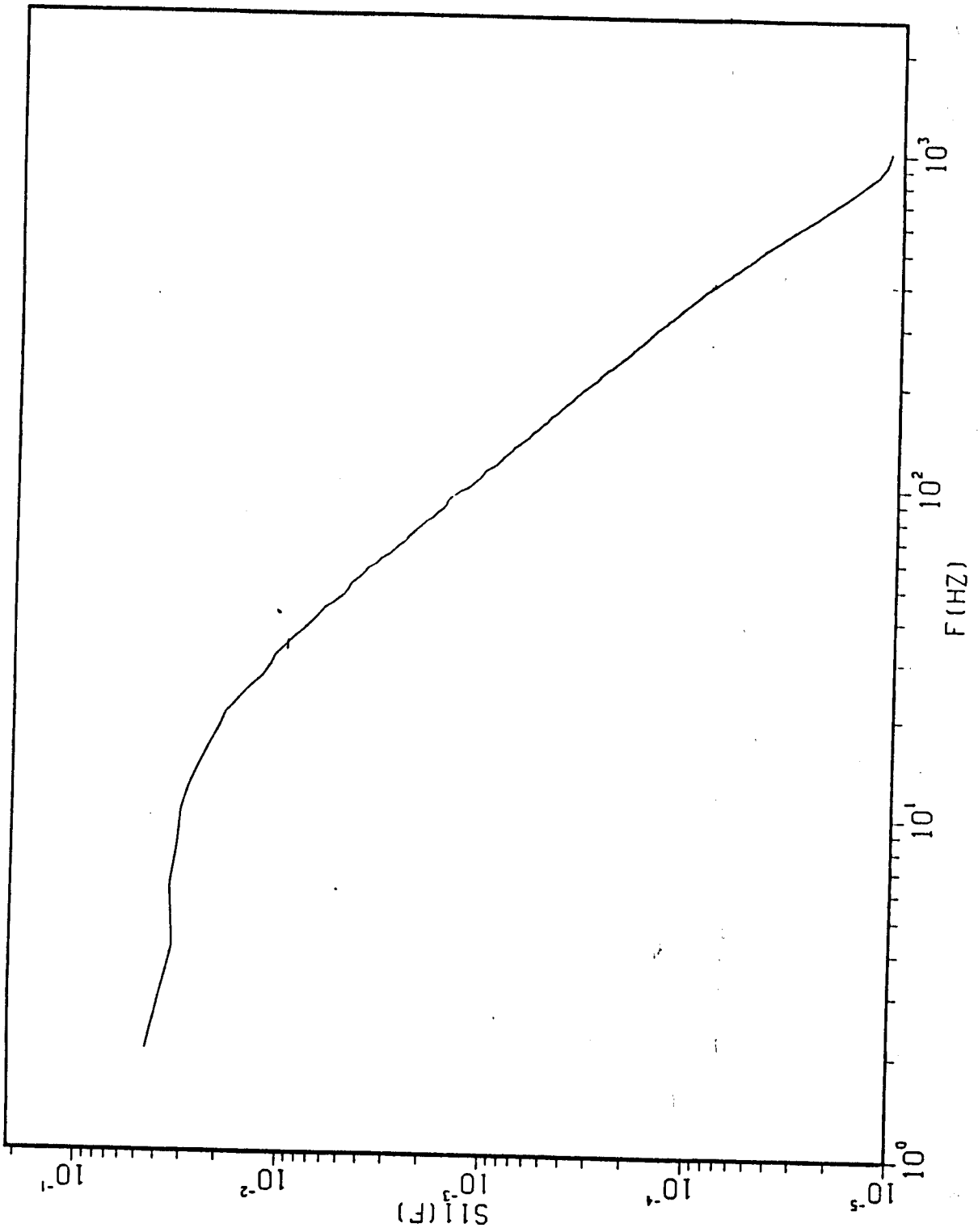


Figure 4.3.4(h) Streamwise velocity spectrum at $r/D=.90$, $x/D=3$.

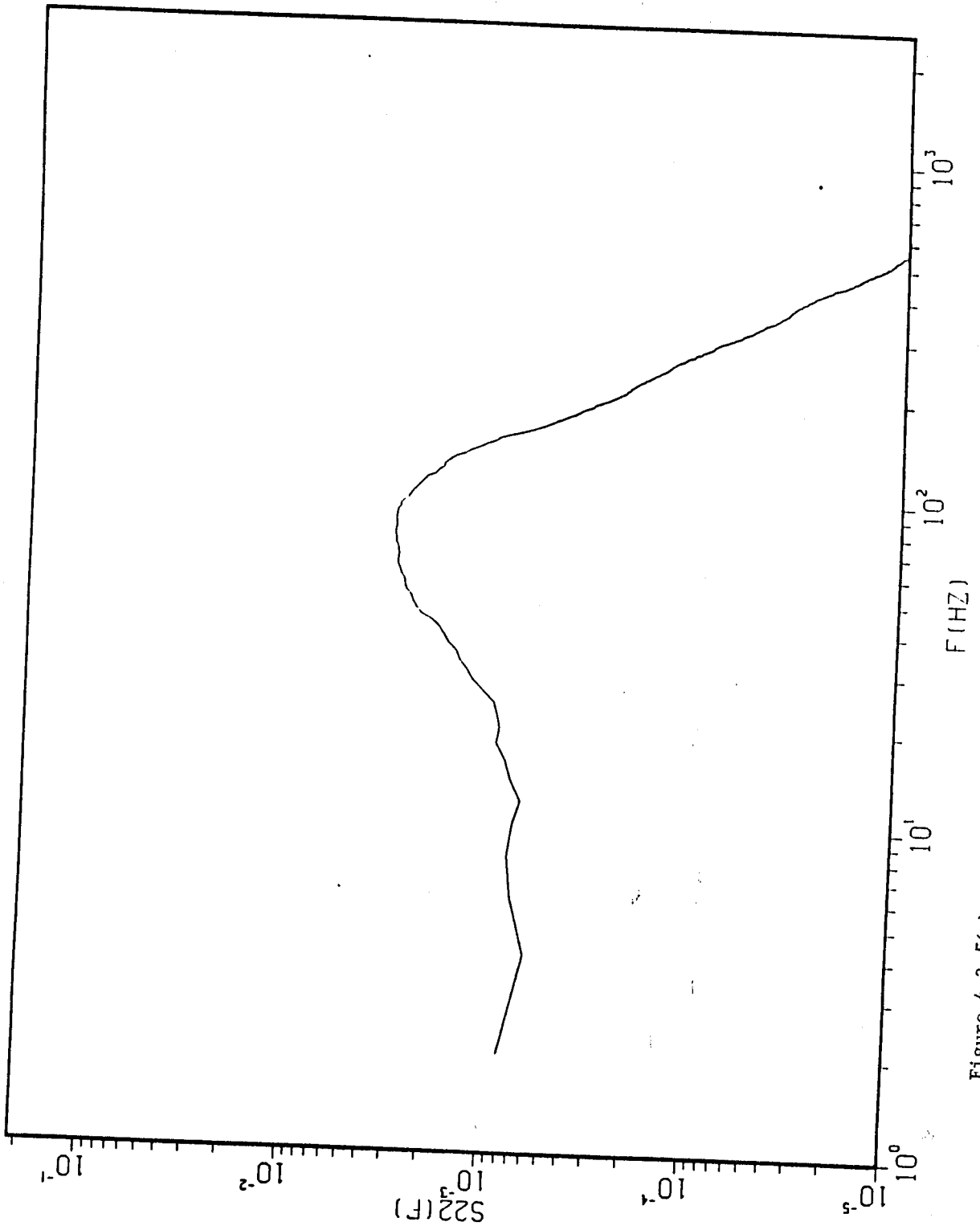


Figure 4.3.5(a) Radial velocity spectrum at $t = 10$

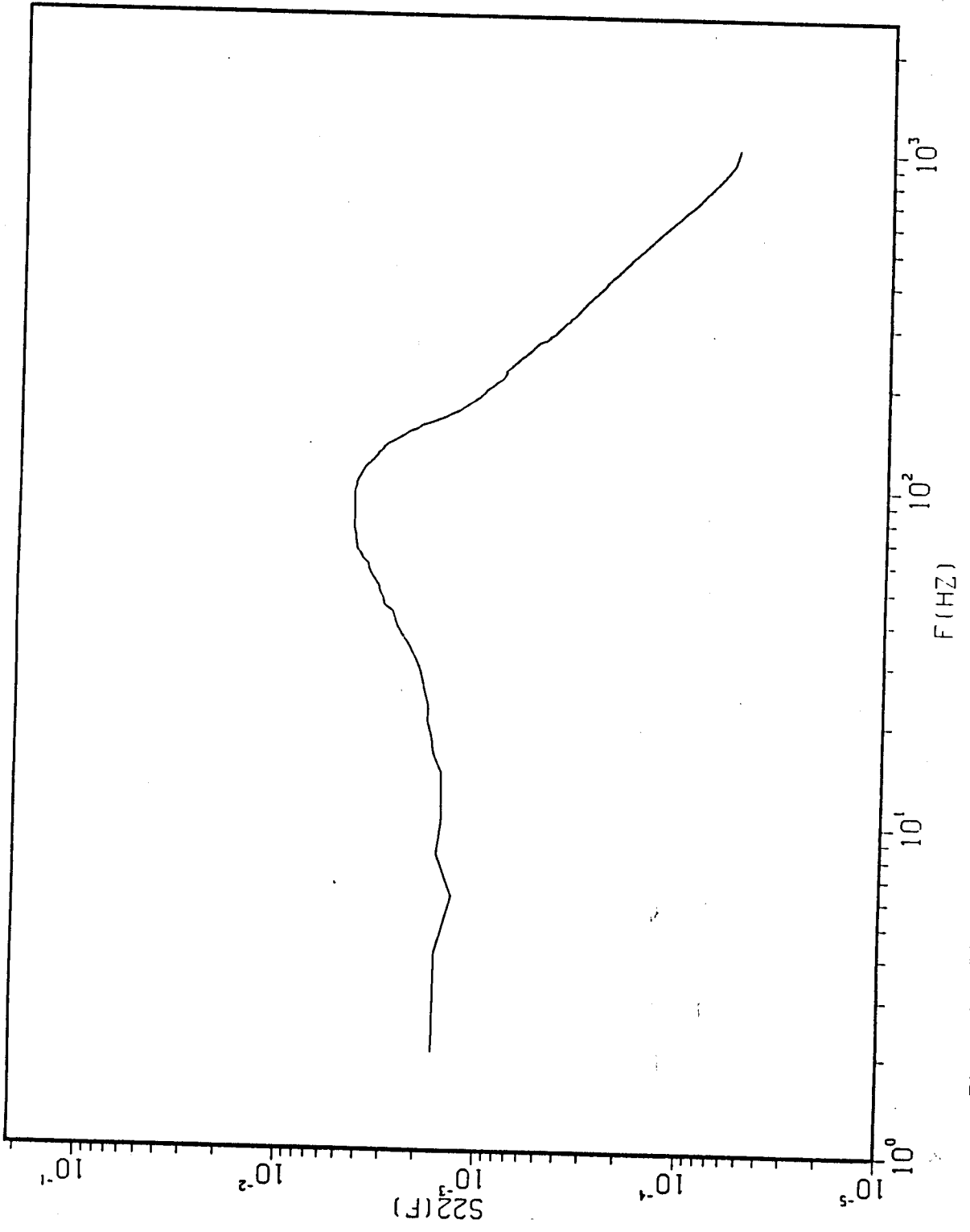


Figure 4.3.5(b) Radial velocity spectrum at $r/D=.24$, $x/D=3$.

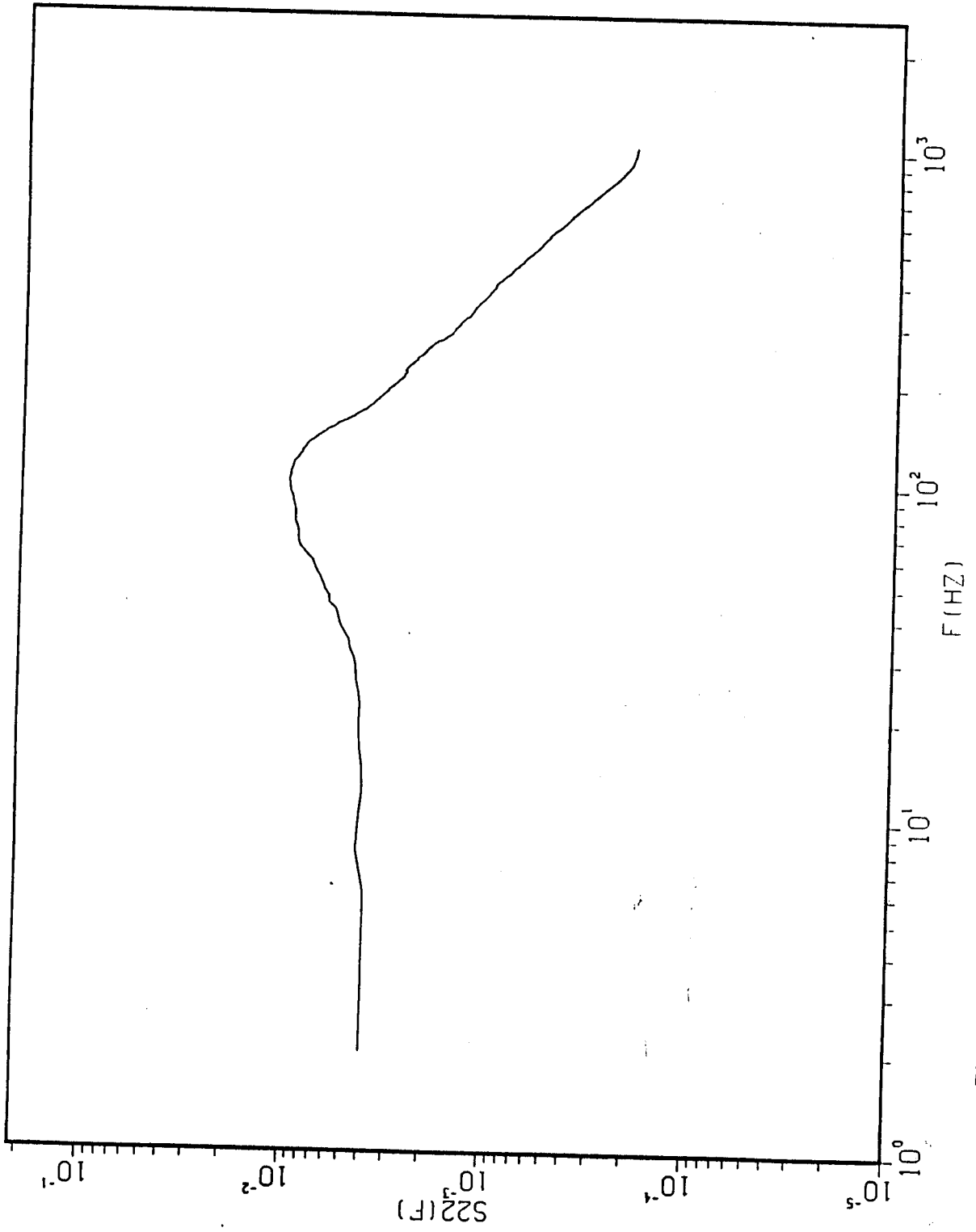


Figure 4.3.5(c) Radial velocity spectrum

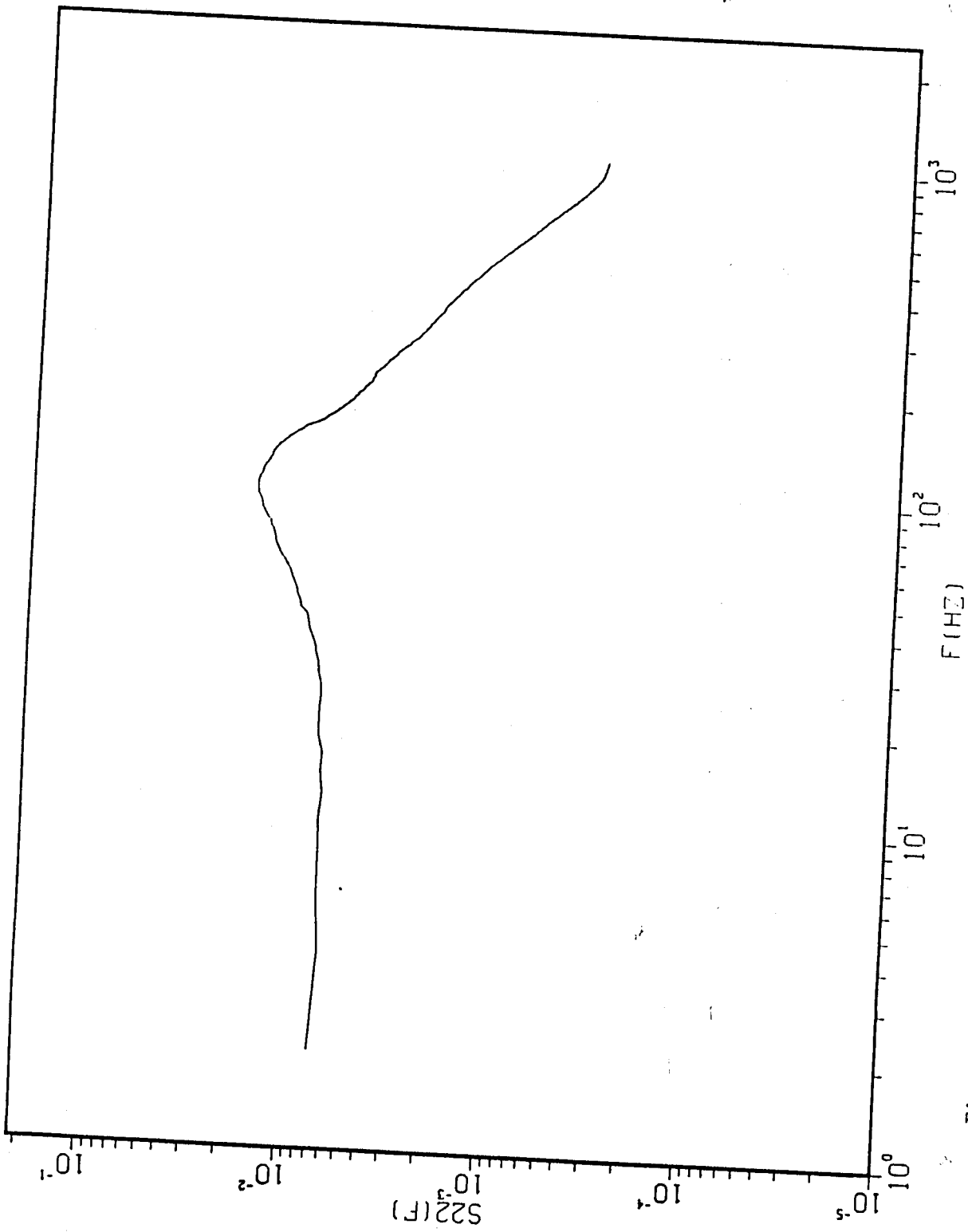


Figure 4.3.5(d) Radial velocity spectrum at $r/D=.46$, $x/D=3$.

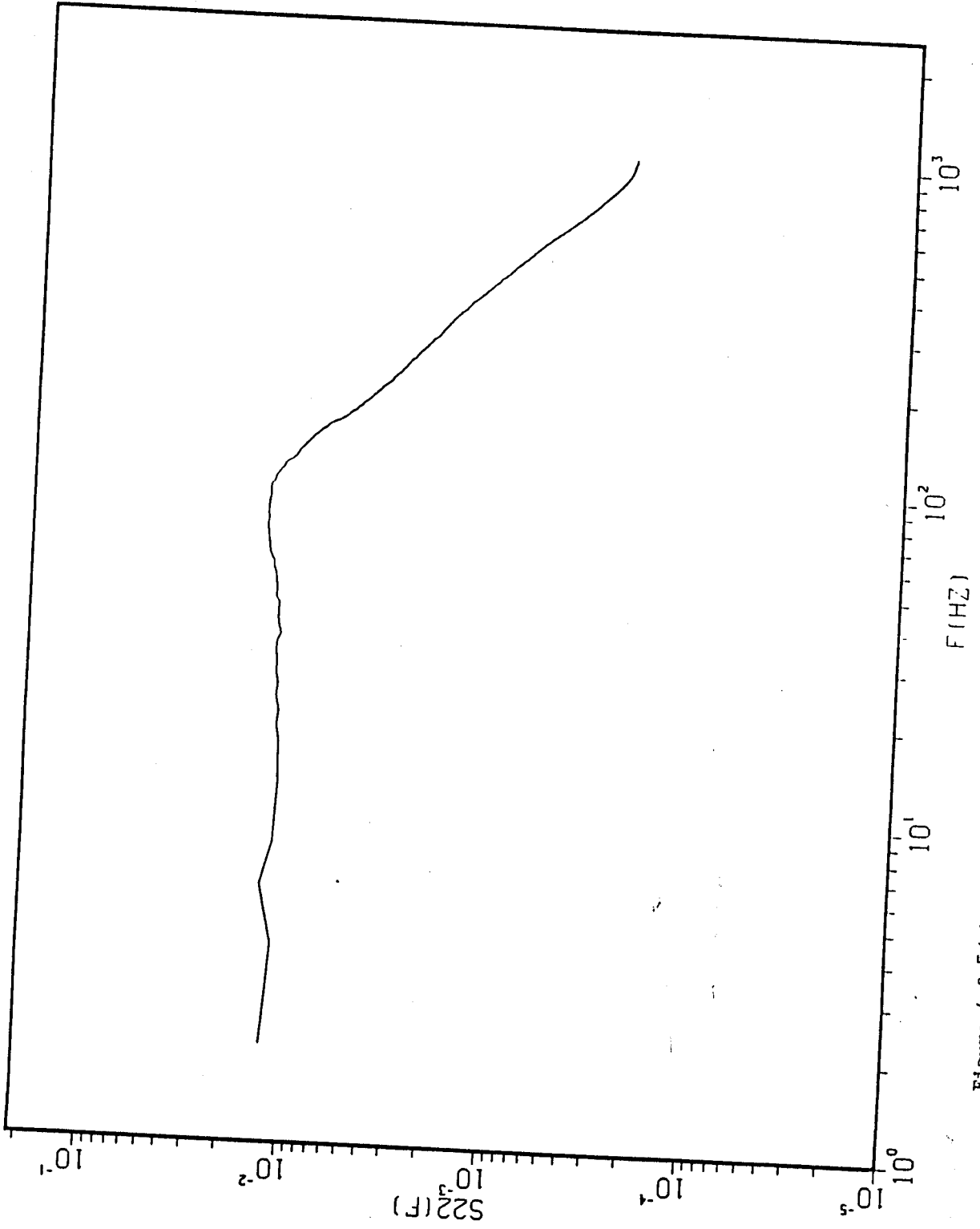


Figure 4.3.5(e) Radial velocity spectrum at $r/D=.57$, $x/D=3$.

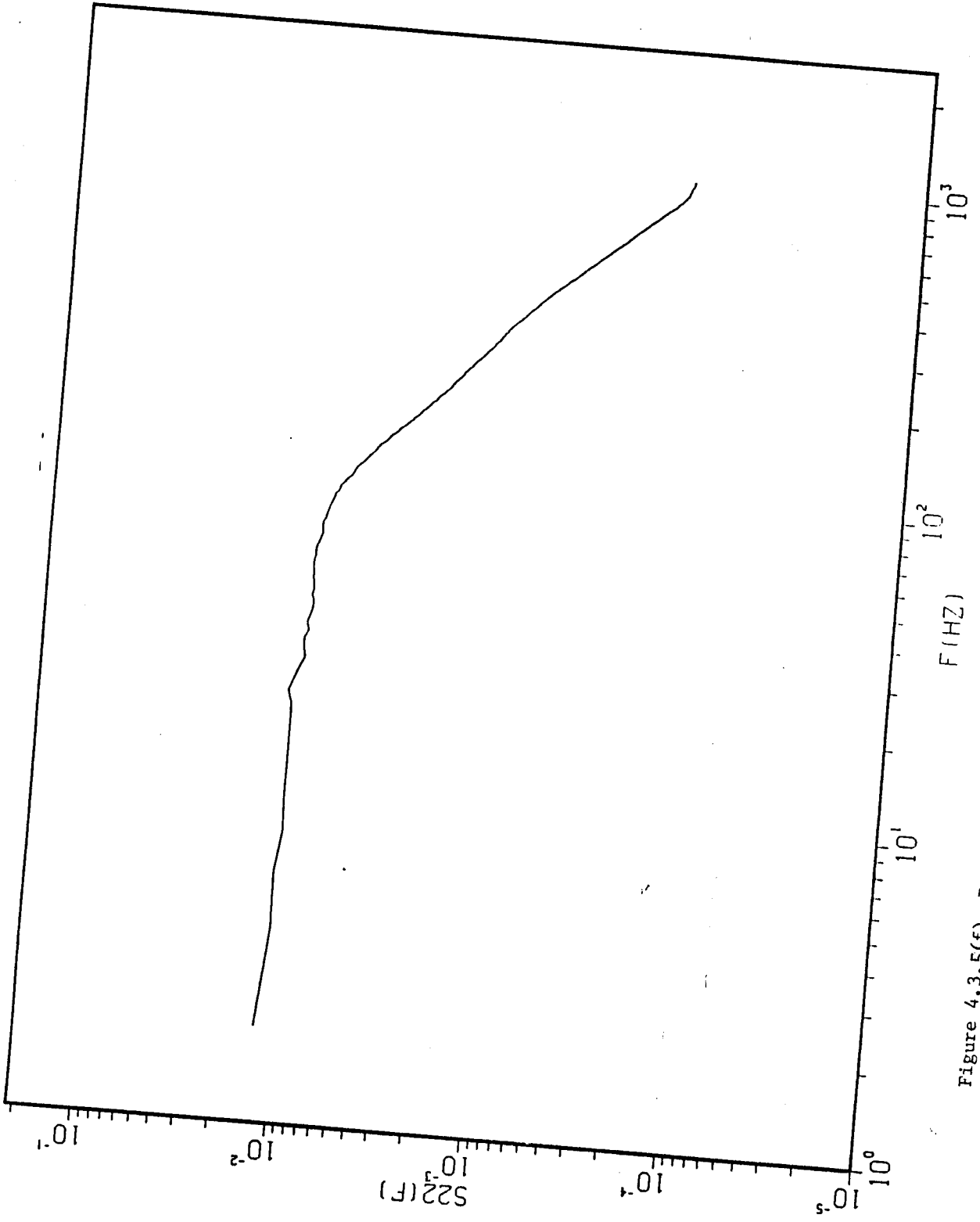


Figure 4.3.5(f) Radial velocity spectrum at $r/D=.68$, $x/D=3$.

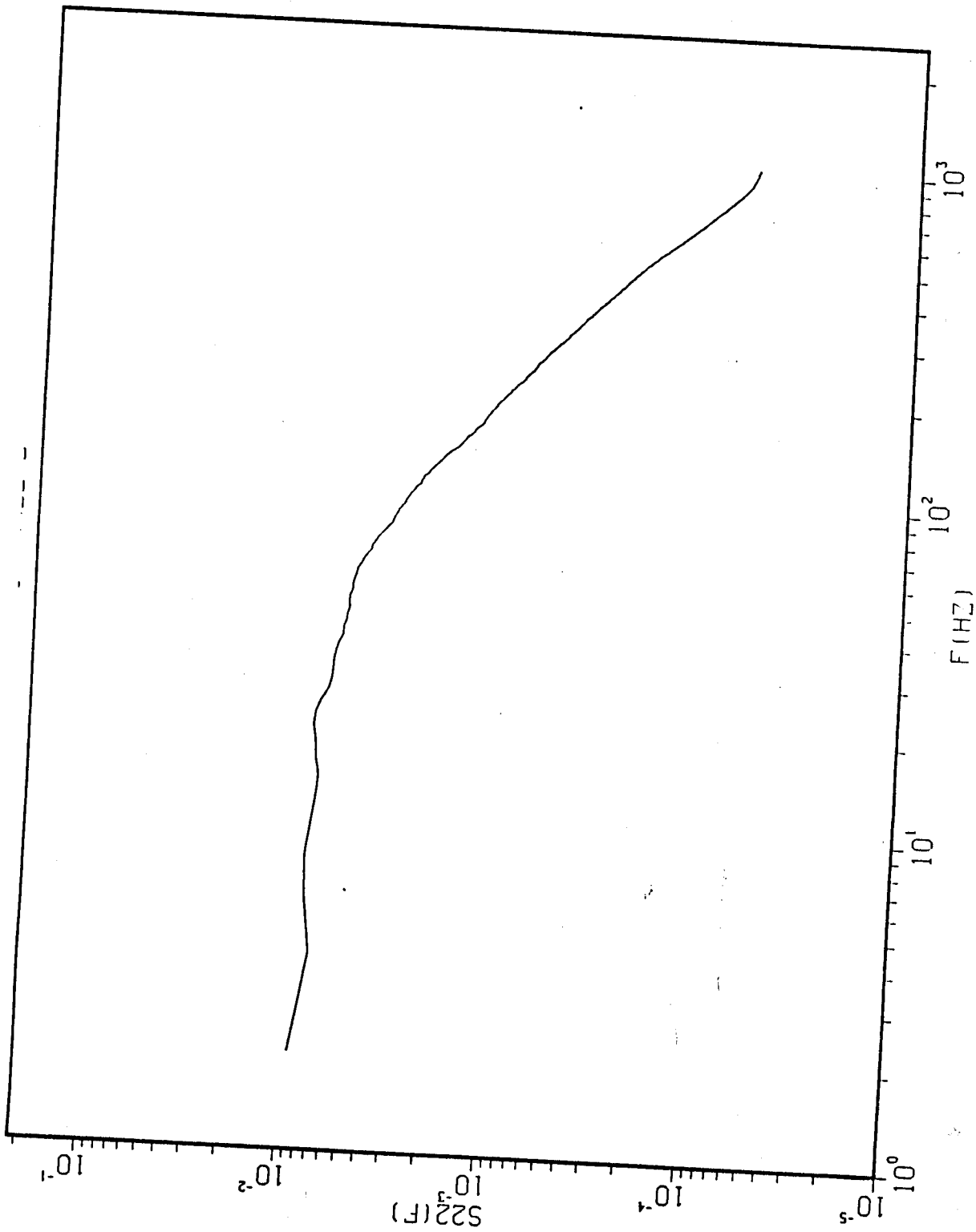


Figure 4.3.5(g) Radial velocity spectrum at $r/D=.79$, $x/D=3$.

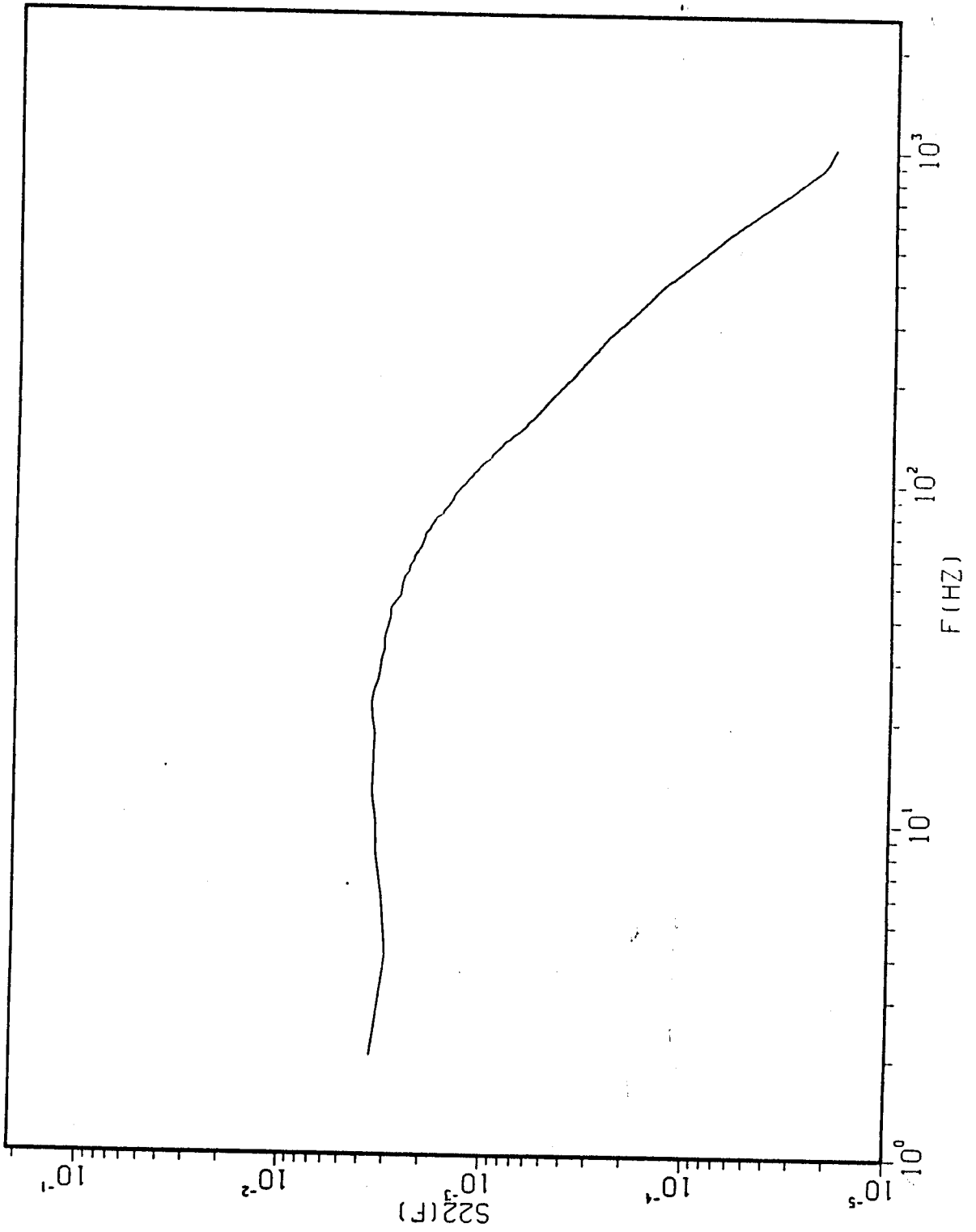


Figure 4.3.5(h) Radial velocity spectrum at $r/D = 0.5$, $v/D = 3$

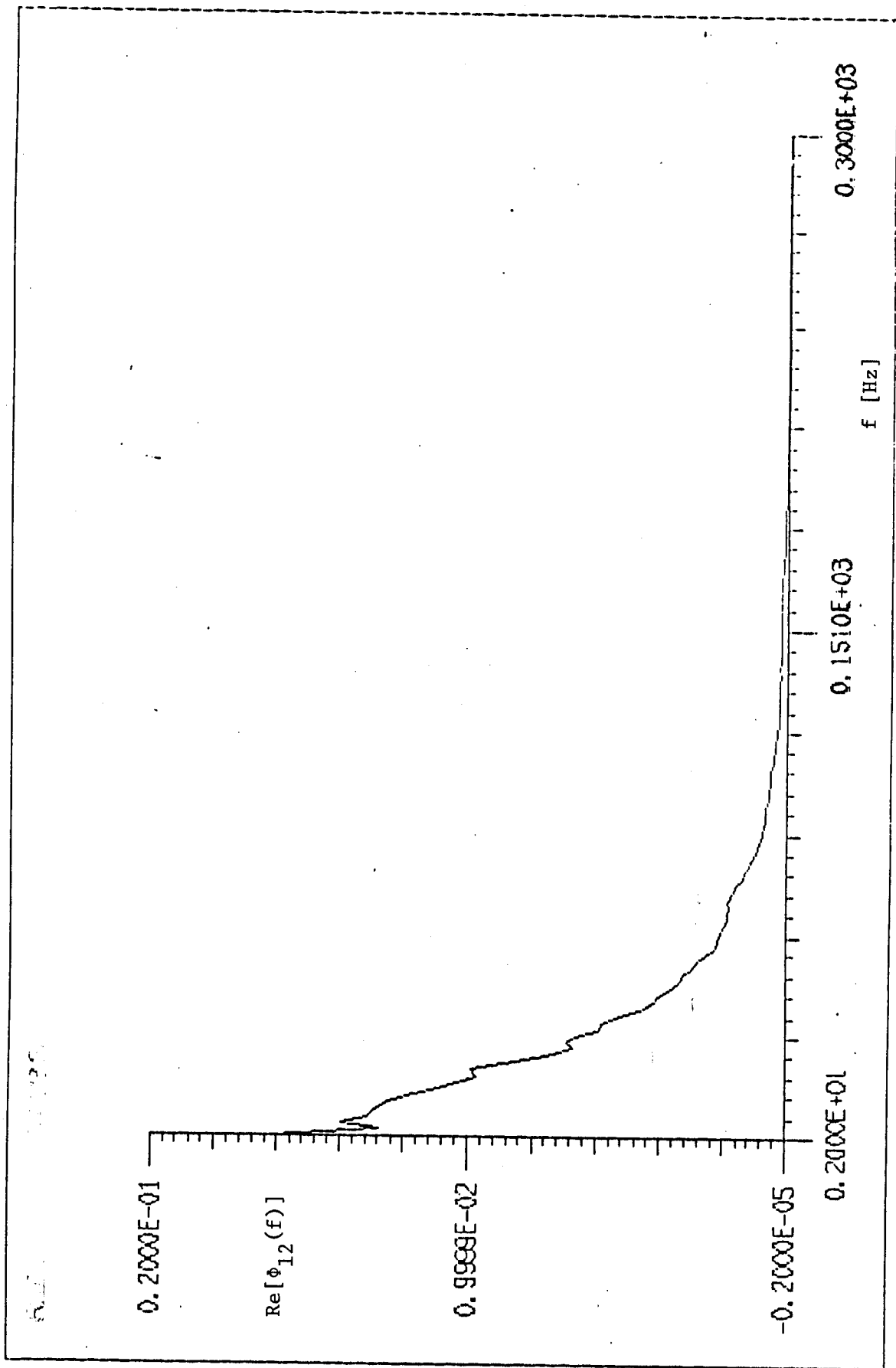


Figure 4.3.6(a) Co-spectrum between 2 radial locations ($r/D=.68$, $r/D=.79$) at $x/D=3$.

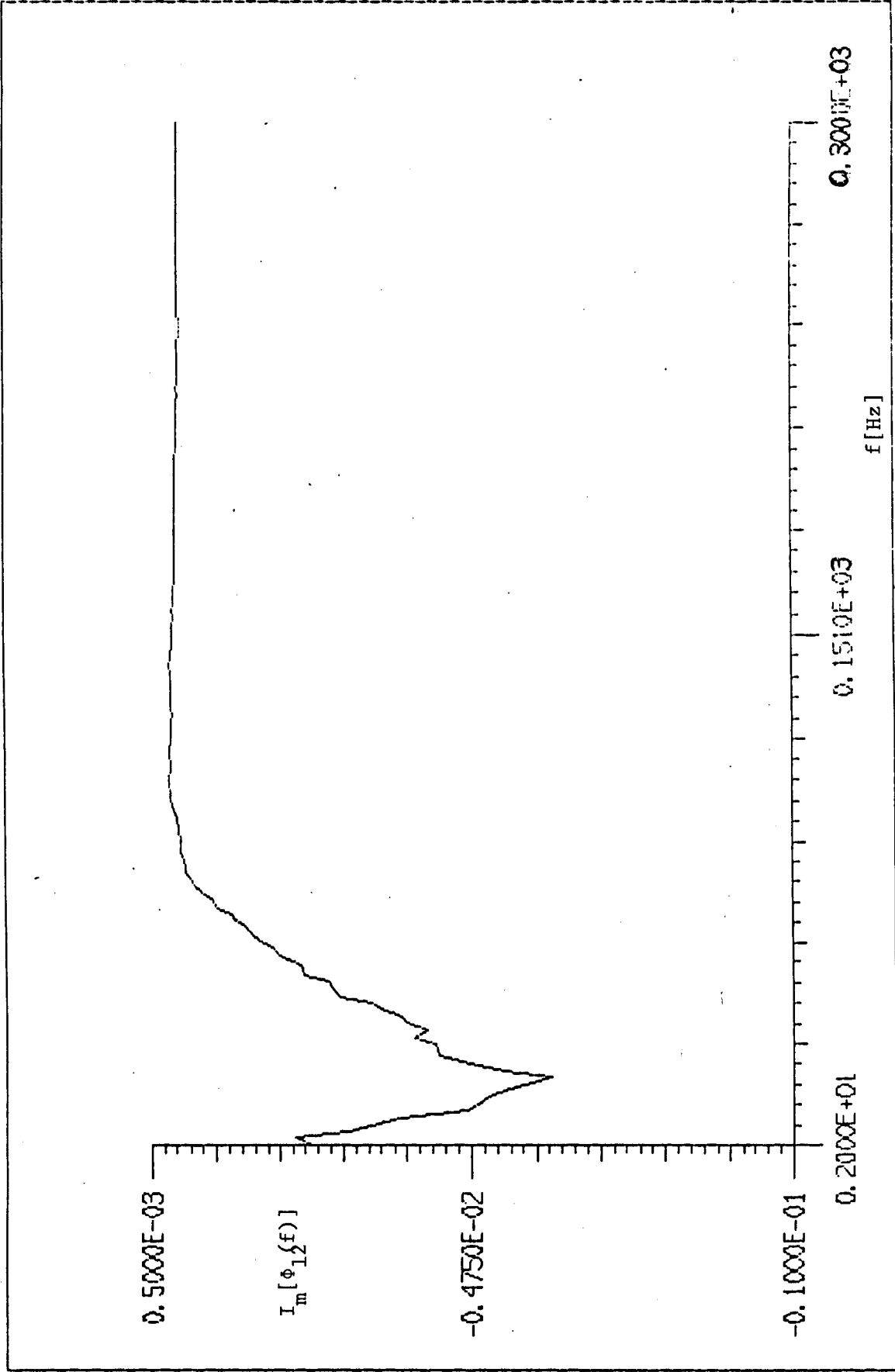


Figure 4.3.6(b) Quad-spectrum between 2 radial locations ($r/D=.68$, $r/D=.79$) at $x/D=3$.

CHAPTER 5

RESULTS AND DISCUSSION

5.1 Phase 1

A scalar, one-dimensional version of the orthogonal decomposition which utilizes the one-dimensional cross-spectra measured in the jet can be derived and formulated from equation (2.1.2) as

$$\int \phi_{11}(r, r', f) \psi_1^{(n)}(r', f) dr' = \lambda^{(n)}(f) \psi_1^{(n)}(r, f) \quad (5.1.1)$$

where r is the radius in the mixing layer. Using the measured values of the cross spectrum, equation (5.1.1) can be solved numerically for the eigenvalues and eigenfunctions.

The Fourier transform of the streamwise velocity can be reconstructed by

$$\hat{u}(r, f) = \sum_{n=1}^{\infty} a_n(f) \psi^{(n)}(f, r), \quad (5.1.2)$$

where

$$a_n(f) = \int \hat{u}(r, f) \psi^{(n)*}(r, f) dr. \quad (5.1.3)$$

The spectrum is reconstructed from

$$S(r, f) = \sum_{n=1}^{\infty} \lambda^{(n)}(f) |\psi^{(n)}(r, f)|^2, \quad (5.1.4)$$

where λ^n are the eigenspectra.

The Numerical Approximation

The numerical approximation to equation (5.1.1) consists basically of replacing the integral in (5.1.1) by a suitably chosen quadrature rule. Simpson's one-third rule was chosen as the

quadrature rule for its accuracy and simplicity. This can be written in general as

$$\sum_{i=1}^m W(r_i) \Phi(r_j, r_i, f) \Psi^{(n)}(r_i, f) = \lambda^{(n)}(f) \Psi^{(n)}(r_j, f),$$

$$j = 1, 2, \dots, m \quad (5.1.5)$$

where m is the maximum number of radial locations and $W(r_i)$ is a weighting function. In the present case $m = 7$. Equation (5.1.5) is now an algebraic eigenvalue problem.

Now the matrix formed from the values of Φ is complex Hermitian. That is

$$\Phi_{ij} = \Phi_{ji}^* \quad (5.1.6)$$

where the $*$ now means complex conjugate. However, the weighted matrix formed by $W(r_i) \Phi(r_j, r_i)$ no longer has this property. It is desirable, in the numerical solution of eigenvalue problems, to keep the coefficient matrix Hermitian (Baker 1977). Operating on both sides of equation (5.1.5) by $W(r_j)^{1/2}$ results in the following eigenvalue problem.

$$\sum_{i=1}^m [W^{1/2}(r_j) \Phi(r_j, r_i, f) W^{1/2}(r_i)] W^{1/2}(r_i) \Psi^{(n)}(r_i, f)$$

$$= \lambda^{(n)}(f) W^{1/2}(r_j) \Psi^{(n)}(r_j, f) \quad (5.1.7)$$

where now the matrix $W(r_j)^{1/2} \Phi(r_j, r_i, f) W(r_i)^{1/2}$ is Hermitian. Since this matrix is similar to that in equation (5.1.5) they have the same eigenvalues. The original eigenvectors can be recovered from those obtained from equation (5.1.6) by operating by $W(r_j)^{-1/2}$, i.e.

$$\psi^{(n)}(r_j, f) = W(r_j)^{-1/2} \psi^{(n)}(r_j, f) W(r_j)^{-1/2} \quad (5.1.8)$$

Results of the Orthogonal Decomposition Analysis for Phase 1

Figure 5.1.1 shows the eigenspectra for the three dominant modes. These eigenvalues represent the contribution to the total energy (integrated across the shear layer) from the various modes. It was found that the first mode contained about 40% of the total energy.

As was shown earlier (5.1.4), the power spectra at each radial position can be expanded in a series of the eigenmodes since each mode makes an independent contribution to the spectrum. Figure 5.1.2 shows the contributions from the first two modes to the power spectrum at a position on the low speed side of the mixing layer. It can be seen from this figure that the contribution to the power spectrum from the first mode peaks at very low frequency, while that of the second peaks at a higher frequency. This was found to be the case at the other radial positions around the center of the mixing layer. In this sense then, we see that the dominant mode is indeed representative of the larger scales in the flow.

Figure 5.1.3 [using equation (5.1.4) for $n = 1, 2, 3$] shows the convergence of the expansion for this power spectrum. Similar results were obtained at the other locations. These results show that nearly all the energy is contained in the first three modes.

From the spectral data it might be expected that the instantaneous velocity signal could be represented adequately with these three modes. After application of equation (5.1.2), this is indeed seen to be the case (see Figures 5.1.4-5.1.7). Figure 5.1.4 is a record of the original velocity signal in the center of the mixing

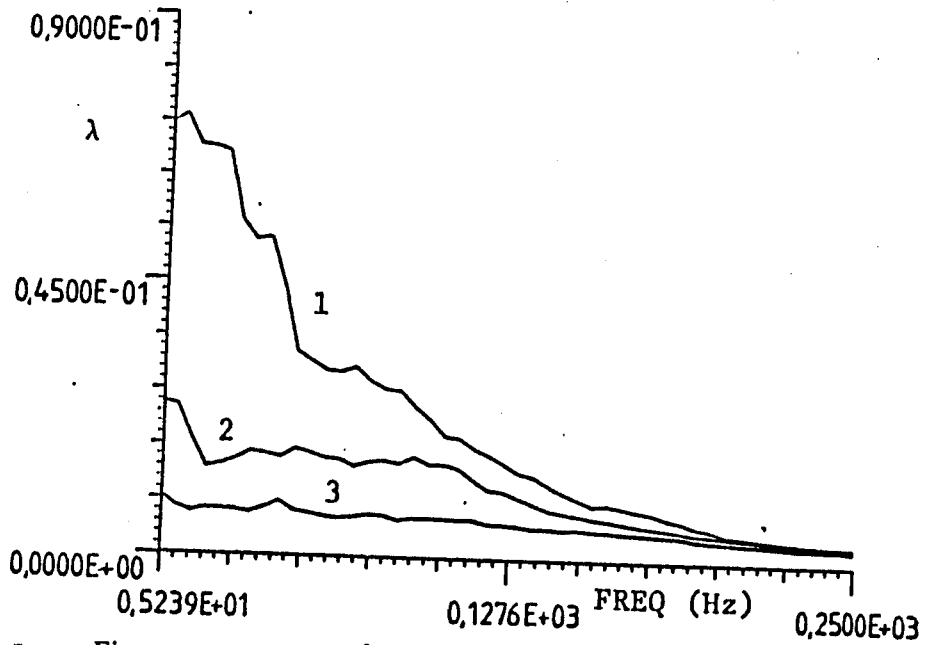


Fig 5.1.1 Eigenspectra showing how energy is distributed among the first three eigenvalues

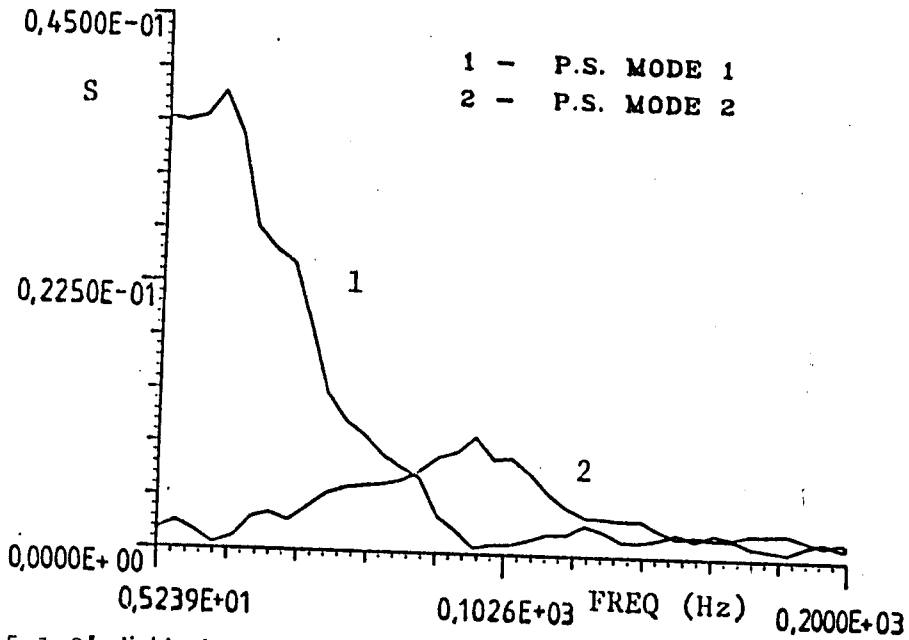


Fig 5.1.2 Individual contributions to the power spectrum from first 2 modes

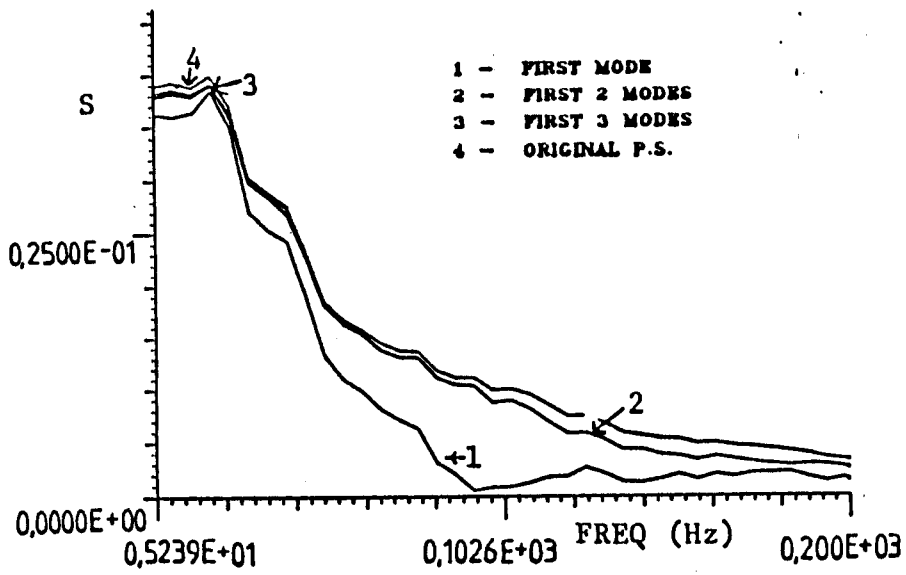


Fig 5.1.3 Convergence of power spectrum

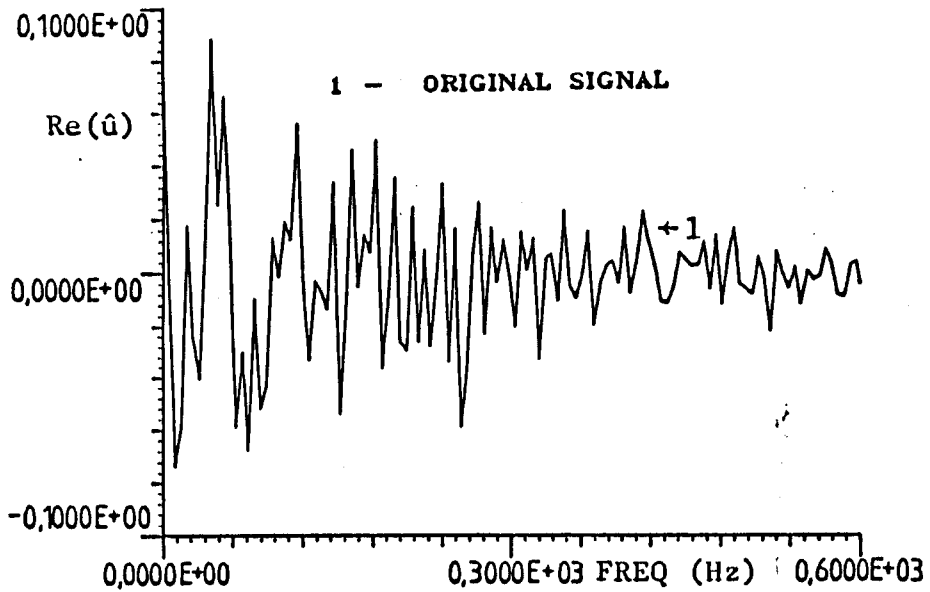


Fig 5.1.4 Real part of F.T. of original signal

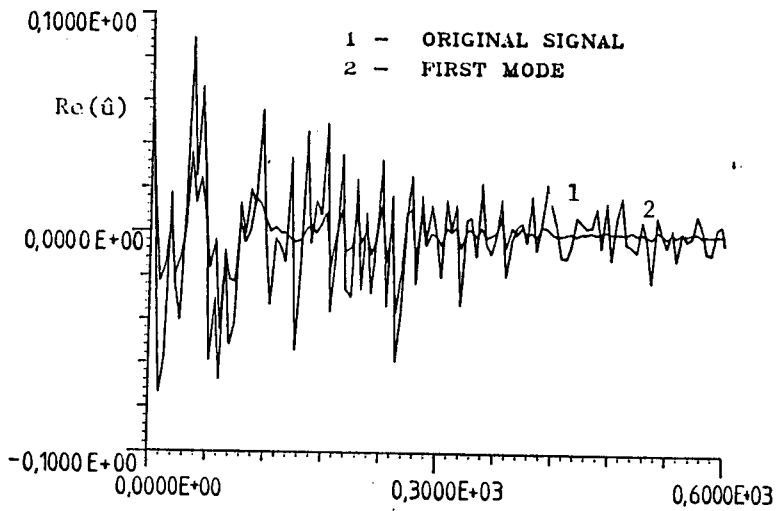


Fig 5.1.5 First mode superimposed on original

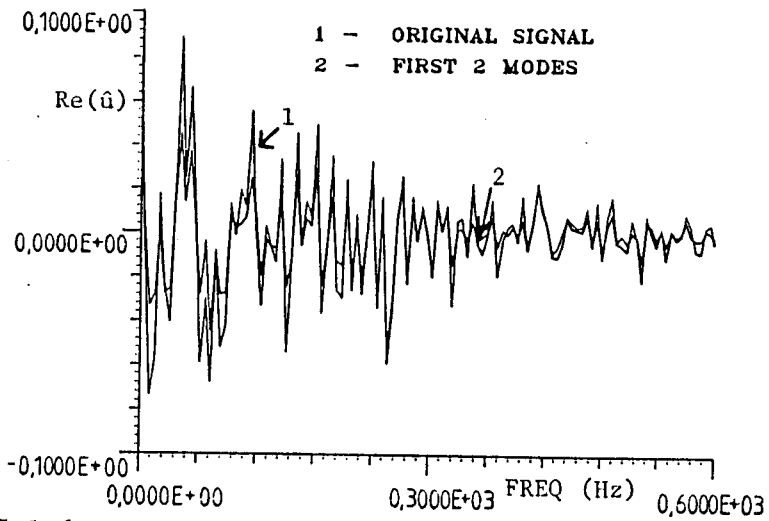


Fig 5.1.6 First 2 modes superimposed on original

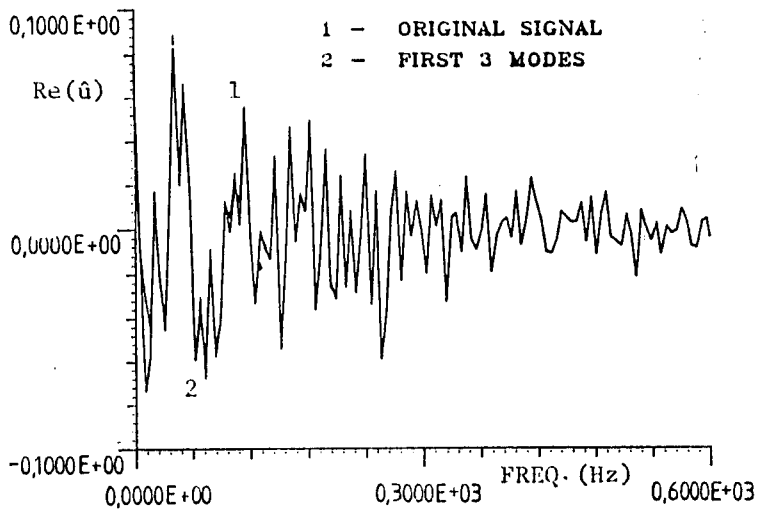


Fig 5.1.7 First 3 modes superimposed on original. Note: Essentially no difference

layer (real part of its Fourier transform). Figure 5.1.5 shows the super-position of the 1st mode ($n = 1$ in equation (5.1.2)) on the original signal. Figure 5.1.6 shows the first 2 modes. Figure 5.1.7 shows the first 3 modes. As can be seen from Fig. 5.1.7, almost the entire signal has been reconstructed from the summation of the first 3 modes.

From these results the orthogonal decomposition has been shown to be remarkably efficient at organizing data and the instantaneous properties of the random signal have not been lost, only organized. So efficient has the scheme been at organizing the energy that only a few terms were needed to completely represent the instantaneous signal.

5.2 Phase 2

The results from Phase 1 discussed in Section 5.1 were encouraging. However, because only 7 probes were used to span the mixing layer it was felt that a grid spacing problem may exist. In particular, if more probes were used across the same span would three terms still be adequate to represent the spectra and instantaneous signal as was seen in Phase 1?

This problem was addressed by performing the same experiment over again, only now 13 probes were used across the span where 7 had been used previously. This effectively halved the grid spacing. The eigenvalue problem solved was the same as in Phase 1 only now $m=13$ in equation (5.1.5).

The simplest way to compare the results from Phase 1 and 2 is to operate on equation (5.1.4) by summing over frequency. Equation (5.1.4) becomes as follows

$$\int_{\mathbb{F}} S(r, f) = \int_{\mathbb{F}} \sum_{n=1}^m \lambda^{(n)}(f) |U^{(n)}(r, f)|^2 \quad (5.2.1)$$

where the left hand side of (5.2.4) is $u^{\overline{r^2}}$ by Parseval's identity. This approach will allow the convergence of $\overline{u^2}$ for the two problems to be compared.

Figure 5.2.1a shows a plot of the LHS equation (5.2.1) with the contribution of one term from the RHS superimposed on it for the 7 wire case. Figure 5.2.1b shows a plot of the same only now using the 13 wire data. As can be seen by examination of Figure 5.2.1, the contribution from the first term for the 7 wire case is about 5% more than that for the 13 wire case.. Remember that the first term in the expansion is presumed to be the large eddy so that these plots show the contribution from the large eddy to the turbulent energy. This small difference (5%) in the energy content of the large eddy (the 7 wire result being higher) between the 7 and 13 wire cases indicates that 7 wires across the span is adequate. The instantaneous velocities also converged with 3 terms for the 13 wire case in much the same manner as the 7 wire case.

The number of grid points needed across a given span of finite energy is obviously flow dependent. Lumley (1970) showed that the number of terms in the expansion needed to adequately represent the instantaneous signals or spectra is given by $N \leq L/\mathcal{L}$ where \mathcal{L} is an intensity-weighted average integral scale and L is the span that covers the variation of the energy distribution. In the jet mixing layer $N \simeq 3$.

The fact that 7 wires appear adequate in the jet shear layer would suggest that there is a spatial sampling theorem (unproven at

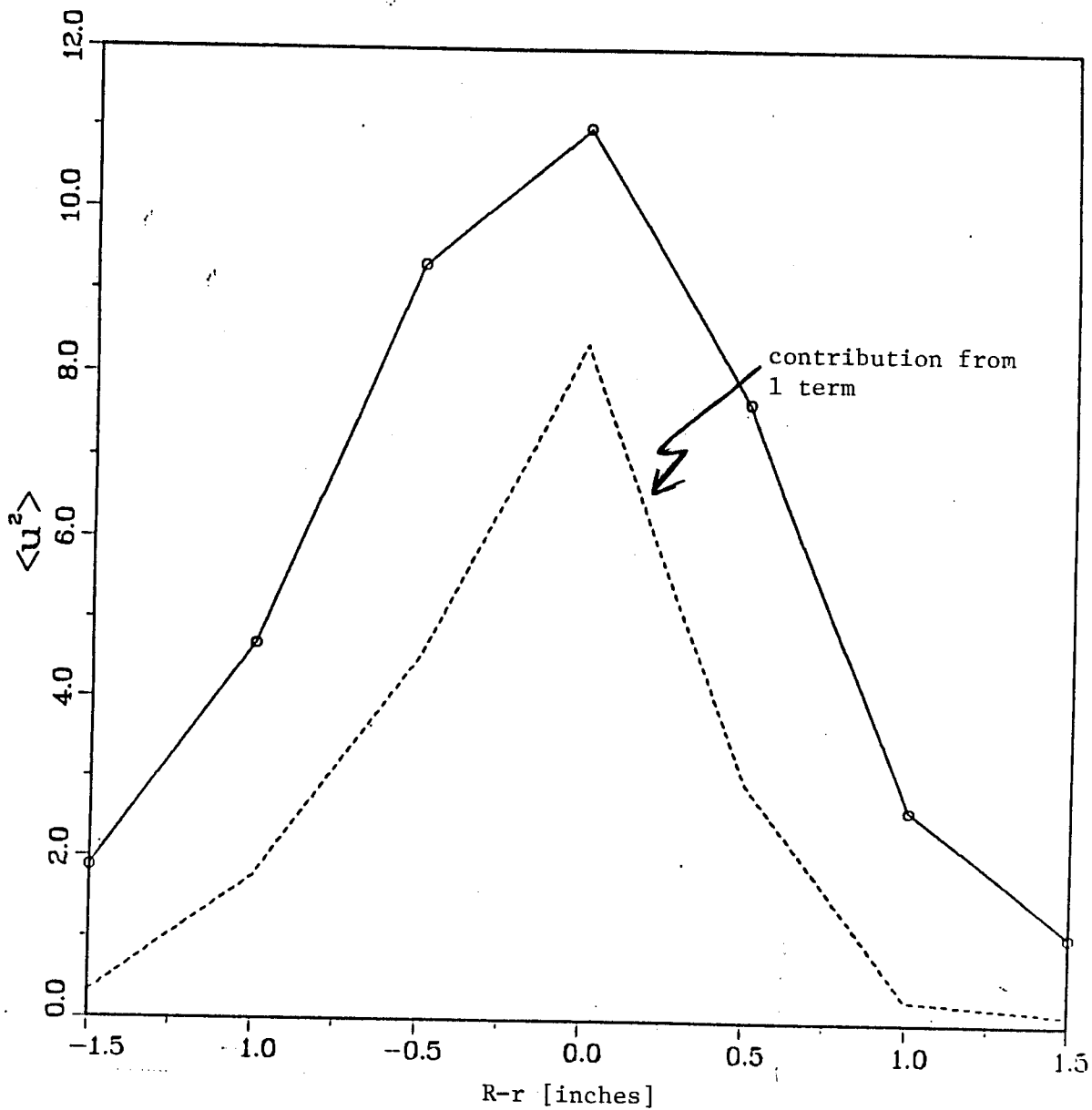


Figure 5.2.1 (a). $\overline{u^2}$ as a function of radius in the jet mixing layer for the 7-wire case with the contribution from first eigenfunction superimposed on it.

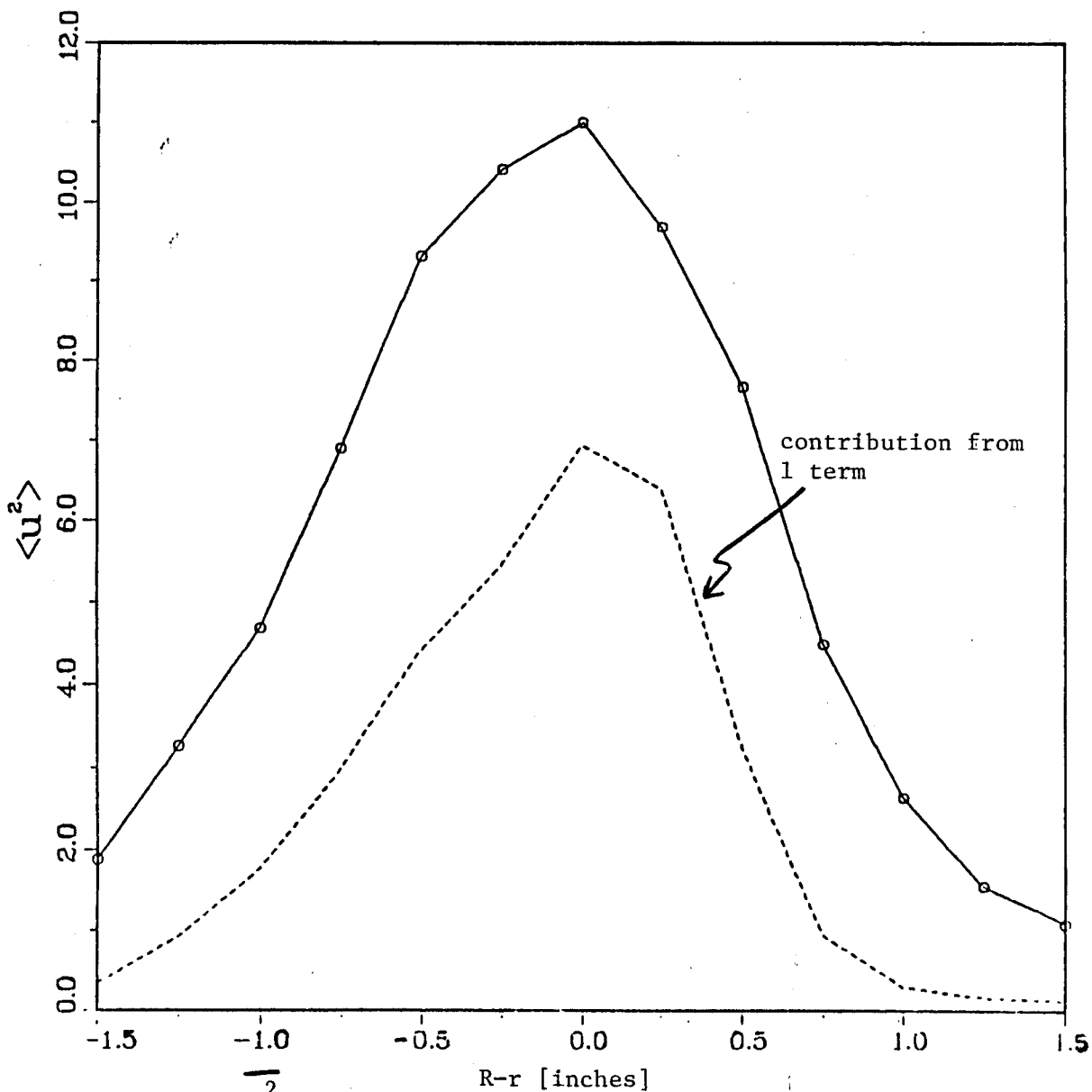


Figure 5.2.1(b). $\overline{u^2}$ as a function of radius in the jet mixing layer for the 13-wire case with the contribution from the first eigenfunction superimposed on it.

this point) to be concerned with, that is, if 3 terms are needed to represent the signal then at least $2N+1$ grid points should be used. This suggests that in this particular flow situation, 7 grid points across the span is the minimum needed (v. Adrian (1985)).

5.3 Azimuthal Problem Streamwise Velocity Only - Phase 3

This phase involves adding the azimuthal variation to Phase 1 where the decomposition was utilized for the radial direction, and the Fourier modes were used for the azimuthal direction and time.

A scalar version of the orthogonal decomposition which utilizes the streamwise velocity measurements from the jet can be derived and formulated as,

$$\int A_{11}(r, r', f, m) \Psi^{(n)}(r', f, m) dr' = \lambda^{(n)}(f, m) \Psi^{(n)}(r, f, m) \quad (5.3.1)$$

where r is the radius in the jet mixing layer and the A_{11} 's are the complex coefficients defined by equations (2.2.3) and (2.2.4) with $i=j=1$ because only the streamwise velocities were measured in this phase. Using the measured values of A_{11} equation (5.3.1) can be solved numerically for the eigenvalues and eigenfunctions.

5.3.1 Results of the Azimuthal Decomposition Analysis - Phase 3

Before examining the results of (5.3.1), the breakdown into azimuthal modes warrants examination. From (2.2.3) and (2.2.4) setting $i=j=1$, (since only streamwise velocities were measured in phase 3) they become respectively,

$$A_{11}(r, r', f, 0) = \frac{1}{\pi} \int_0^{\pi} \mathcal{F}_{11}(r, r', f, \theta) d\theta \quad (5.3.2)$$

and

$$A_{11}(r, r', f, m) = \frac{2}{\pi} \int_0^{\pi} \bar{\Phi}_{11}(r, r', f, \theta) \cos m\theta d\theta, \quad (5.3.3)$$

The numerical approximation to equation (5.3.3) is as follows:

$$A_{11}(r, r', f, m) = \frac{2}{\pi} \sum_{n=1}^{M/2+1} \bar{\Phi}_{11}(r, r', f, n) \cos m((n-1)\Delta\theta) \Delta\theta \quad (5.3.4)$$

where

$$\Delta\theta = \frac{2\pi}{M} \quad (5.3.5)$$

Substituting equation (5.3.5) into (5.3.4) and mapping M to $2N$ results in

$$A_{11}(r, r', f, m) = \frac{2}{N} \sum_{n=1}^{N+1} \bar{\Phi}_{11}(r, r', f, n) \cos \frac{m(n-1)\pi}{N} \quad (5.3.6)$$

where N is the number of grid points not counting the symmetry point.

It is advantageous to solve this equation numerically utilizing a FFT algorithm. The FFT does not do exactly what is needed here so it must be modified in order to achieve the desired result (Moin, private communication). The FFT does the following,

$$A_{11}(r, r', f, m) = \sum_{n=1}^M \bar{\Phi}_{11}(r, r', f, n) \exp\left[\frac{i2\pi m(n-1)}{M} \right] \quad (5.3.7)$$

which can be written as

$$A_{11}(r, r', f, m) = \sum_{n=1}^M \bar{\Phi}_{11} \cos \frac{2\pi m(n-1)}{M} + i \sum_{n=1}^M \bar{\Phi}_{11} \sin \frac{2\pi m(n-1)}{M} \quad (5.3.8)$$

In order to use the FFT, equation (5.3.8) must look like (5.3.6).

This can be achieved by letting $M=2N$ and setting

$$\bar{\Phi}_{11}(r, r', f, n) = 0 \text{ for } n = N+2, \dots, 2N$$

and realizing that the imaginary part of equation (5.3.8) is zero because of the symmetry properties of $\overline{\Phi}_{11}$. For phase 3, $N=15$ so that a 30 point transform was done for each r, r' and frequency combination.

If both sides of (5.3.2) and (5.3.3) are summed over f they become respectively

$$B_{11}(r, r', 0) = \frac{1}{\pi} \int_0^{\pi} R_{11}(r, r', \theta) d\theta \quad (5.3.9)$$

and

$$B_{11}(r, r', m) = \frac{2}{\pi} \int_0^{\pi} R_{11}(r, r', \theta) \cos m\theta d\theta \quad (5.3.10)$$

where

$$R_{11}(r, r', \theta) = \sum_f \overline{\Phi}_{11}(r, r', \theta, f) = \overline{u(r, \theta_0) u(r', \theta_0 + \Delta\theta)} \quad (5.3.11)$$

and

$$B_{11}(r, r', m) = \sum_f A_{11}(r, r', m, f). \quad (5.3.12)$$

$R_{11}(r, r', \theta)$ can be reconstructed from the $B_{11}(r, r', m)$ as,

$$R_{11}(r, r', \theta) = \sum_{m=0}^{N-1} B_{11}(r, r', m) \cos m\theta. \quad (5.3.13)$$

It is advantageous to set $r = r'$, so that B_{11} and R_{11} can be plotted for each radial position in the jet mixing layer. A sampling of these is plotted in Figures 5.3.1-5.3.4.

Figure 5.3.1a shows measurements of $R_{11}(\theta)$ at a position near the potential core at $r/D = 0.13$. There is clearly a strong correlation over the entire 180° span. The corresponding $B_{11}(m)$ is plotted in

Fig. 5.3.1(b). The 0th mode (axisymmetric mode) can be seen to contain most of the energy indicating a strong ring-like coherent structure at this position.

Figure 5.3.2a shows measurements of $R_{11}(\theta)$ at a position on the high-speed side of the mixing layer at $r/D = .26$. Again there is a strong correlation over the entire 180° span. The corresponding $B_{11}(m)$ is plotted in Figure 5.3.2b. The first few modes again contain most of the energy indicating that there is still a ring-like structure at this position.

Figure 5.3.3a shows measurements of $R_{11}(\theta)$ at a position on the high speed side of the mixing layer at $r/D = .39$. The correlation falls off very rapidly indicating a breakdown of the ring-like structure at this position. This can be seen by examining $B_{11}(m)$ in Figure 5.3.3b. The energy is now spread out over many of the modes when compared to Figures 5.3.1b and 5.3.2b.

Figure 5.3.4a shows measurements of $R_{11}(\theta)$ at a position in the center of the mixing layer at $r/D = 0.52$. Again the correlation falls off very rapidly. The corresponding $B_{11}(m)$ is plotted in Figure 5.3.4b. An interesting phenomenon occurs at this position. Instead of the first few modes dominating, as in the aforementioned cases, there is a shift here to the fourth, fifth and sixth modes.

The other three positions in the mixing layer, $r/D = 0.65$, $r/D = 0.78$, and $r/D = 0.91$ where measurements were taken are not shown because R_{11} and B_{11} at these positions exhibit the same basic characteristics as those in Figures 5.3.4a and 5.3.4b.

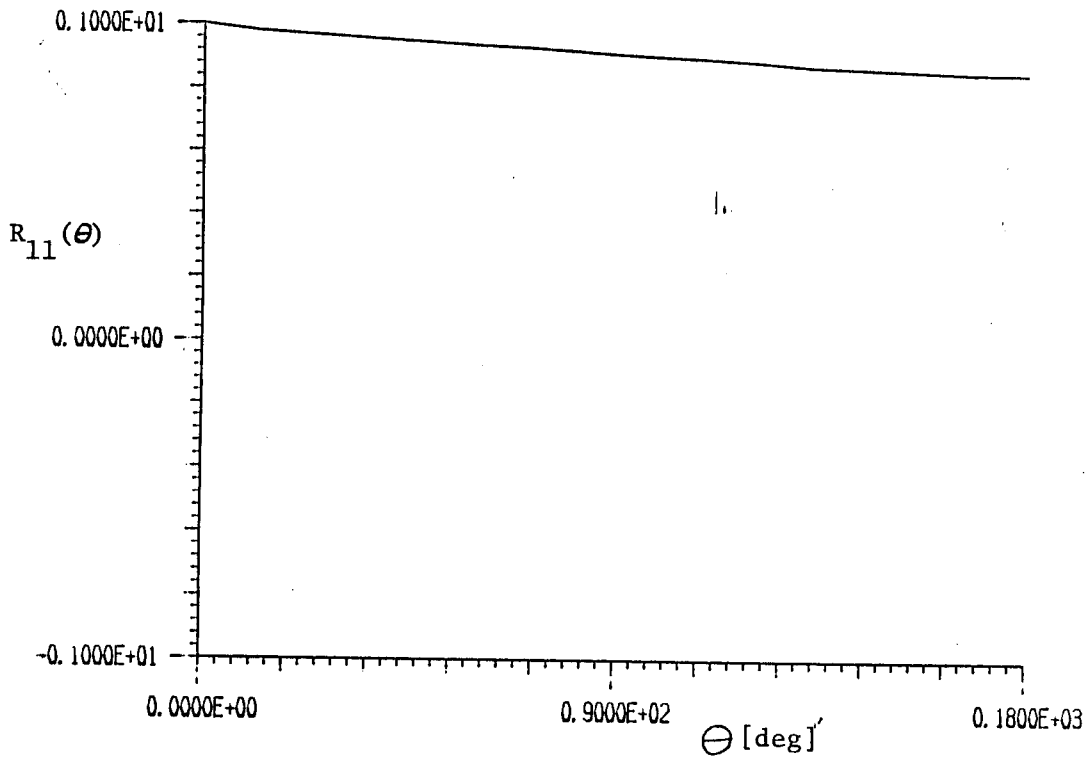


Figure 5.3.1(a). $R_{11}(\theta)$ at $x/D=3, r/D=0.13$

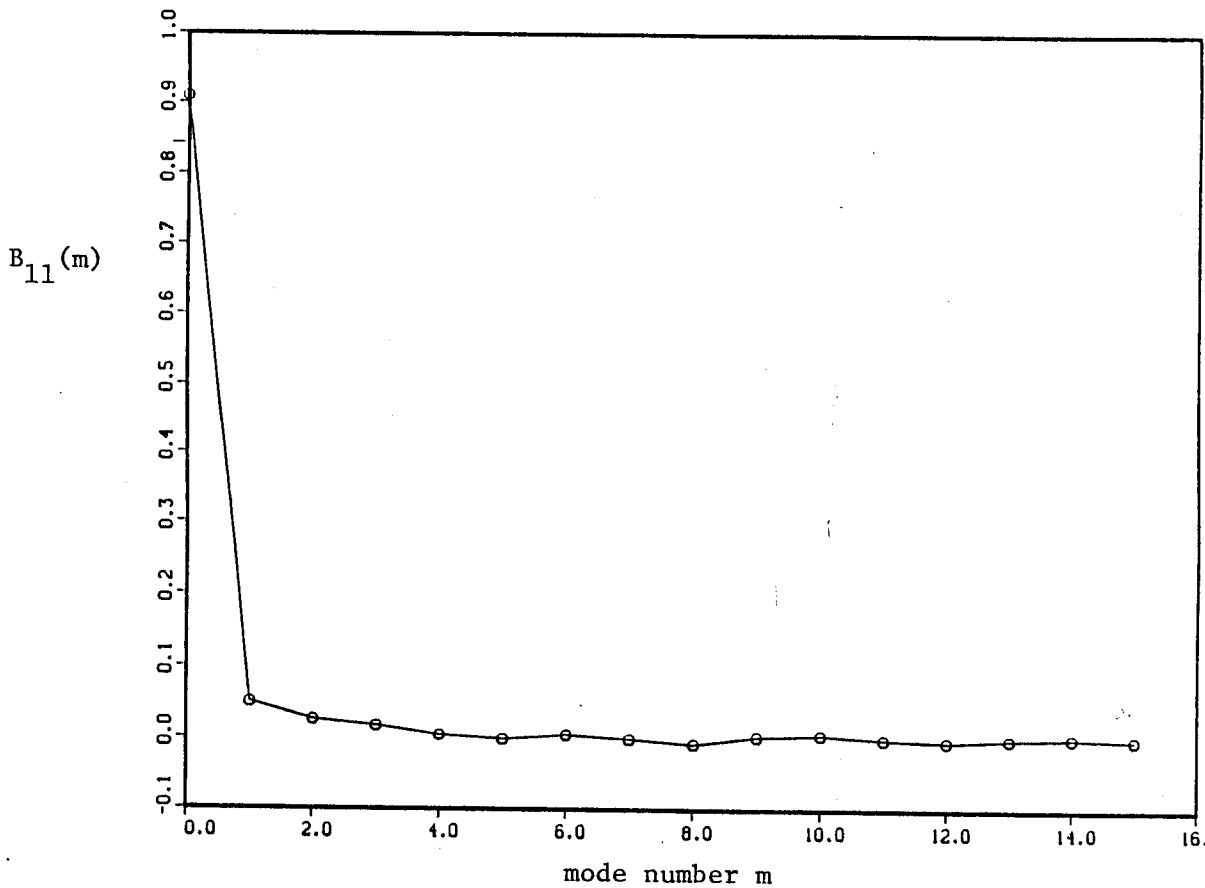


Figure 5.3.1(b) $B_{11}(m)$ at $x/D=3, r/D=0.13$

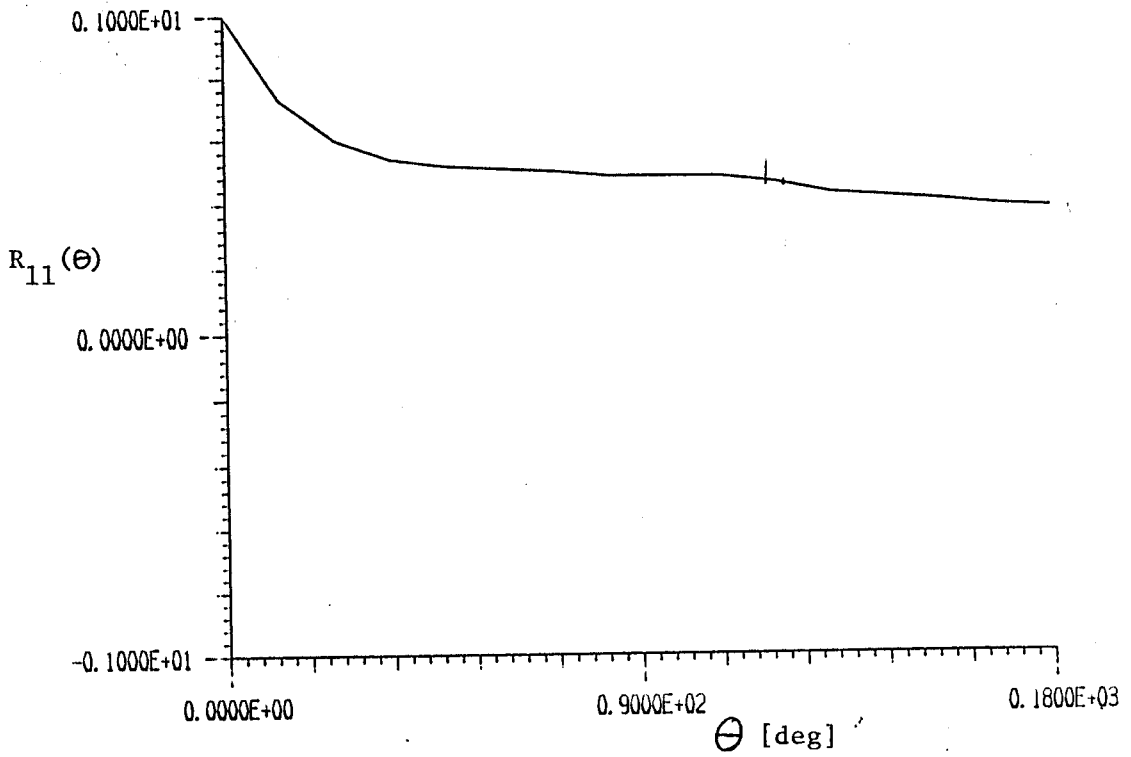


Figure 5.3.2(a) $R_{11}(\theta)$ at $x/D=3, r/D=0.26$

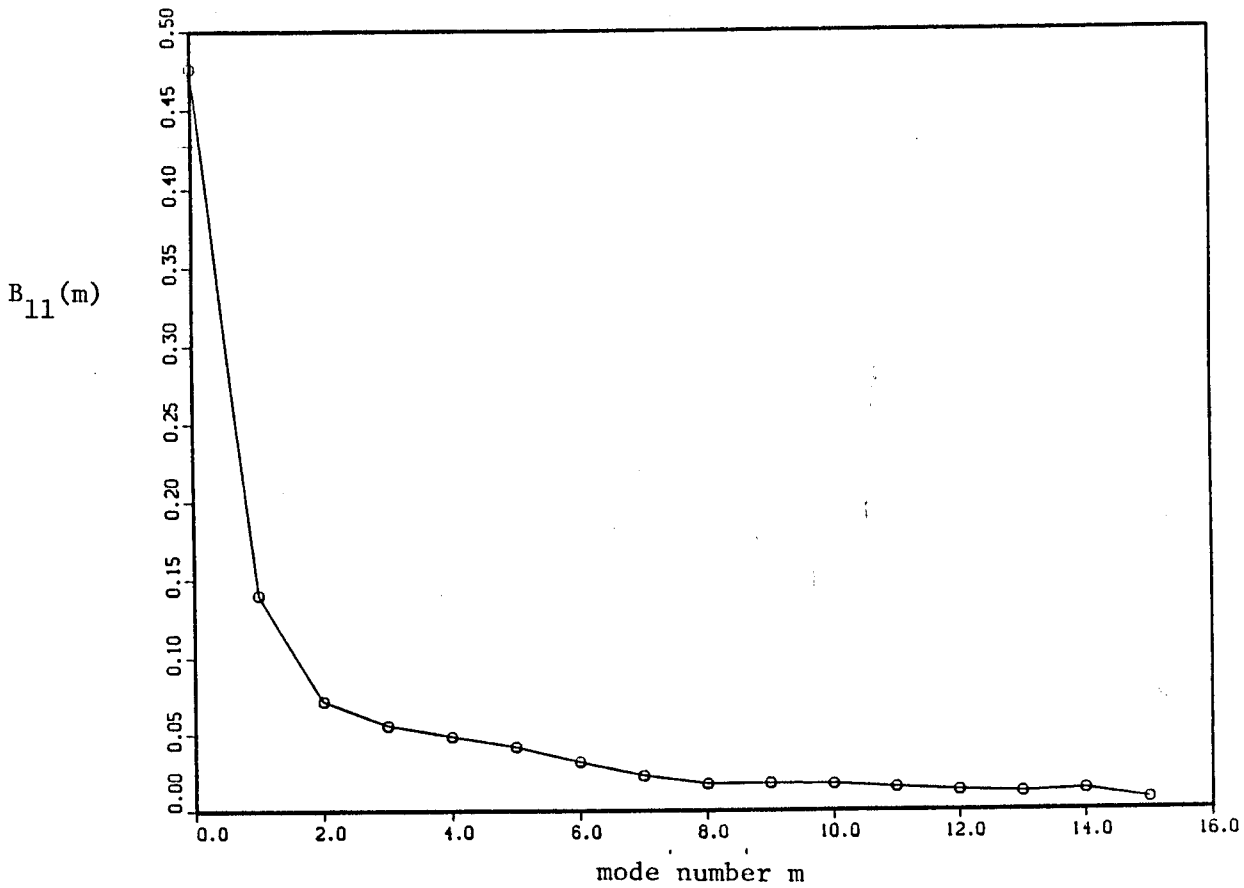


Figure 5.3.2(b) $B_{11}(m)$ at $x/D=3, r/D=0.26$

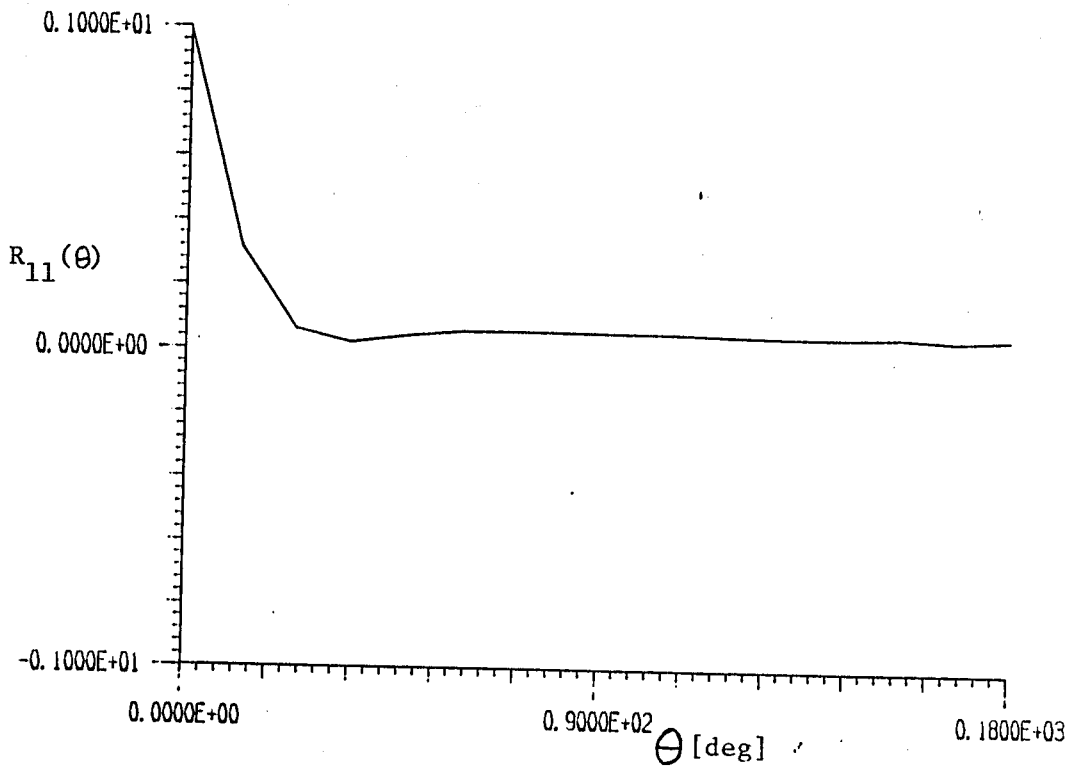


Figure 5.3.3(a) $R_{11}(\theta)$ at $x/D=3, r/D=0.39$

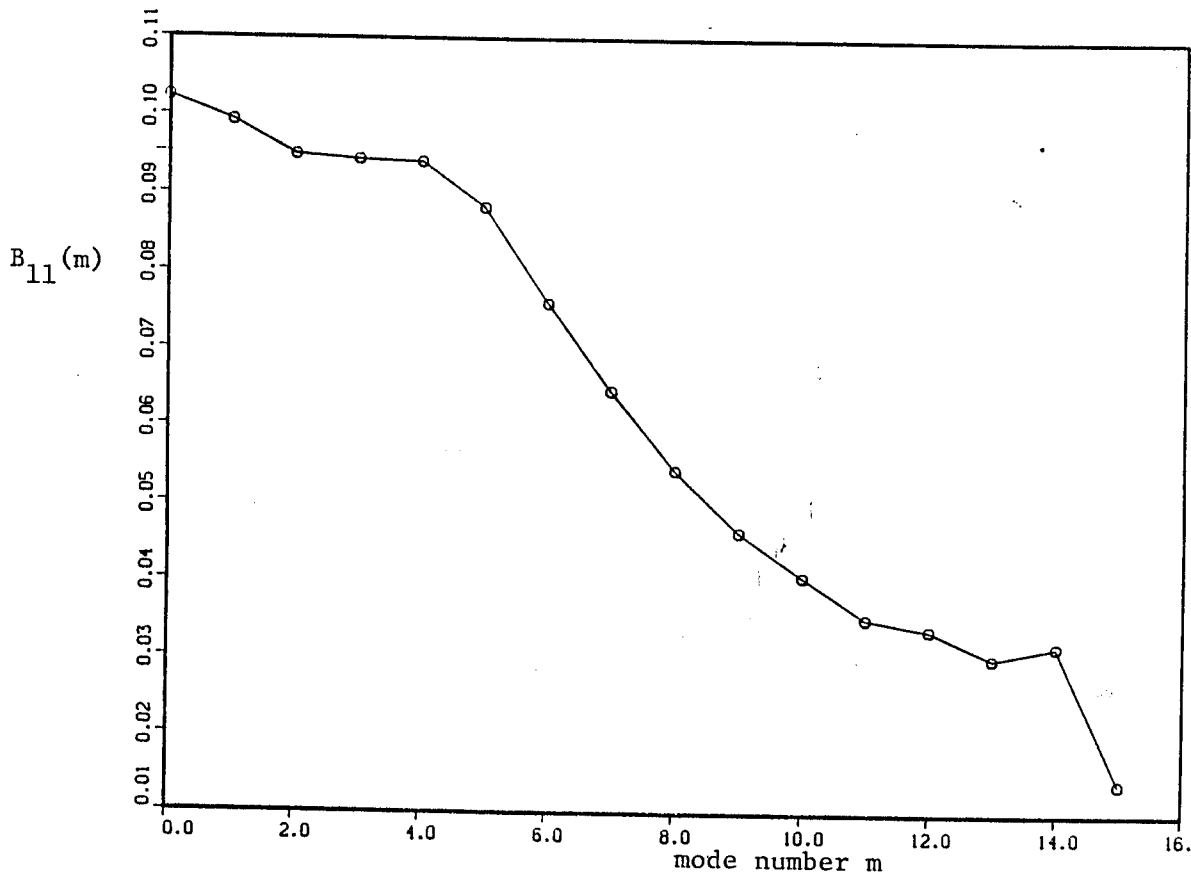


Figure 5.3.3(b) $B_{11}(m)$ at $x/D=3, r/D=0.39$

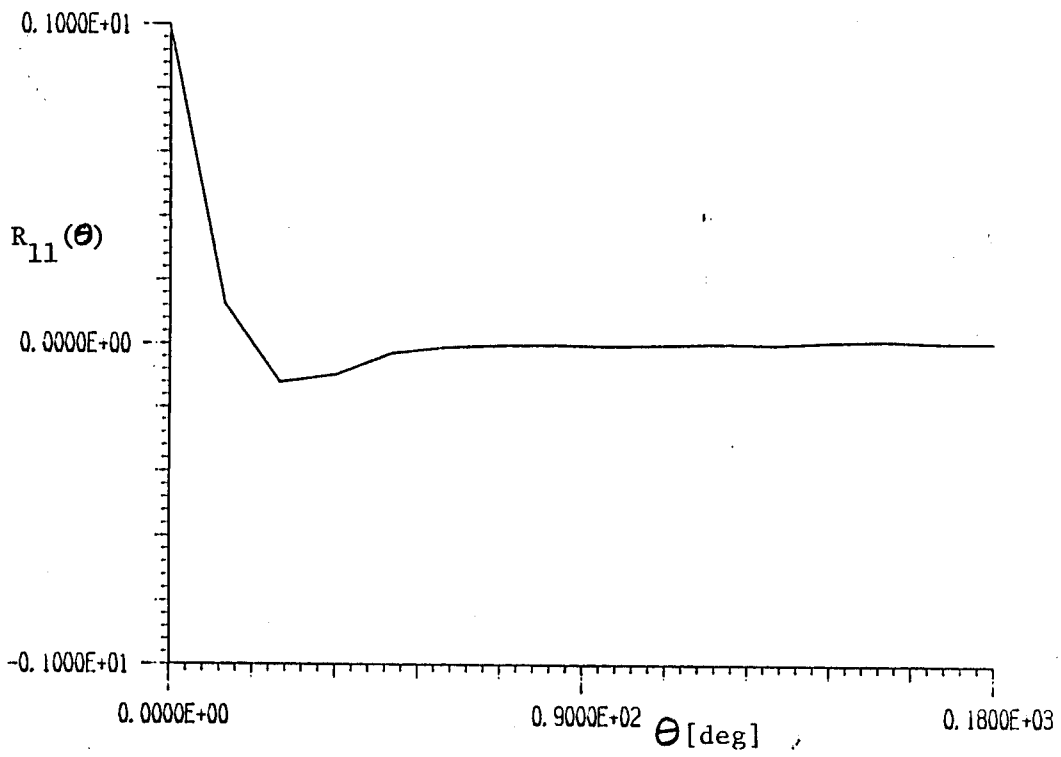


Figure 5.3.4(a) $R_{11}(\theta)$ at $x/D=3, r/D=0.52$

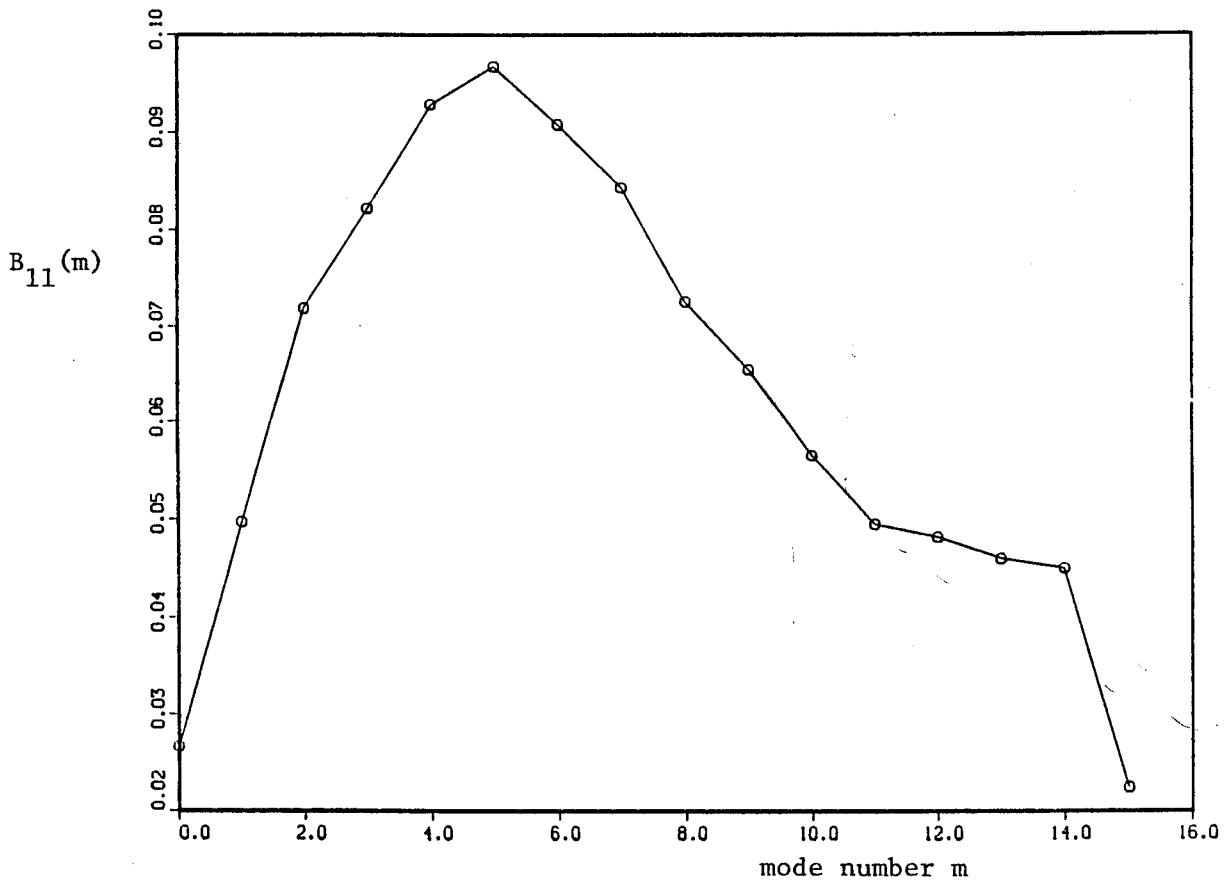


Figure 5.3.4(b) $B_{11}(m)$ at $x/D=3, r/D=0.52$

5.3.2 Results of the Orthogonal Decomposition - Phase 3

The inhomogenous problem was solved using Lumley's Orthogonal Decomposition. For each mode number/frequency combination equation (5.3.1) was solved numerically using the measured values $A_{11}(r, r', f, m)$. The numerical approximation to equation (5.3.1) was discussed in section 5.1.

The first 3 eigenspectra for modes 0 and 1 are shown plotted in Figures 5.3.5 and 5.3.6. The first eigenspectrum for each of the two modes is seen to dominate. These results are consistent with those obtained from phases 1 and 2. It is useful to look at the amount of energy contained in the first eigenspectrum of mode 0, $\lambda^{(1)}(f, 0)$ compared to that contained in all the modes combined. The ratio of interest is

$$\sum_f \lambda^{(1)}(f, 0) / \sum_f \sum_m \lambda^{(1)}(f, m). \quad (5.3.14)$$

This ratio is approximately equal to 0.23 indicating that while the first eigenfunction is dominant the structure of mode 0 is more complex. This result in conjunction with those from Section 5.3.1 suggests that the eigenspectra of certain of the remaining modes (i.e. modes 1,4,5,6) need also be included to give a physically realistic assessment of what is happening.

An additional interesting result can be seen by examining Figures 5.3.5 and 5.3.6. The peak of the first eigenspectrum for mode 0, $\lambda^{(1)}(f, 0)$ shown in Figure 5 is seen to be approximately 95 Hz which corresponds to an exit Strouhal number equal to 0.45. This is consistent with the results from the low mach number jet of Long and Arndt (1985) and with the high mach number jet of Stromberg et al.

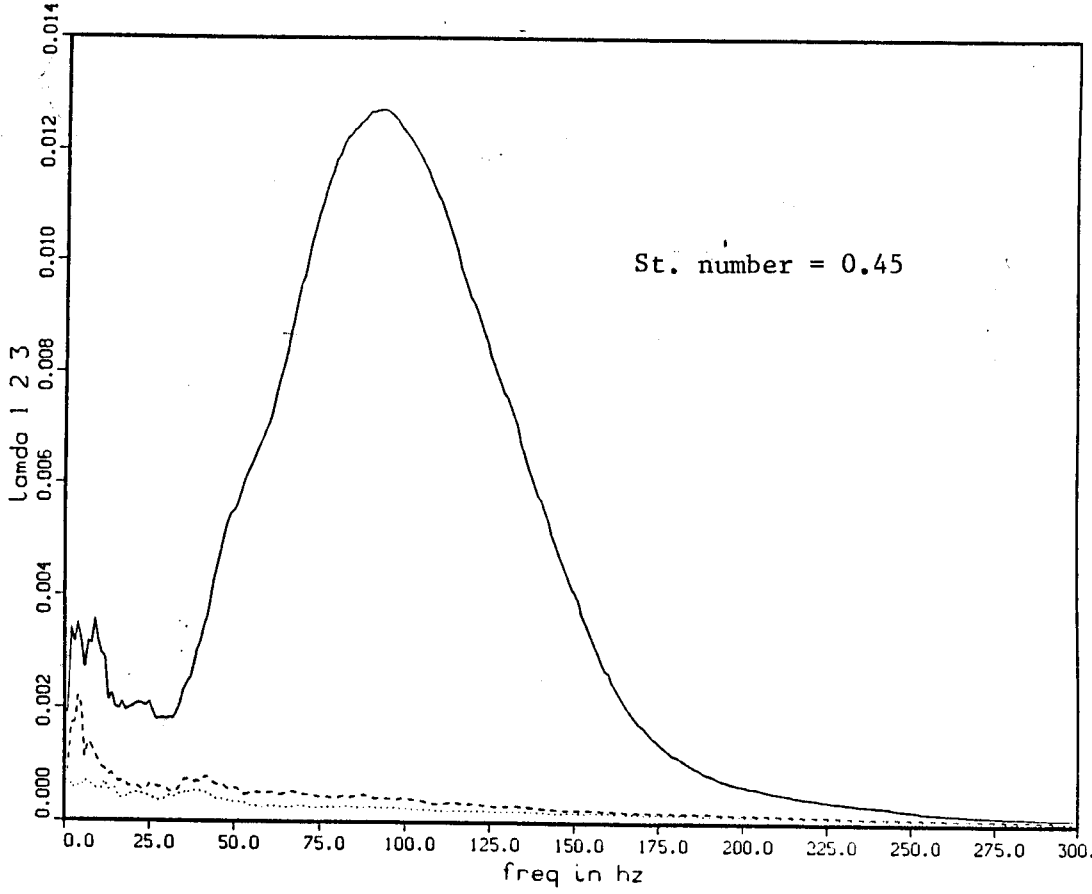


Figure 5.3.5 First 3 eigenspectra for mode 0

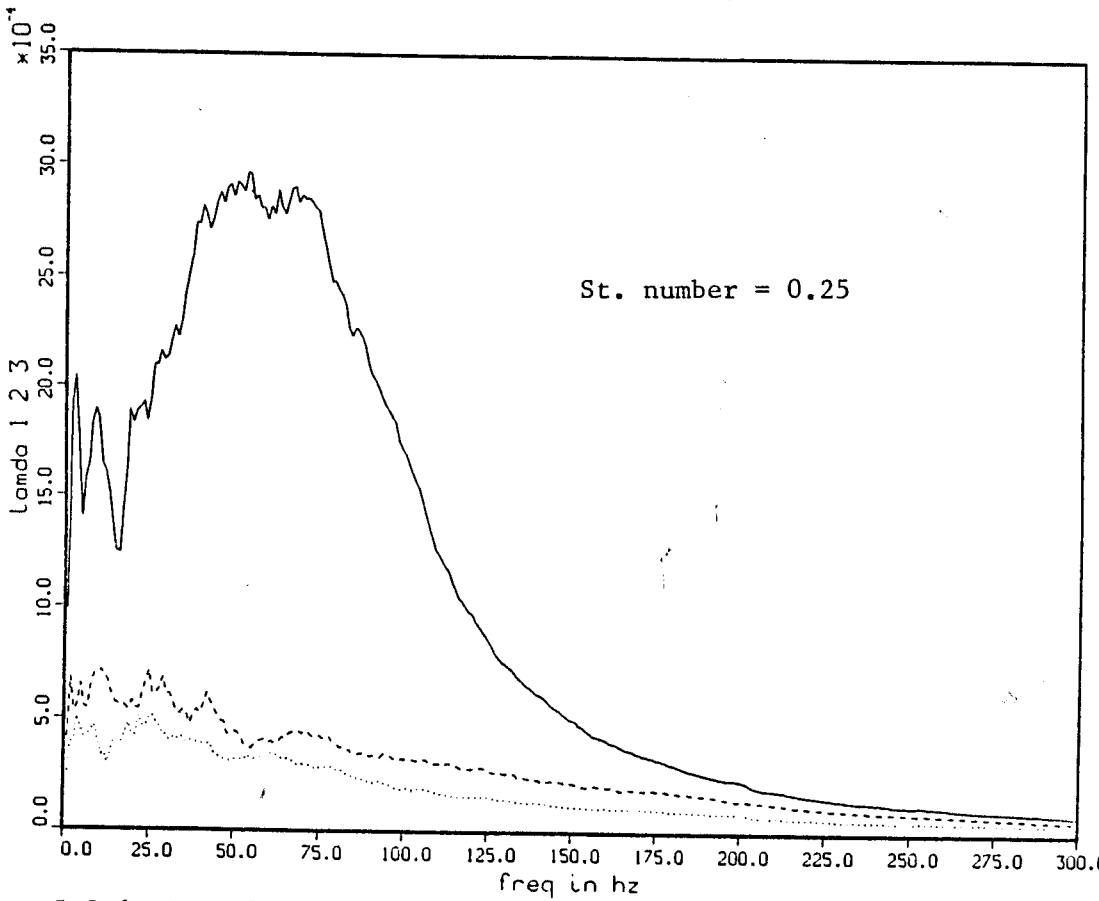


Figure 5.3.6 First 3 eigenspectra for mode 1

(1980). This is higher, however, than the value of 0.3 which is given by some authors (Crowe and Champagne, 1971). When examining Figure 5.3.6, however, the first eigenspectrum for mode 1, $\lambda^{(1)}(f,1)$, is seen to peak around 50 Hz which corresponds to an exit Strouhal number of 0.25. This would suggest that the Strouhal number of 0.3 represents an average over the first few azimuthal modes. If so, the orthogonal decomposition used here would seem to have a real advantage over the earlier techniques in that it can distinguish clearly these phenomena.

For the sake of comparison to the initial experiments discussed in sections 5.1 and 5.2 a brief review of that problem is given below. The eigenvalue problem that was solved is

$$\int_0^R \Phi_{11}(r, r', f) \Psi^{(n)}(r', f) dr' = \lambda^{(n)}(f) \Psi^{(n)}(r, f) \quad (5.3.15)$$

where Φ_{11} is the cross-spectral tensor.

From the general Hilbert-Schmidt theory Φ_{11} can be reconstructed from the eigenvalues and eigenfunctions solved for in (5.3.15) by

$$\Phi_{11}(r, r', f) = \sum_n \lambda^{(n)}(f) \Psi^{(n)}(r, f) \Psi^{*(n)}(r', f). \quad (5.3.16)$$

Note the difference between equations (5.3.1) and (5.3.15). In (5.3.1) the integral eigenvalue problem is performed using the azimuthal coefficients A_{11} obtained from the breakdown of $\Phi_{11}(r, r', f, \theta)$ versus its azimuthal modes. The problem in (5.3.15), however, is performed over $\Phi_{11}(r, r', f)$ since the azimuthal dependence had not been obtained at the time phase 1 was performed.

The eigenspectra computed from (5.3.15) are shown plotted in Figure 5.3.7. A similar dominance of the first eigenspectrum

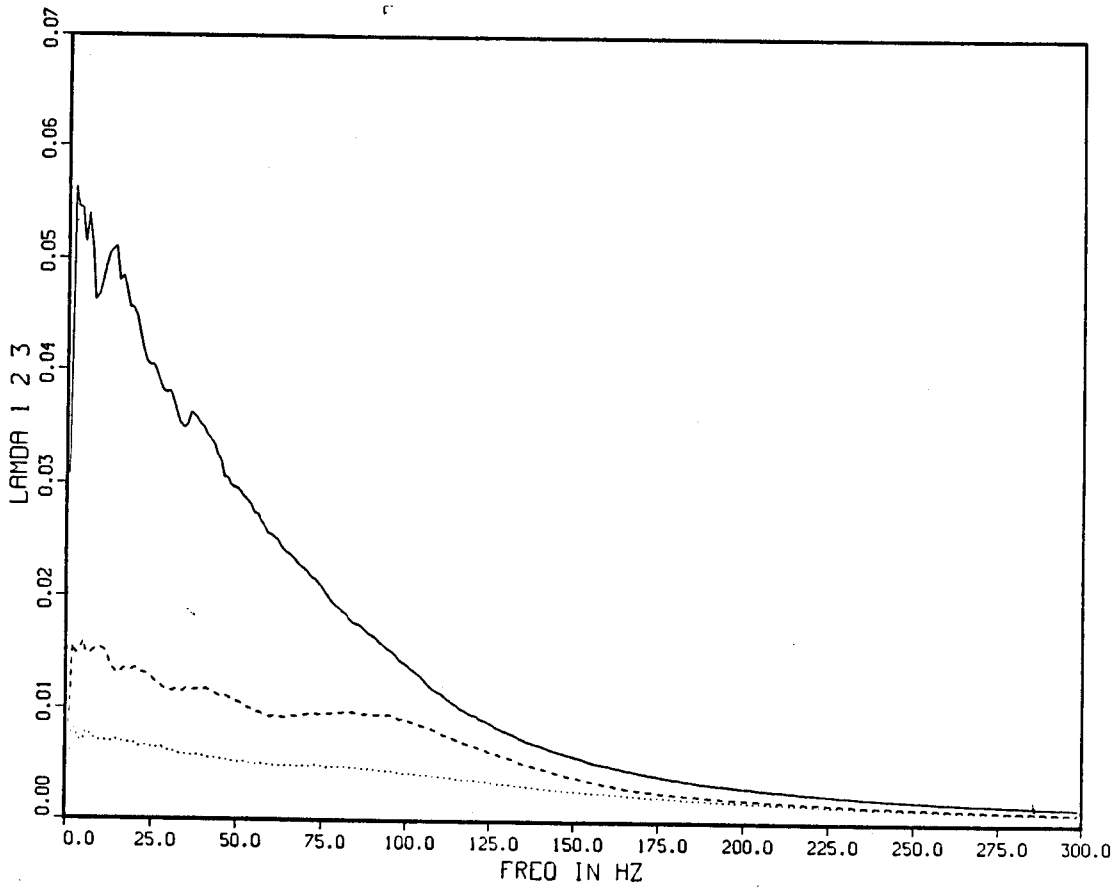


Figure 5.3.7 First 3 eigenspectra from phase 1 (radius and time only)

(compared to Figures 5.3.5 and 5.3.6) is observed here also. Although no obvious analytical relationship exists between the first eigenspectrum from the radial-only problem $[\lambda^{(1)}(f)]$ and the first eigenspectrum from the radial and azimuthal problem, $[\lambda^{(1)}(f, m)]$ it is still instructive to compare them by looking at the following ratio,

$$\sum_f \lambda^{(1)}(f) / \sum_f \sum_m \lambda^{(1)}(f, m). \quad (5.3.17)$$

In other words, by adding the azimuthal dependence, has more of the total energy been gained or did the initial experiment lump all the energy into $\lambda^{(1)}(f)$? In this case the ratio in (5.3.17) is approximately equal to 0.9. This would suggest that the initial problem did contain most of the azimuthal variation, only that it was mapped somehow, to the lower dimensional problem. These results are consistent with those of Moin (private communication).

A further comparison can be made between the two experiments. From the general Hilbert-Schmidt theory it can be shown that the complex coefficients can be reconstructed from the eigenvalues and eigenvectors in the following manner,

$$A_{11}(r, r, f, m) = \sum_{n=1}^N \lambda^{(n)}(f, m) \Psi^{(n)}(r, f, m) \Psi^{(n)*}(r, f, m) \quad (5.3.18)$$

Also, by examining (5.3.16) and setting $r = r'$ the cross spectrum reduces to

$$\Phi_{11}(r, r, f) = \sum_{n=1}^N \lambda^{(n)}(f) \Psi^{(n)}(r, f) \Psi^{(n)*}(r, f). \quad (5.3.19)$$

If both sides of (5.3.18) and (5.3.19) are summed over f , and n is set equal to 1, the following ratios can be derived,

$$\sum_{\mathbf{f}} \lambda^{(1)}(\mathbf{f}, m) \Psi^{(1)}(\mathbf{r}, \mathbf{f}, m) \Psi^{(1)*}(\mathbf{r}, \mathbf{f}, m) / \sum_{\mathbf{f}} A_{11}(\mathbf{r}, \mathbf{r}, \mathbf{f}, m) \quad (5.3.20)$$

and

$$\sum_{\mathbf{f}} \lambda^{(1)}(\mathbf{f}) \Psi^{(1)}(\mathbf{r}, \mathbf{f}) \Psi^{(1)*}(\mathbf{r}, \mathbf{f}) / \sum_{\mathbf{f}} \Phi_{11}(\mathbf{r}, \mathbf{r}, \mathbf{f}). \quad (5.3.21)$$

For the 0th mode the ratio in (5.3.20) gives an indication of the contribution of the 1st term (obtained now from the inhomogeneous problem) to the total energy in the 0th mode. From Figure 5.3.8 an idea of the value of (5.3.10) for the 0th mode can be obtained. The solid line represents the denominator and the dashed line the numerator. Approximately 85% of the total is seen to be contained in the first term. It must be remembered, however, that the results of (5.3.20) must be interpreted along with those of (5.3.14) for the azimuthal problem. This combination gives a total contribution to the energy of at most 20% for the large eddy if only the 0th mode is used for its definition. From Fig. 5.3.9 the contribution of the large eddy (the ratio in 5.3.21) can be seen to be about 40% for the initial problem. This discrepancy in the two problems would suggest that the orthogonal decomposition is more efficient in the inhomogeneous direction (across the shear layer) than the harmonic decomposition applied in the azimuthal direction. This would suggest that the prevailing view of the large eddy as an axisymmetric vortex be modified somewhat. Instead of only using the 0th azimuthal mode, at least the 4th, 5th and 6th modes should be included in the definition. This would increase the energy content of the big eddy, and give a more realistic physical view of it. This is not surprising in light of the discussion in Section 5.2 concerning the number of terms needed

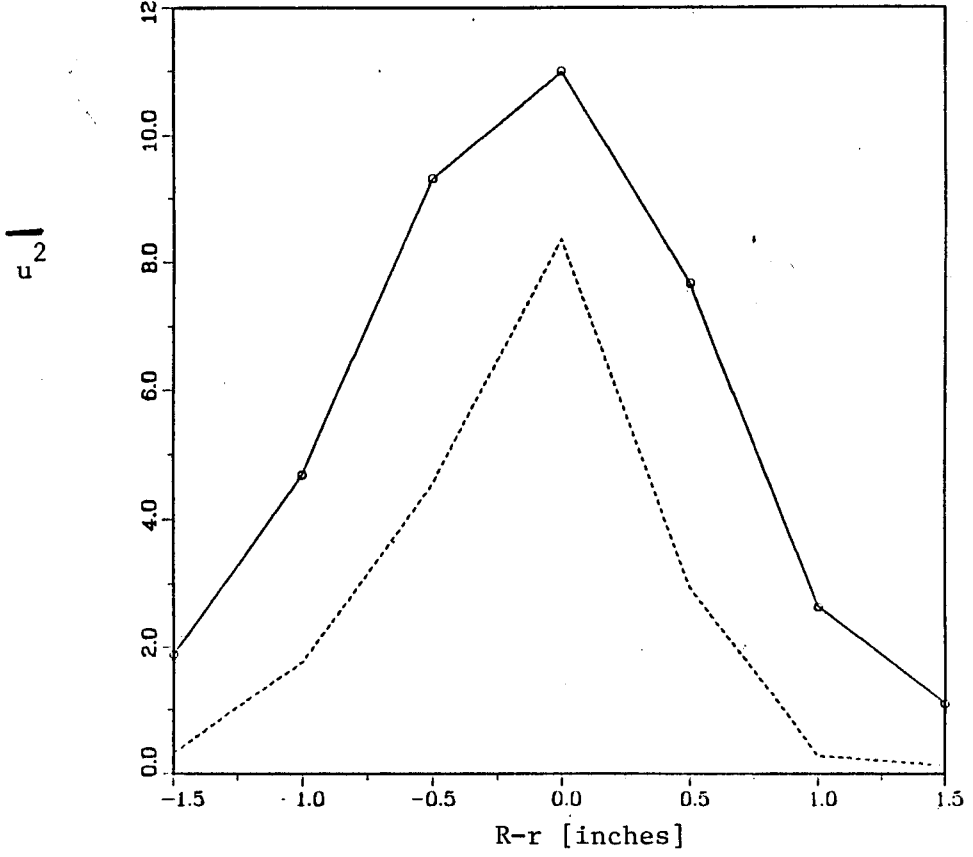


Figure 5.3.9 (—•—) $\overline{u^2}$, (----) contribution from first term to $\overline{u^2}$.

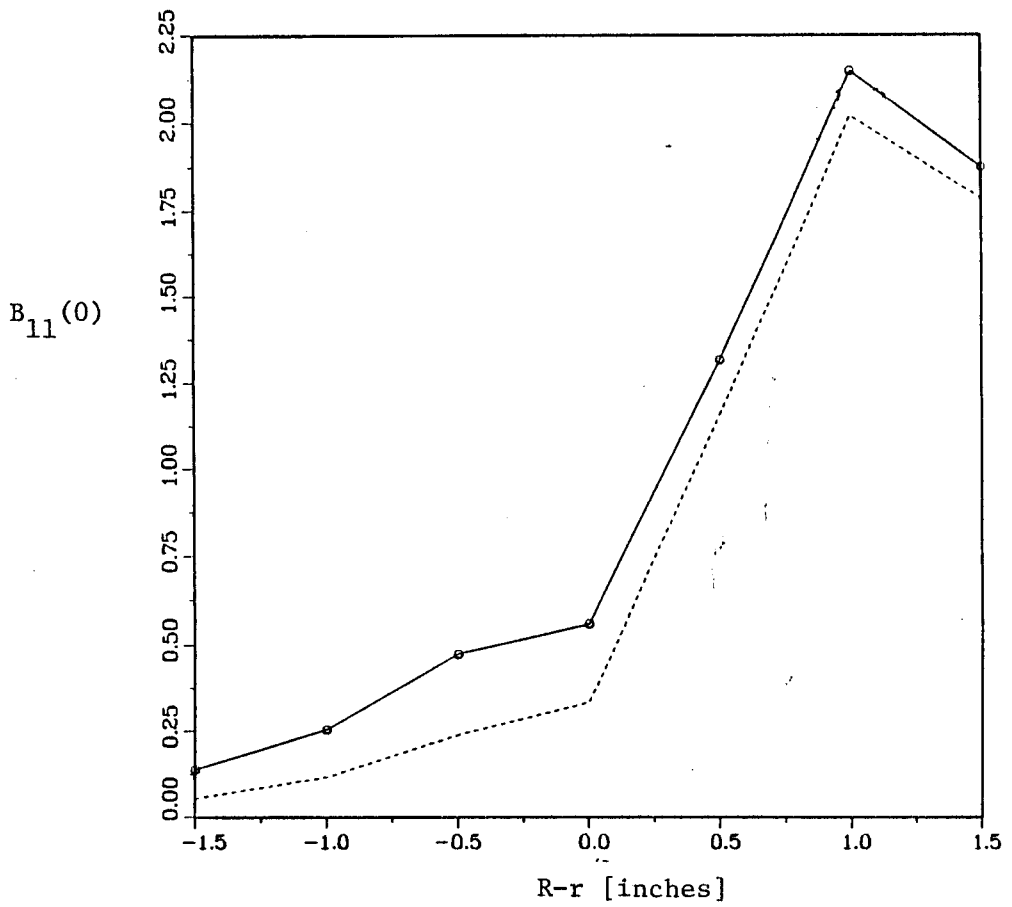


Figure 5.3.8 (—•—) B_{11} for mode 0, (----) contribution from 1 term.

in a particular direction (of finite energy) to represent the original kernel of the integral.

For the azimuthal direction a typical integral scale is $I \sim 20$ deg. while the span of finite energy is $L=360$ deg. so that the number of terms needed is

$$N \leq \frac{L}{I} \frac{360 \text{ deg.}}{20 \text{ deg.}} = 18.$$

This indicates that possibly as many as 18 terms would be needed in the azimuthal direction to represent the kernel as opposed to only 3 being needed in the strongly inhomogeneous direction across the shear layer.

The spatial sampling theorem suggested in Section 5.2 implies that at least $2N+1$ grid points be used in a particular direction to minimize spatial aliasing. In light of the above discussion of the azimuthal problem where $N \sim 18$ it was felt that the results from phase 3 were slightly aliased since only 16 grid points over 180 deg. were used (30 grid points over 360 deg.). As a result of this, in phase 4, 25 azimuthal positions were used over a span of 180 deg. (48 grid points over 360 deg.) in order to satisfy this constraint.

5.4 Azimuthal Problem Streamwise and Radial Velocity - Phase 4

These experiments extended the work discussed in section 5.3 to include the radial velocity components. It should be noted that all of the previous phases (excluding phase 2) are included in this final experiment.

A version of the orthogonal decomposition which utilizes the streamwise and radial velocity measurements from the jet can be

formulated as

$$\int \begin{bmatrix} A_{11}(r, r', f, m) & A_{12}(r, r', f, m) \\ A_{21}(r, r', f, m) & A_{22}(r, r', f, m) \end{bmatrix} \begin{bmatrix} \psi_1^{(n)}(r', f, m) \\ \psi_2^{(n)}(r', f, m) \end{bmatrix} dr' = \lambda^{(n)}(f, m) \begin{bmatrix} \psi_1^{(n)}(r, f, m) \\ \psi_2^{(n)}(r, f, m) \end{bmatrix} \quad (5.4.1)$$

where r is the radius in the jet mixing layer and the A 's are the complex coefficients defined by equations (2.2.3) and (2.2.4). Using the measured values of A_{11} , A_{12} , A_{21} and A_{22} equation (5.4.1) can be solved numerically for the eigenvalues and eigenfunctions as discussed in section 5.1.

5.4.1 Results of the Azimuthal Decomposition Analysis - Phase 4

Before looking at the results of the orthogonal decomposition in the inhomogeneous direction (equation 5.4.1) the breakdown into azimuthal modes will be examined as was done in section 5.3.

Equations similar to those written in section 5.3 are also written for A_{12} , A_{21} and A_{22} , (since the radial velocity was measured in addition to the streamwise) hence the corresponding R_{12} , R_{21} , R_{22} , B_{12} , B_{21} and B_{22} . In this phase however, $N=24$ in equation (5.3.8) so that a 48 point transform was performed for each r, r' and frequency combination.

It is useful to examine in detail the azimuthal correlations for which $r = r'$ so that B_{11} , B_{12} , R_{11} , R_{12} , etc. can be plotted for each radial position in the jet mixing layer. Selected examples of these

are plotted in Figures 5.4.1 - 5.4.8. The following progression across the jet mixing layer begins near the potential core and progresses towards the low speed side of the shear layer.

The High Speed Side of the Mixing Layer

Figure 5.4.1a shows measurements of $R_{11}(\theta)$ at a position near the potential core at $r/D=0.13$. There is clearly a strong correlation over the entire 180 deg. span. The corresponding $B_{11}(m)$ is plotted in Figure 5.4.1(b). The 0th mode (axisymmetric mode) can be seen to contain most of the energy indicating a strong ring-like structure at this position. This is the same result seen in section 5.3.

Figure 5.4.2(a) shows measurements of $R_{22}(\theta)$ at the same radial position as above. The radial correlation is seen to go to zero at 90 deg. and then becomes negatively correlated. The corresponding $B_{22}(m)$ is plotted in Figure 5.4.2(b). The 1st mode can be seen to dominate in this case. This would indicate either that the ring-like structures flap back and forth or that they are tilted slightly. This was also seen by Long and Arndt (1985) from pressure measurements in an axisymmetric jet.

Figure 5.4.3(a) shows measurements of $R_{12}(\theta)$ at the same radial position as the above. There is clearly a strong correlation over the entire 180 deg. span much the same as was seen in Figure 5.4.1.

Figure 5.4.3(b) shows the corresponding $B_{12}(m)$.

The Center Region of the Mixing Layer

Figure 5.4.4(a) shows measurements of $R_{11}(\theta)$ at a position on the high-speed side of the shear layer at $r/D=0.35$. The correlation falls off much more rapidly than that seen in Figure

5.4.1(a) indicating the presence of substantially smaller scale turbulence. The corresponding $B_{11}(m)$ is plotted in Figure 5.4.4(b). The 0th mode again dominates but in addition there appears another peak around the 4th, 5th or 6th mode. This result was also seen in phase 3.

Figure 5.4.5(a) shows measurements of $R_{22}(\theta)$ at the same radial position as the above at $r/D=0.35$. This correlation does not go negative like the R_{22} did in Figure 5.4.2(a). The corresponding $B_{22}(\theta)$ is plotted in Figure 5.4.5(b). Here the 0th mode comes into play along with the 1st mode as opposed to what was seen in Figure 5.4.2(b) where only the 1st mode dominated.

Figure 5.4.6(a) shows measurements of R_{12} at the same radial position as the above at $r/D=0.35$. An interesting thing happens here in that the correlation falls off very fast indicating the predominance of the small scale structures at this position. This is also seen by examining $B_{12}(\theta)$ shown in Figure 5.4.6(b) where the breakdown versus azimuthal modes is seen to be broad band with no distinct peaks. This is quite distinct from the core region where the Reynolds stress is dominated by the 0th mode. The $R_{12}(\theta)$ and $B_{12}(m)$ at $r/D=.46$ show much the same characteristics as those at $r/D=0.35$.

Figure 5.4.7(a) shows measurements of $R_{11}(\theta)$ at a position just to the high speed side of the center of the mixing layer, at $r/D=.46$. The correlation falls off very rapidly. The corresponding $B_{11}(m)$ is plotted in Figure 5.4.7(b). An interesting phenomenon occurs at this position. Instead of the 0th mode dominating as was seen in Figures 5.4.1 and 5.5.4, there is a shift here to the 4th, 5th and 6th modes.

Figure 5.4.8(a) shows measurements of $R_{12}(\theta)$ at a position just to the low-speed side of the center of the jet shear layer at $r/D=0.57$. Note that there is measurable correlation seen. The corresponding $B_{12}(m)$ is shown in Figure 5.4.9(b). Note the preference for the 4th, 5th and 6th modes. Contrast these with those from Figure 5.4.6.

The results for $R_{11}(\theta)$, $B_{11}(\theta)$, $R_{22}(\theta)$ and $B_{22}(\theta)$ at $r/D=0.57$ are much the same as those shown in Figures 5.4.7 and 5.4.5 respectively. $R_{12}(\theta)$ and $B_{12}(\theta)$ were the only correlations to show significant changes from $r/D=.46$ as seen by comparing Figures 5.4.6 and 5.4.8. The remaining correlations at the other positions in the mixing layer, $r/D=0.68$, $r/D=0.79$ and $r/D=0.9$ exhibit the same basic features as the correlations shown above.

5.4.2 Results of the Orthogonal Decomposition - Phase 4

The inhomogeneous problem was solved using the Orthogonal Decomposition. For each mode number frequency combination equation 5.4.1 was solved numerically using the measured values of $A_{11}(r, r', f, m)$, $A_{12}(r, r', f, m)$, $A_{21}(r, r', f, m)$ and $A_{22}(r, r', f, m)$. The numerical approximation to (5.4.1) was discussed in section 5.1.

The first three eigenspectra for modes 0 through 8 are shown plotted in Figures 5.4.9 - 5.4.17. The first eigenspectrum for each mode is seen to dominate (this was the case for the remaining modes also) indicating that one term is adequate for the description of the large eddy in the inhomogeneous directions. This is the same result seen in the earlier work discussed in sections 5.1 - 5.3.

The azimuthal mode-number-dependent Strouhal number noticed in section 5.3 is also seen here by examining Figures 5.4.9 and 5.4.10.

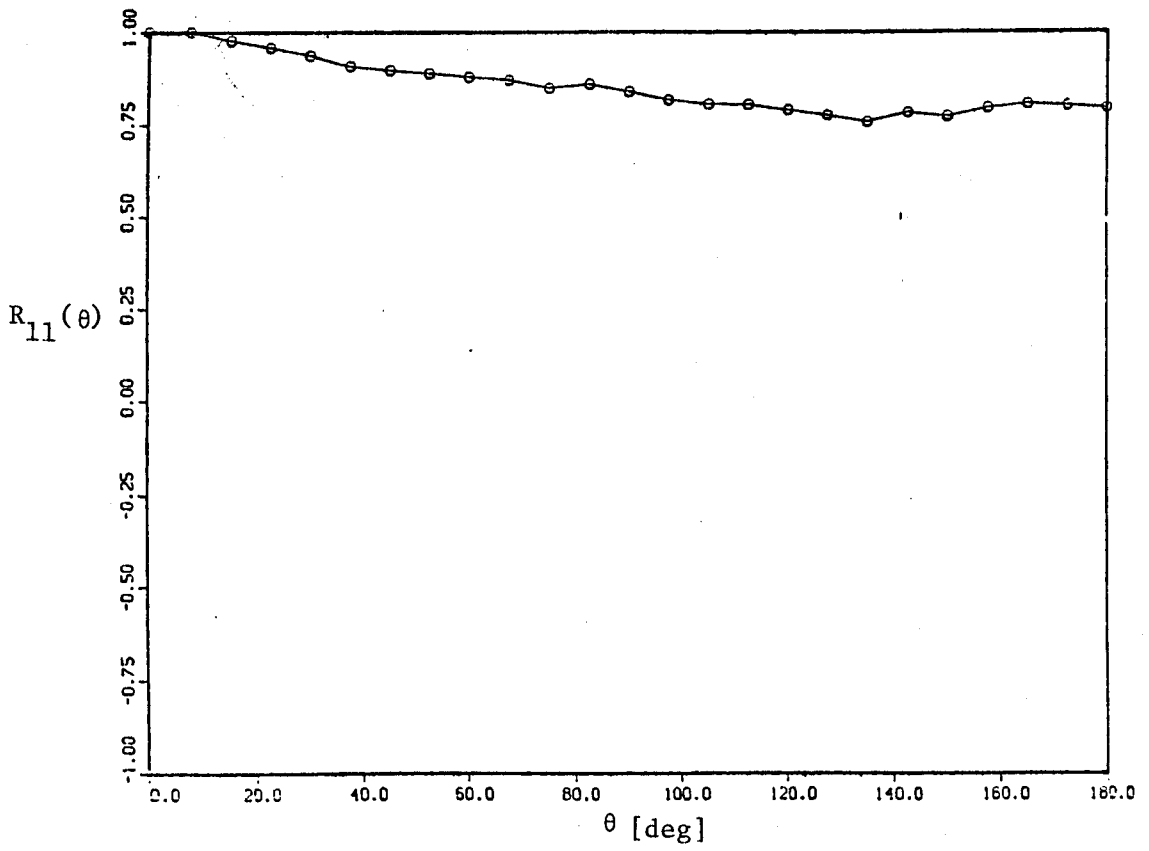


Figure 5.4.1(a) $R_{11}(\theta)$ at $r/D=0.13, x/D=3$

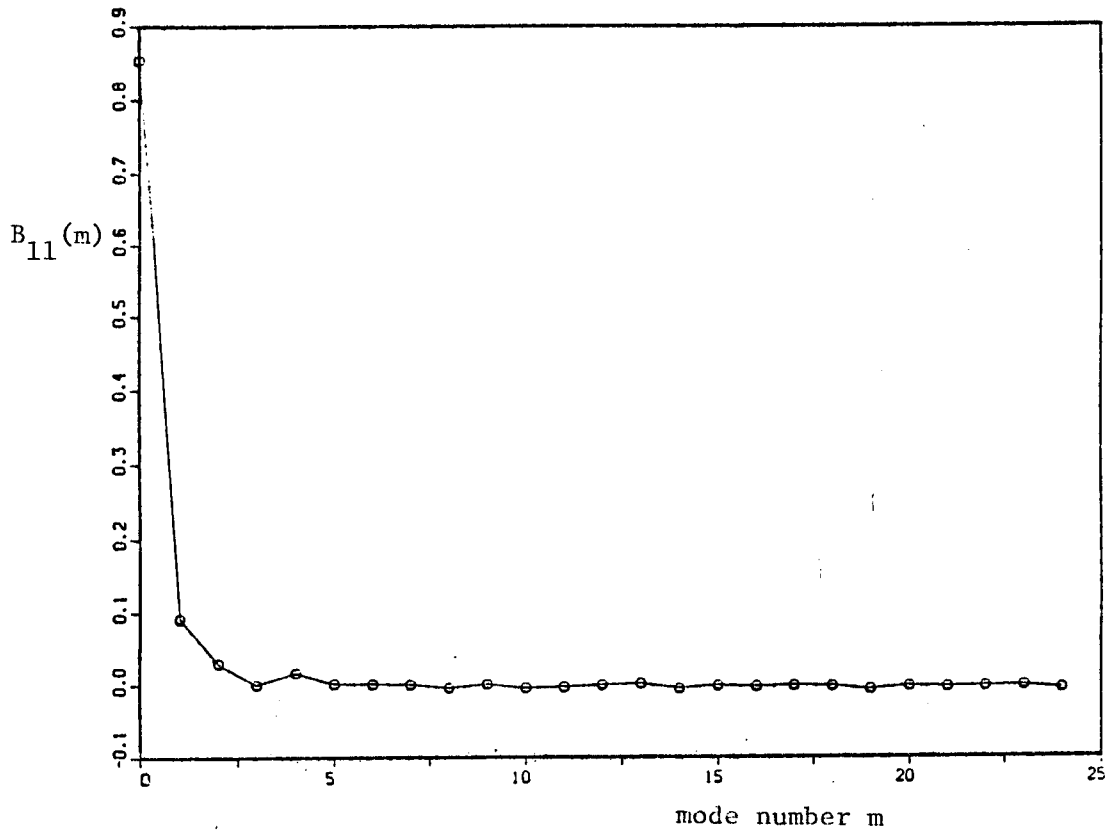


Figure 5.4.1(b) $B_{11}(m)$ at $r/D=0.13, x/D=3$

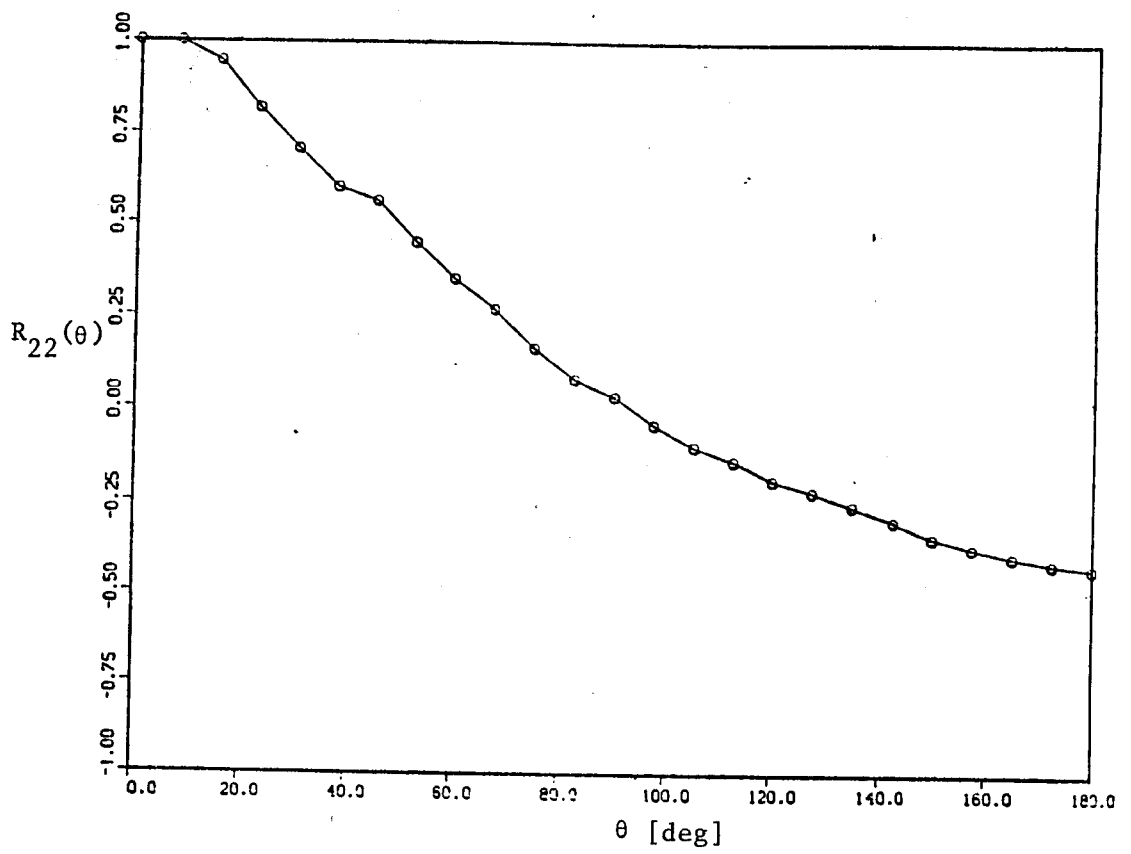


Figure 5.4.2(a) $R_{22}(\theta)$ at $r/D=0.13, x/D=3$

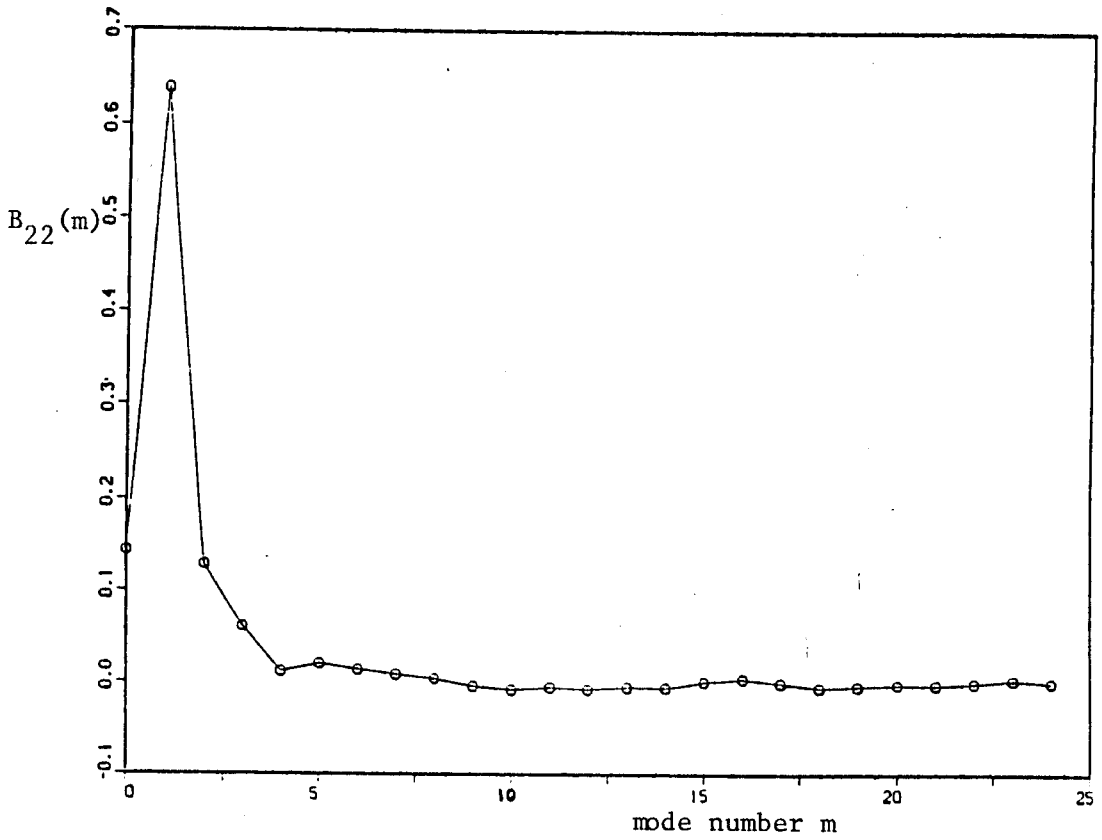


Figure 5.4.2(b) $B_{22}(m)$ at $r/D=0.13, x/D=3$

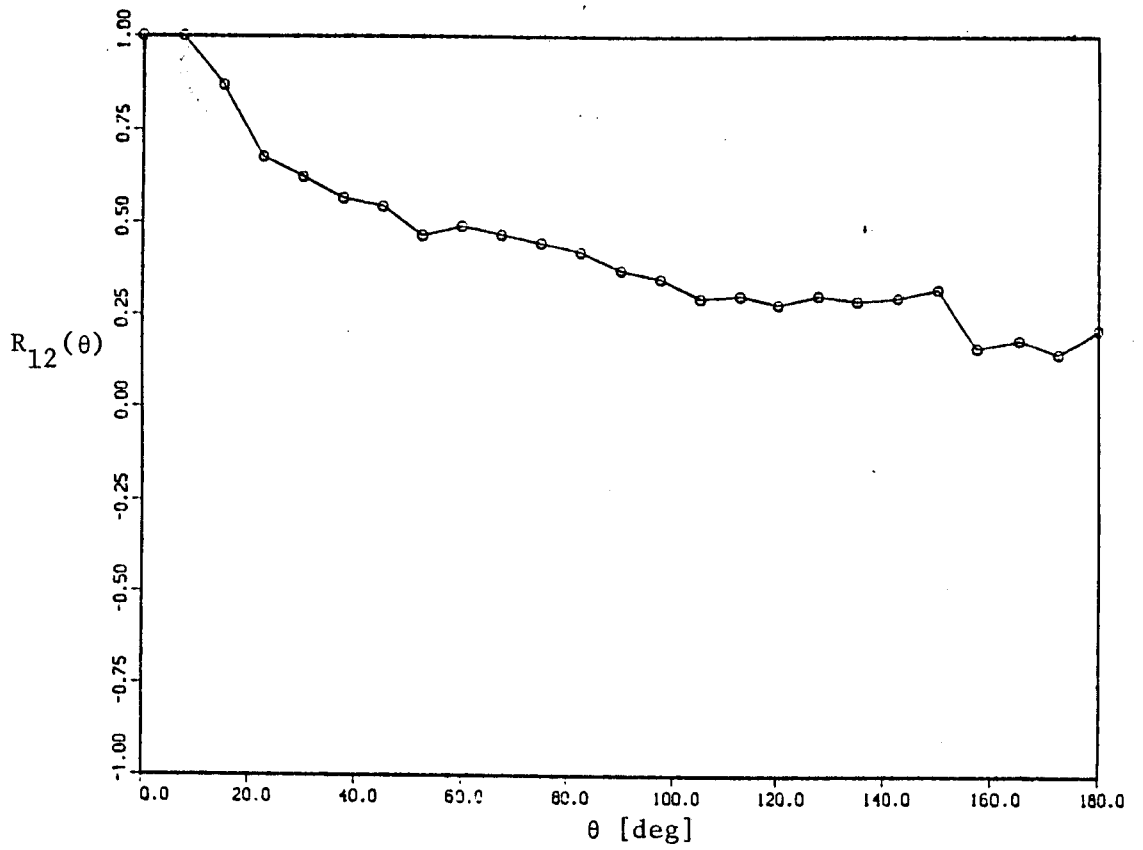


Figure 5.4.3(a) $R_{12}(\theta)$ at $r/D=0.13, x/D=3$

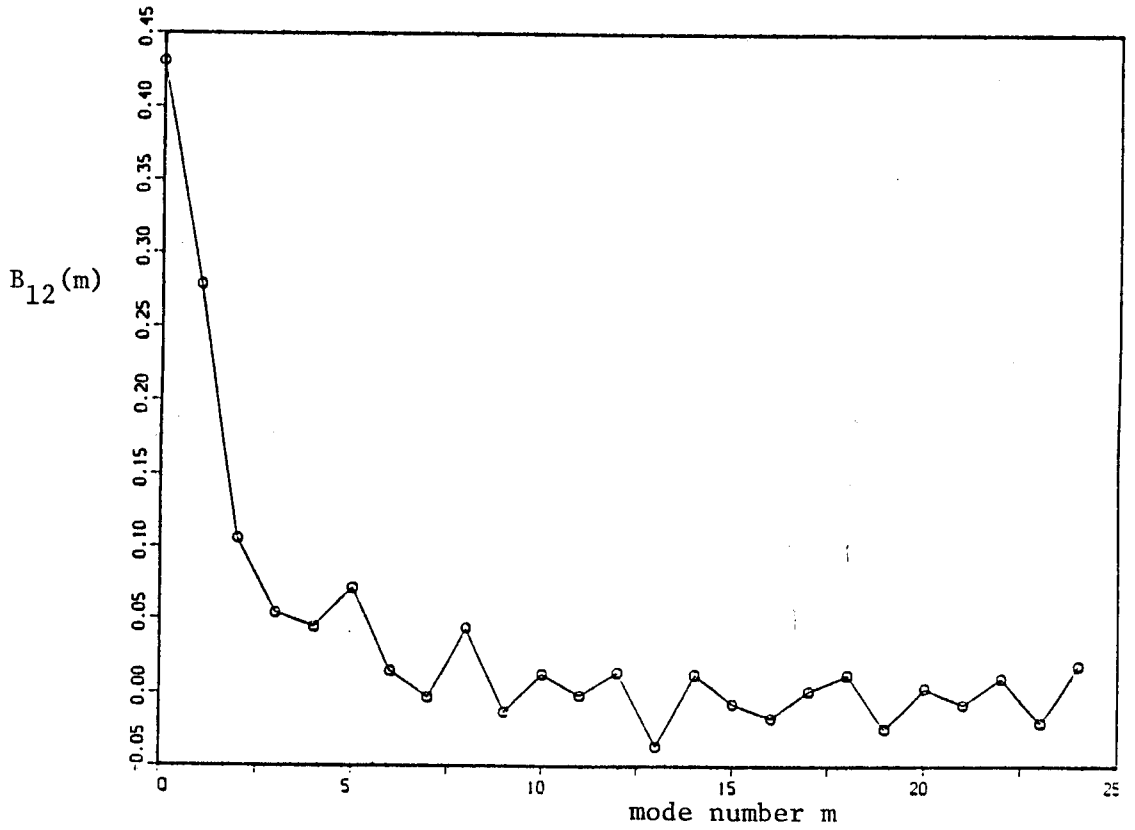


Figure 5.4.3(b) $B_{12}(m)$ at $r/D=0.13, x/D=3$

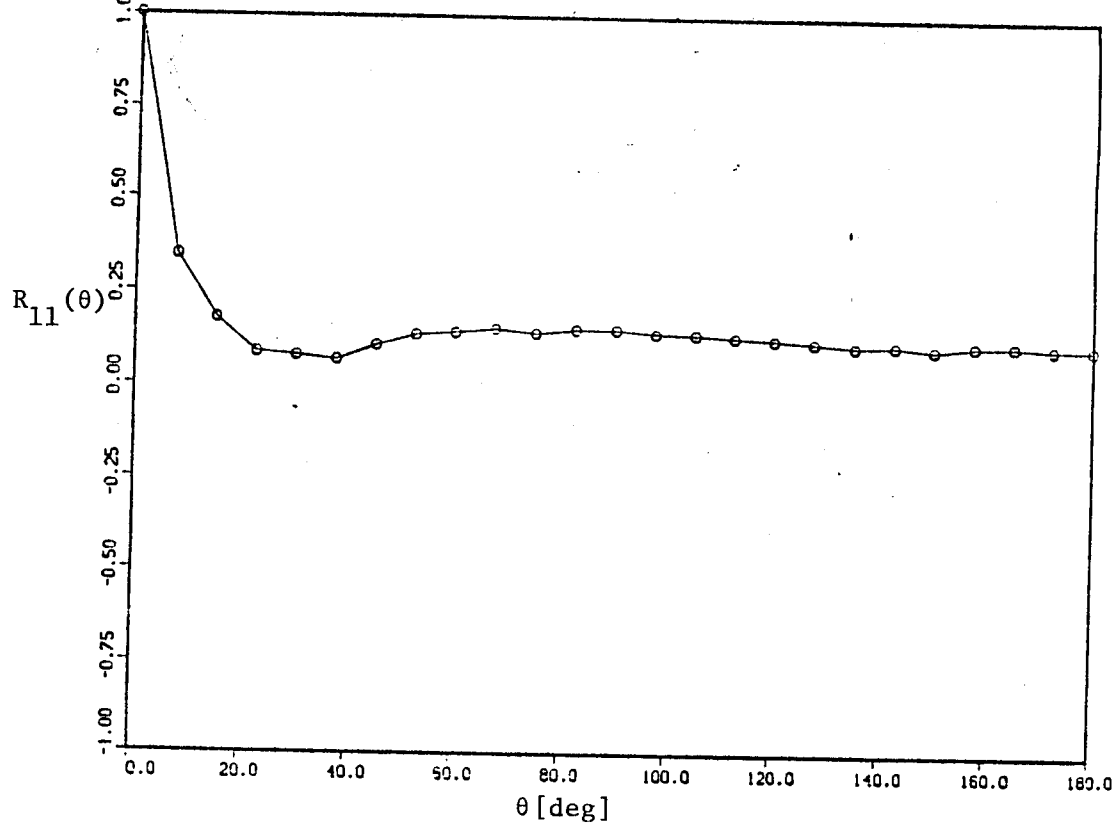


Figure 5.4.4(a) $R_{11}(\theta)$ at $r/D=0.35, x/D=3$

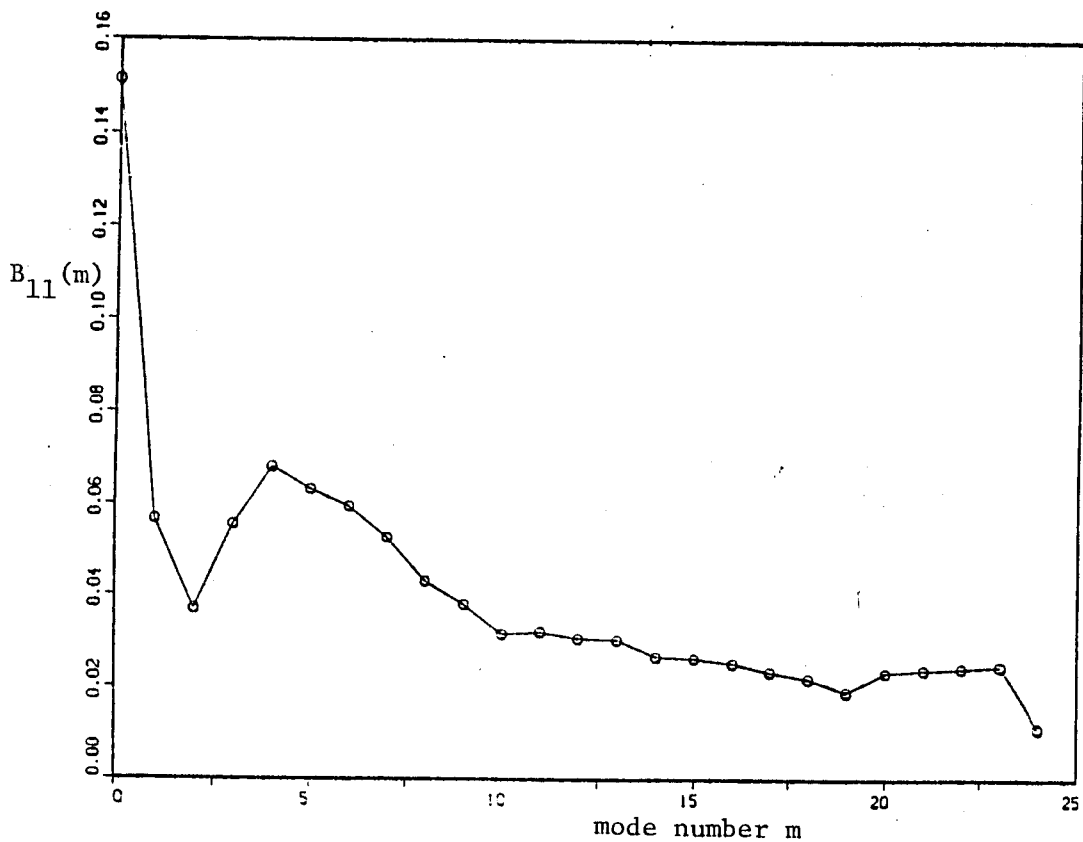


Figure 5.4.4(b) $B_{11}(m)$ at $r/D=0.35, x/D=3$

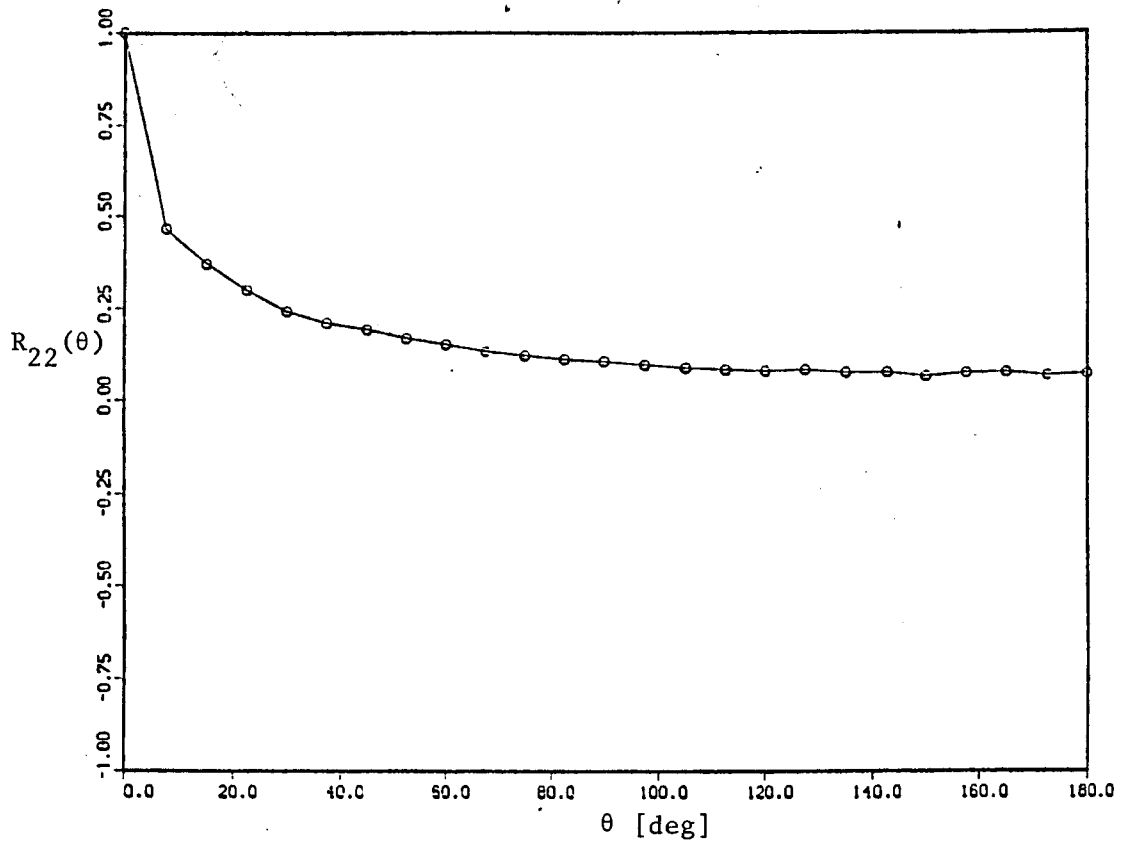


Figure 5.4.5(a) $R_{22}(\theta)$ at $r/D=0.35, x/D=3$

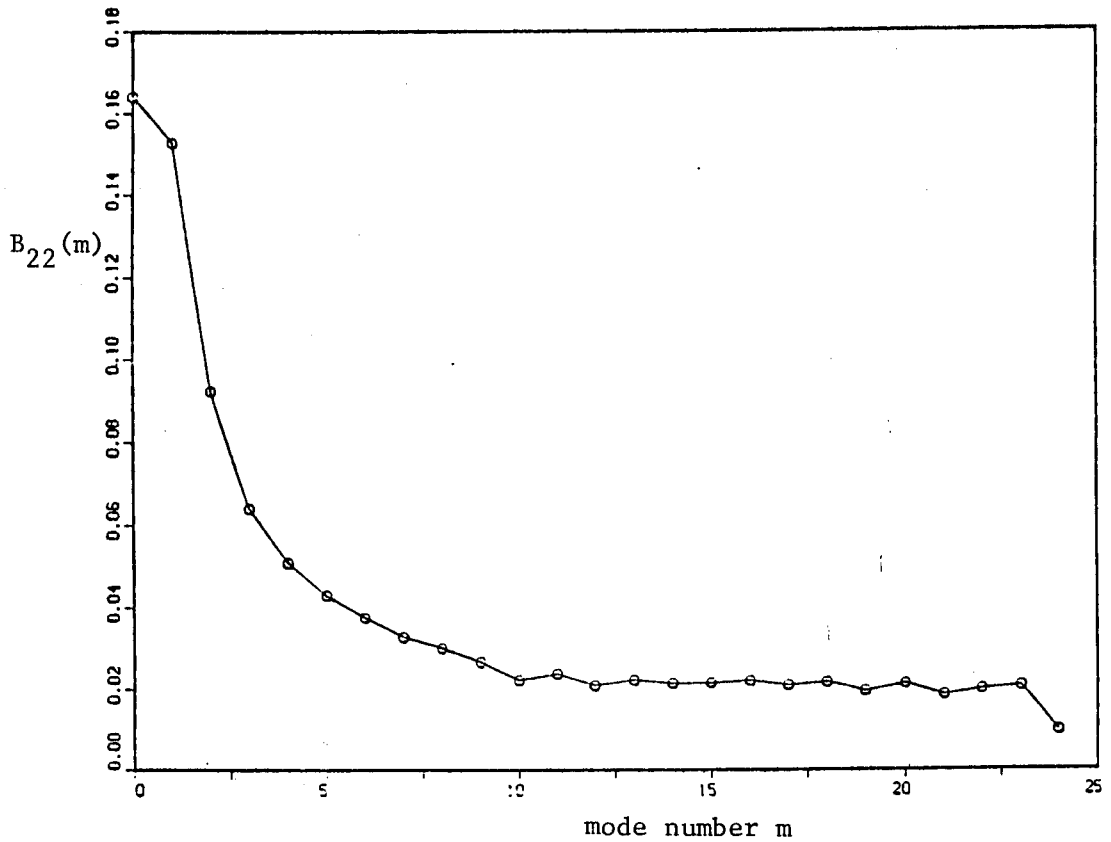


Figure 5.4.5(b) $B_{22}(m)$ at $r/D=0.35, x/D=3$

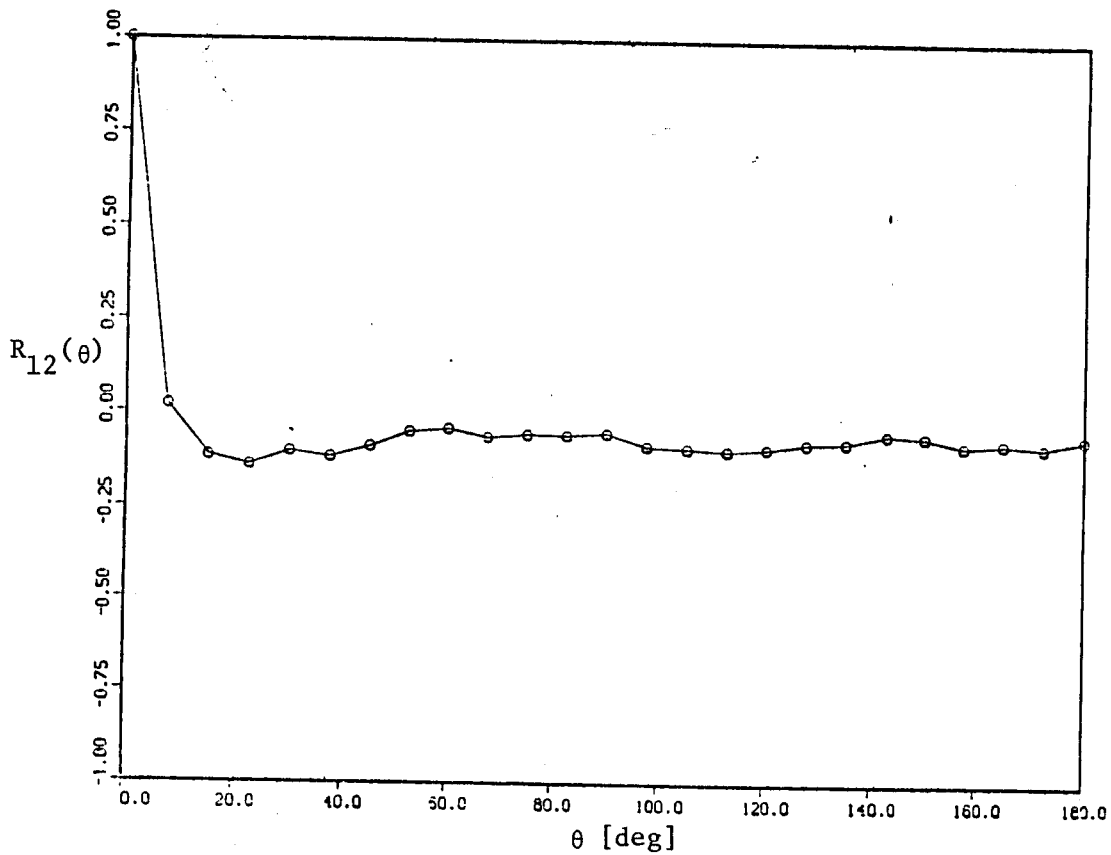


Figure 5.4.6(a) $R_{12}(\theta)$ at $r/D=0.35, x/D=3$

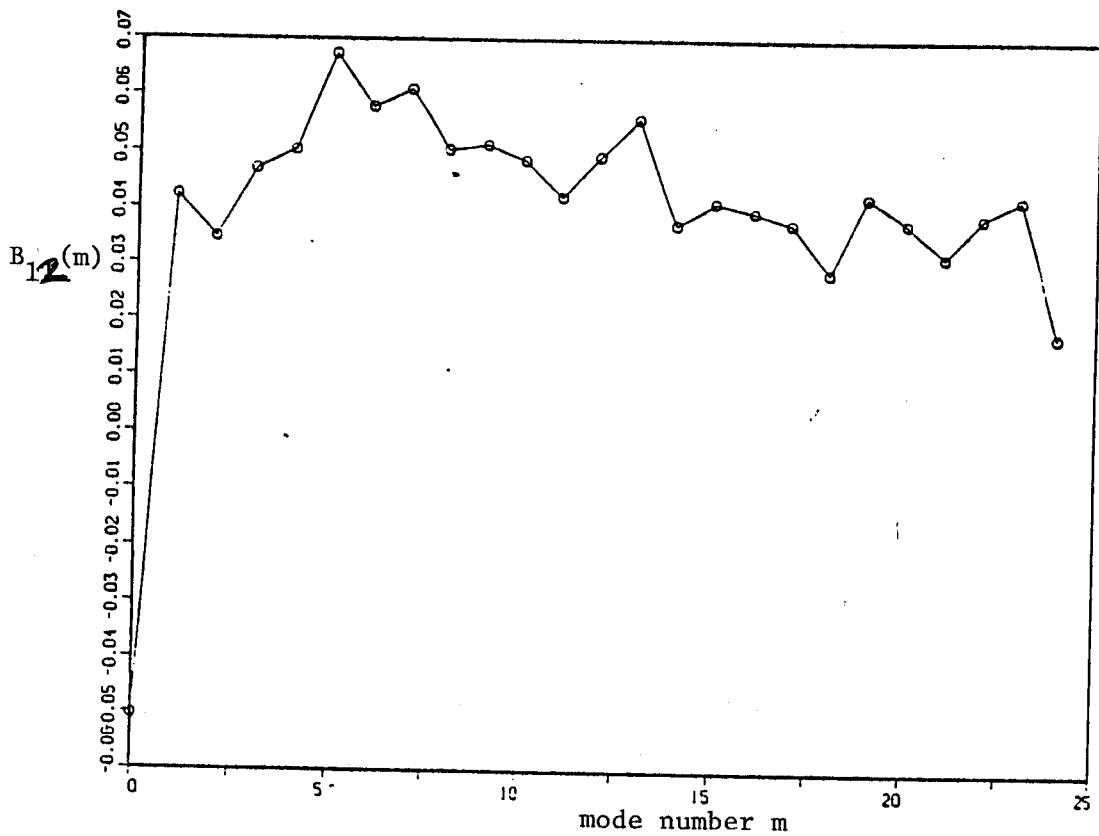


Figure 5.4.6(b) $B_{12}(m)$ at $r/D=0.35, x/D=3$

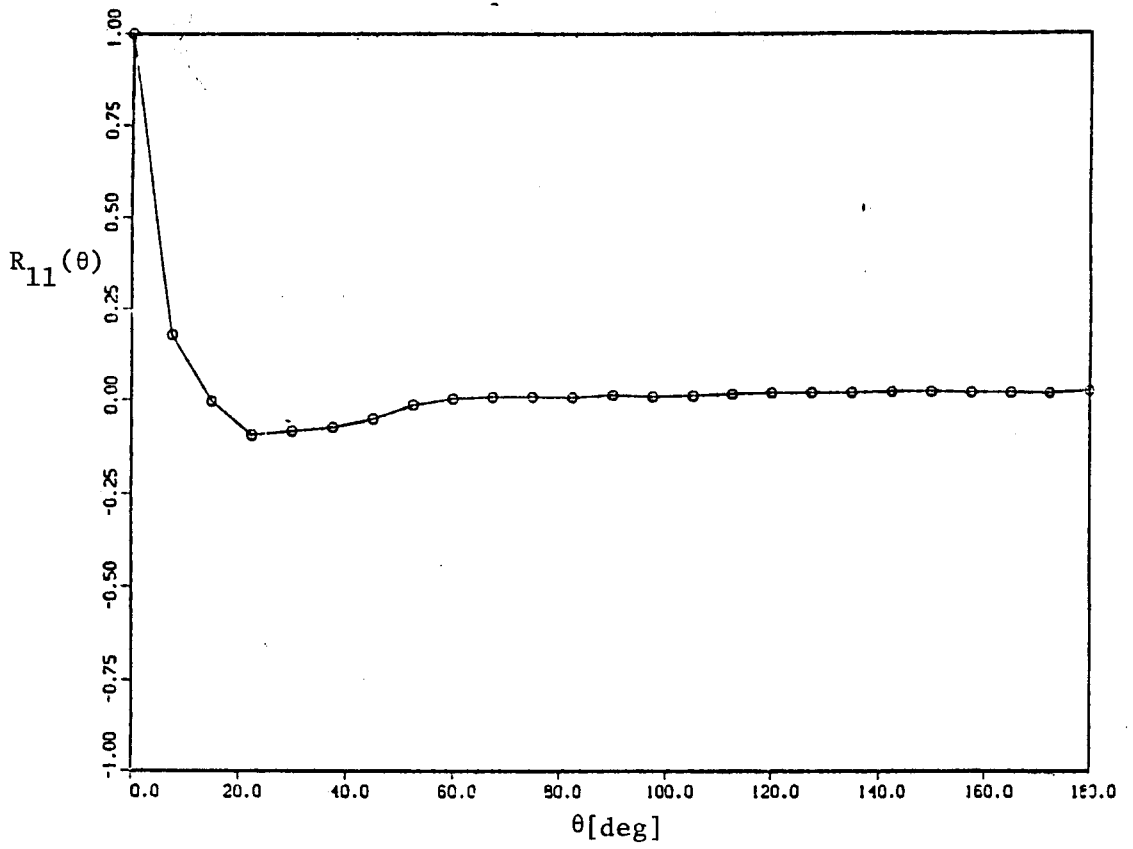


Figure 5.4.7(a) $R_{11}(\theta)$ at $r/D=0.46, x/D=3$

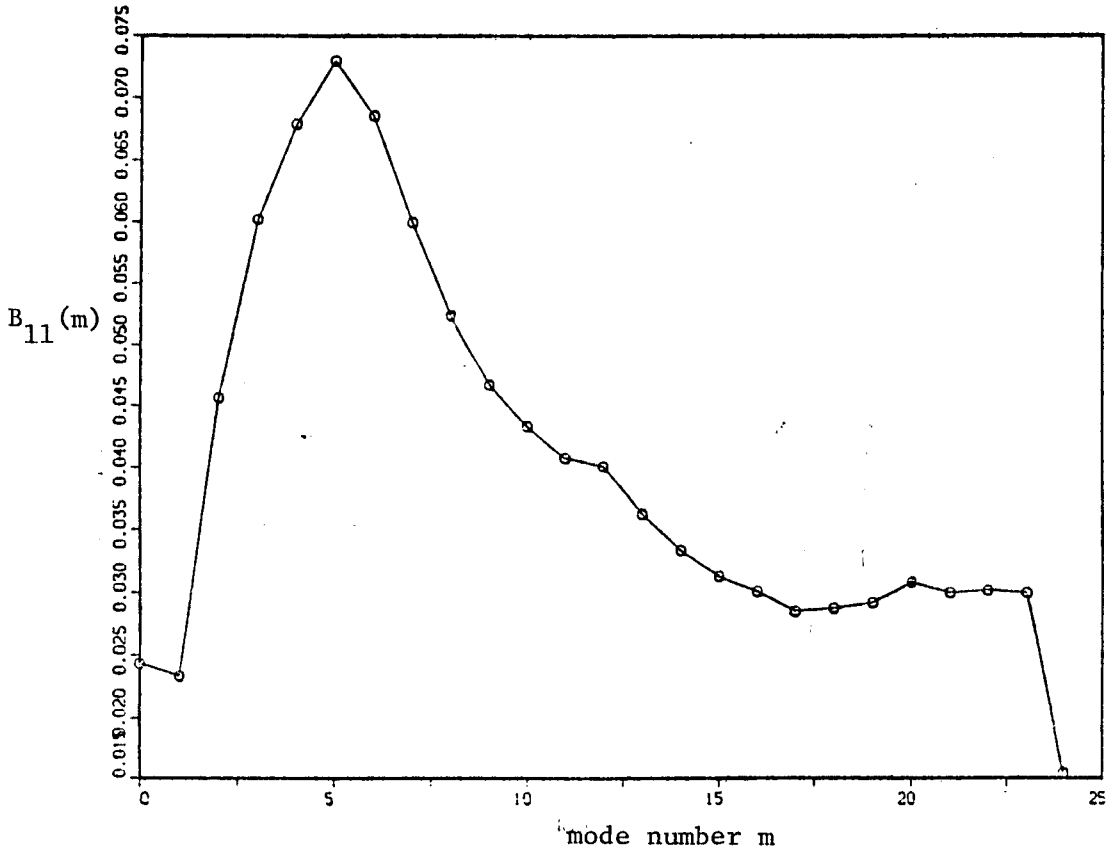


Figure 5.4.7(b) $B_{11}(m)$ at $r/D=0.46, x/D=3$

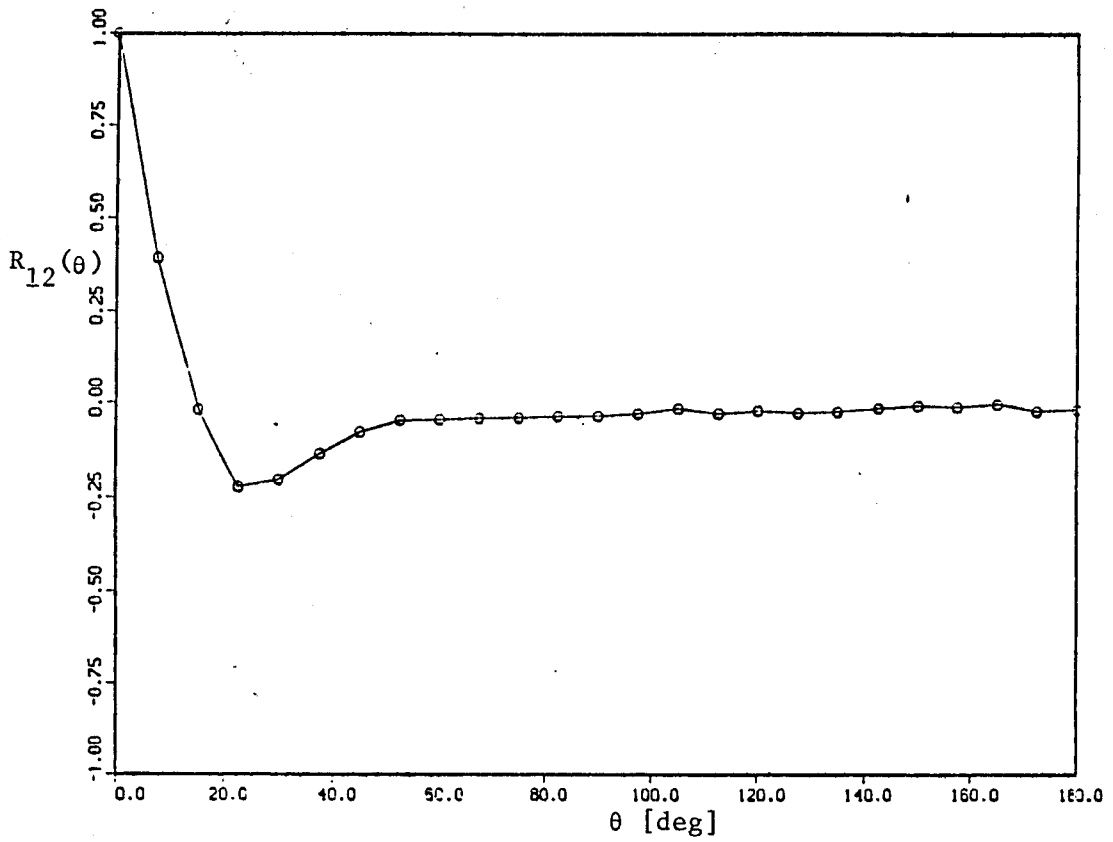


Figure 5.4.8(a) $R_{12}(\theta)$ at $r/D=0.57, x/D=3$

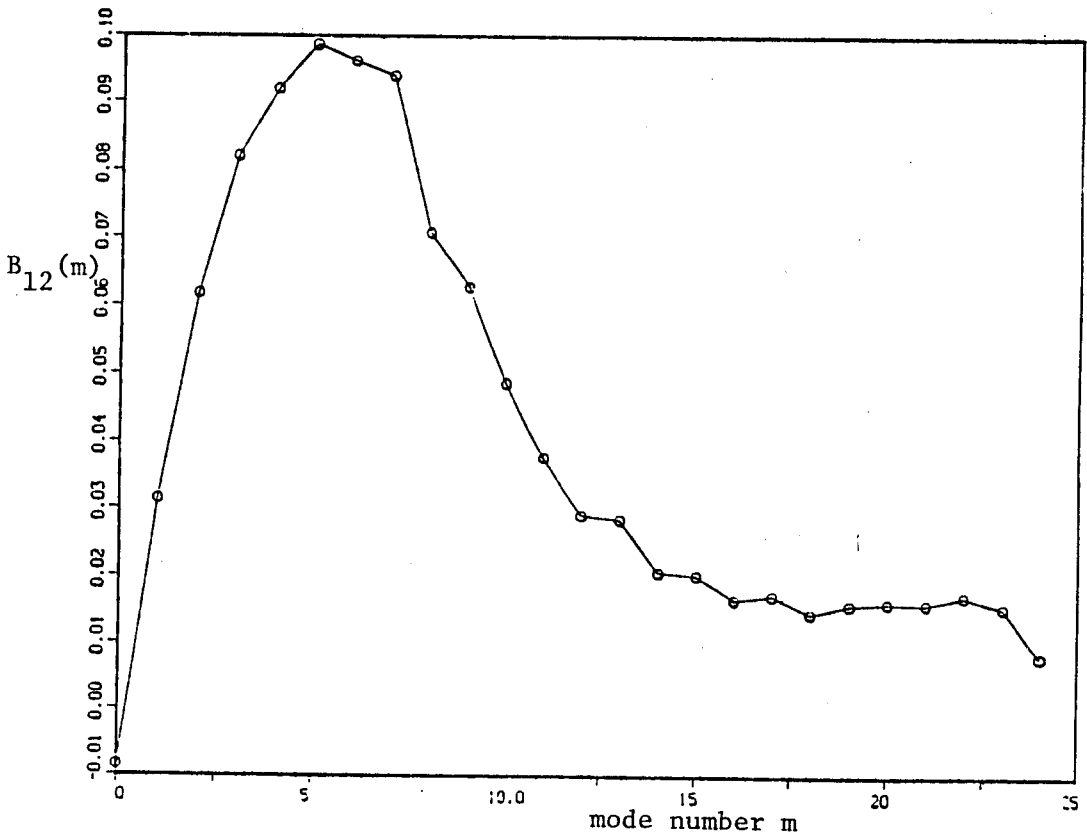


Figure 5.4.8(b) $B_{12}(m)$ at $r/D=0.57, x/D=3$

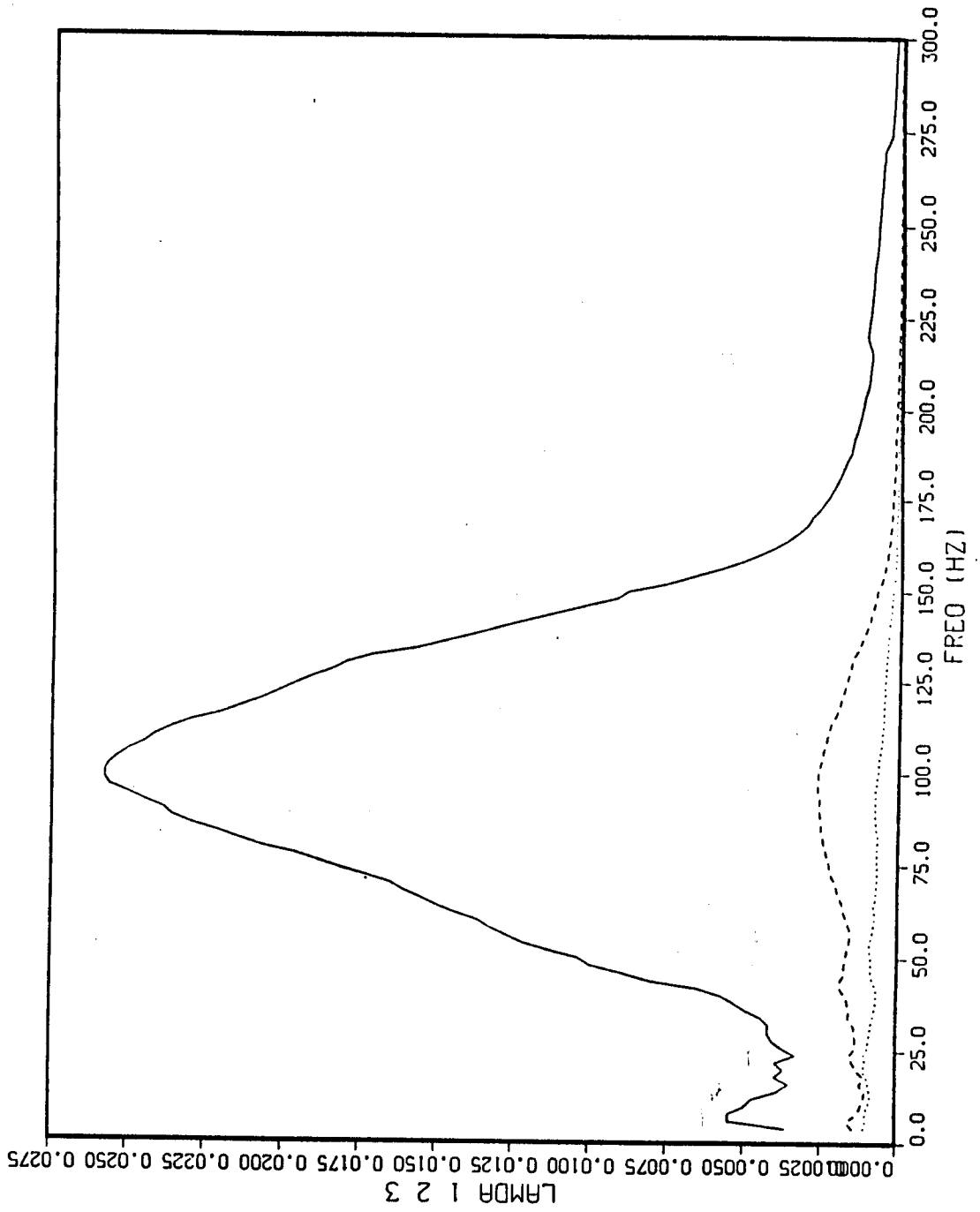


Figure 5.4.9 First 3 eigenspectra, mode 0

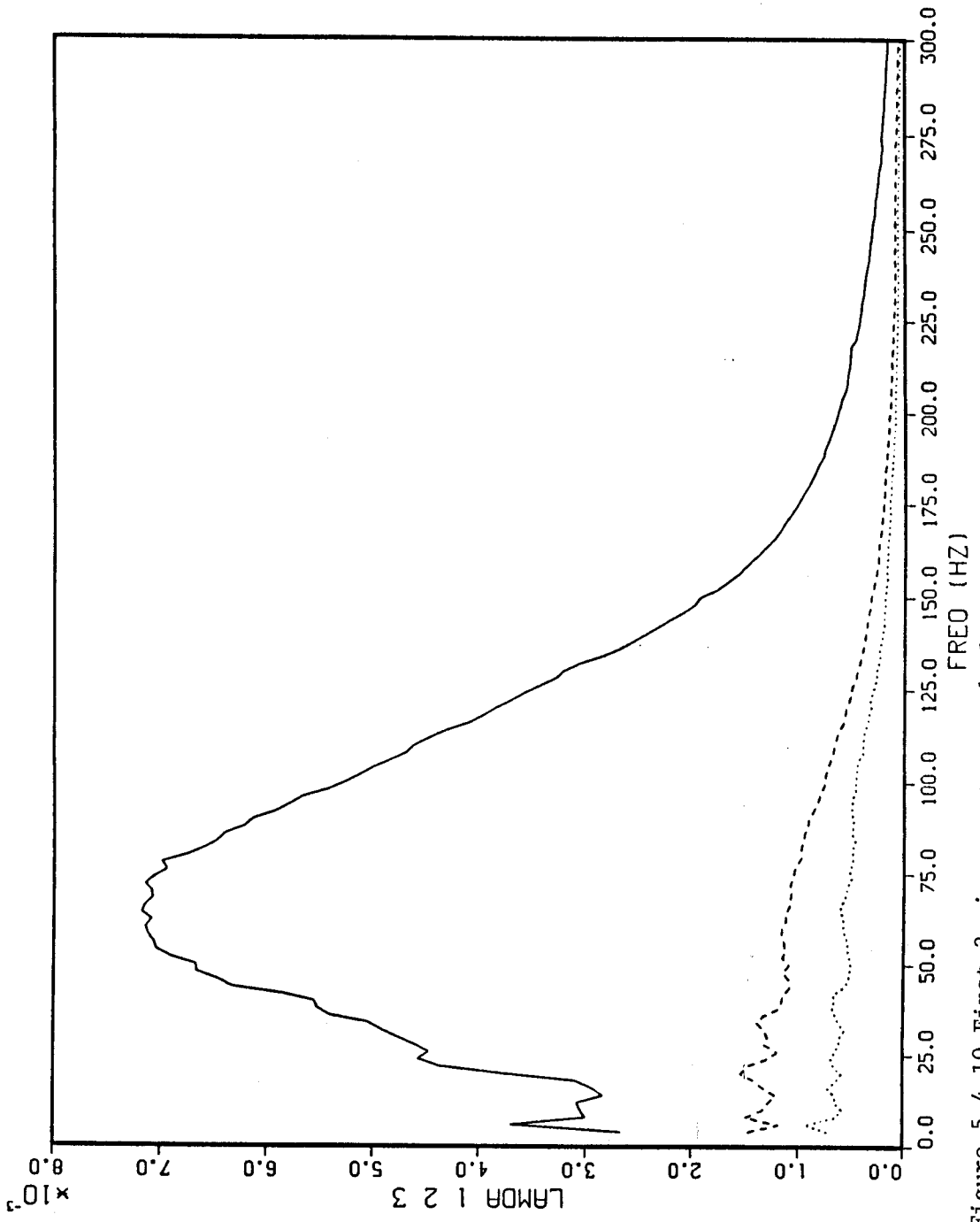


Figure 5.4.10 First 3 eigenspectra, mode 1

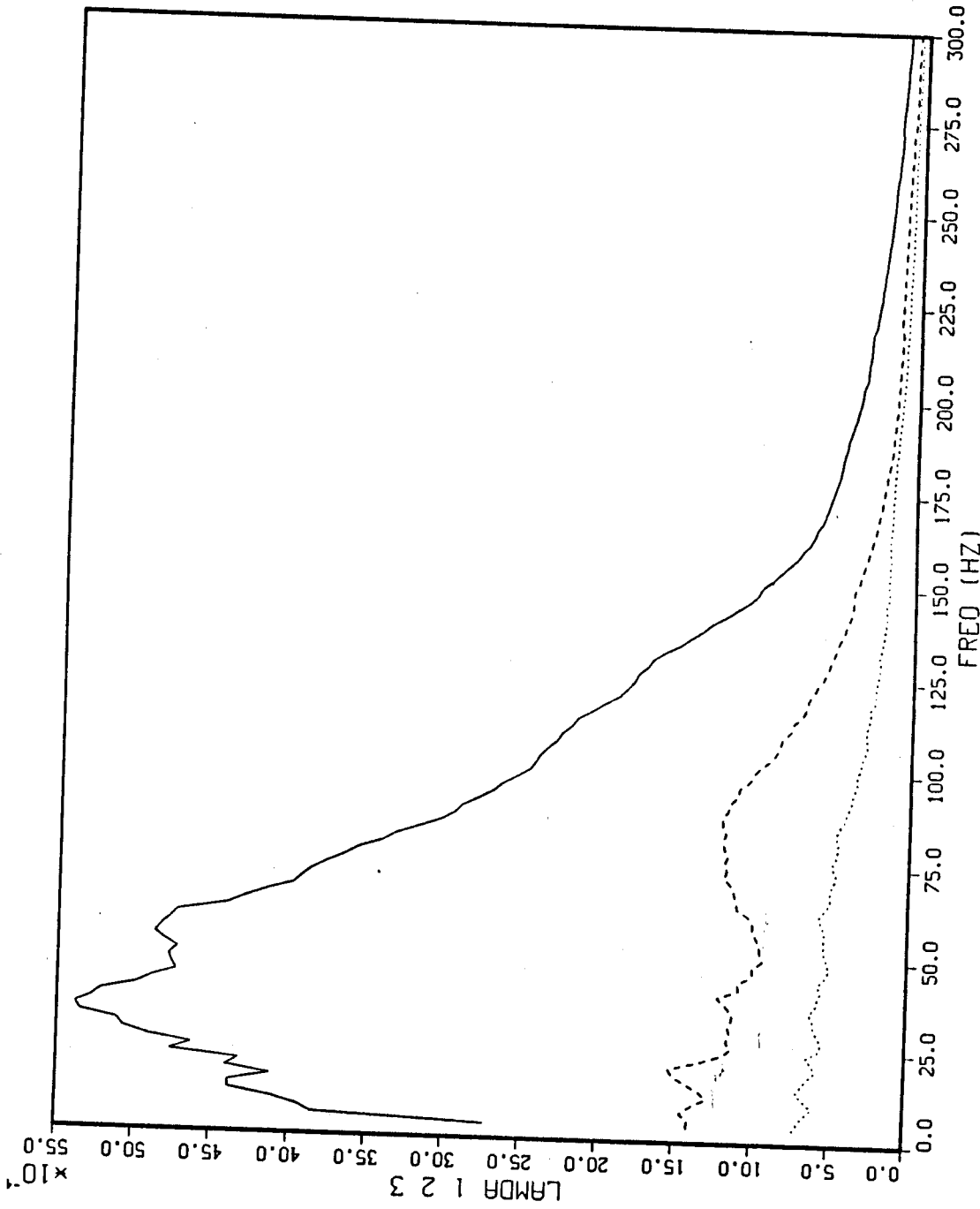


Figure 5.4.11 First 3 eigenspectra, mode 2

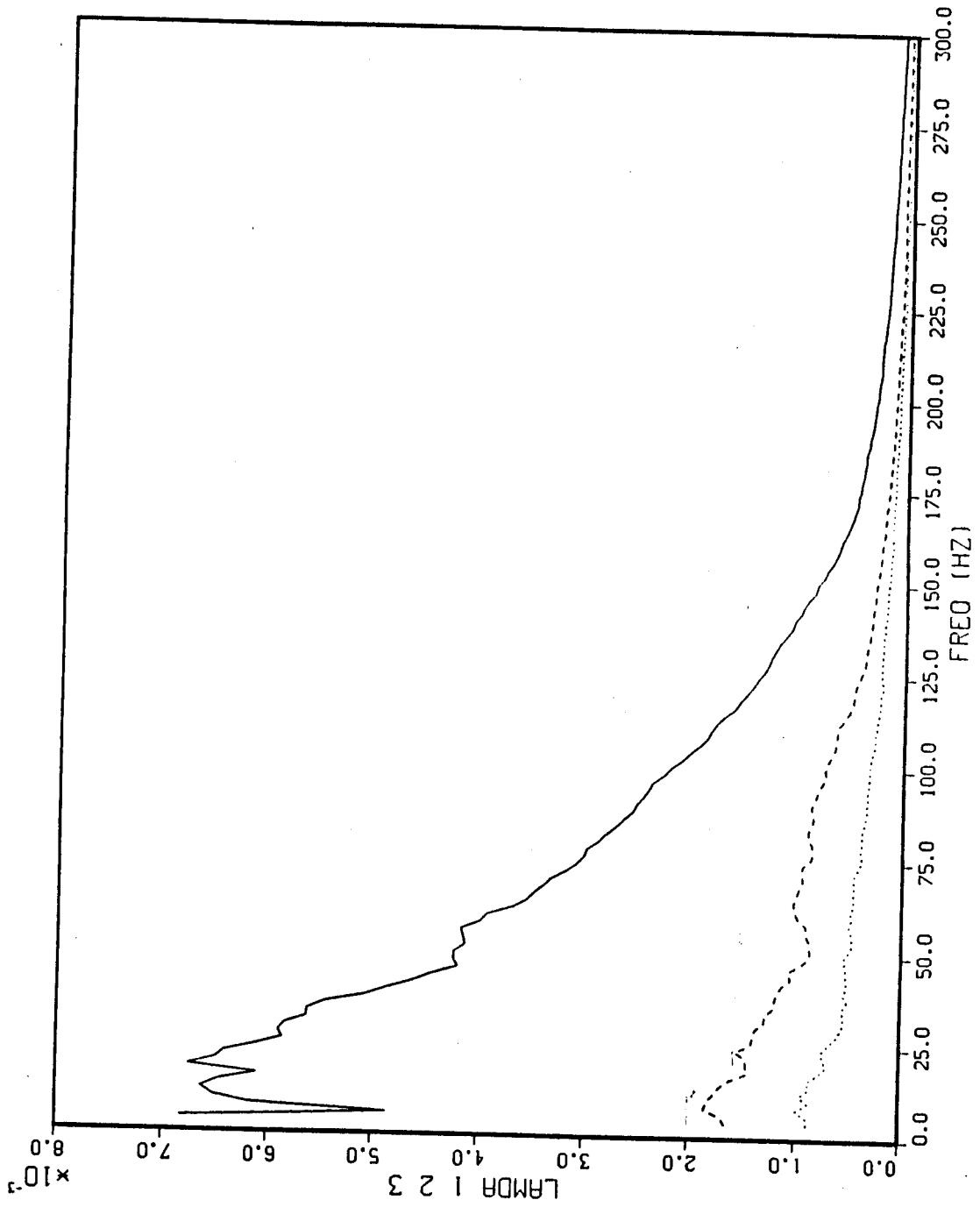


Figure 5.4.1.2 First 3 eigenspectra, mode 3

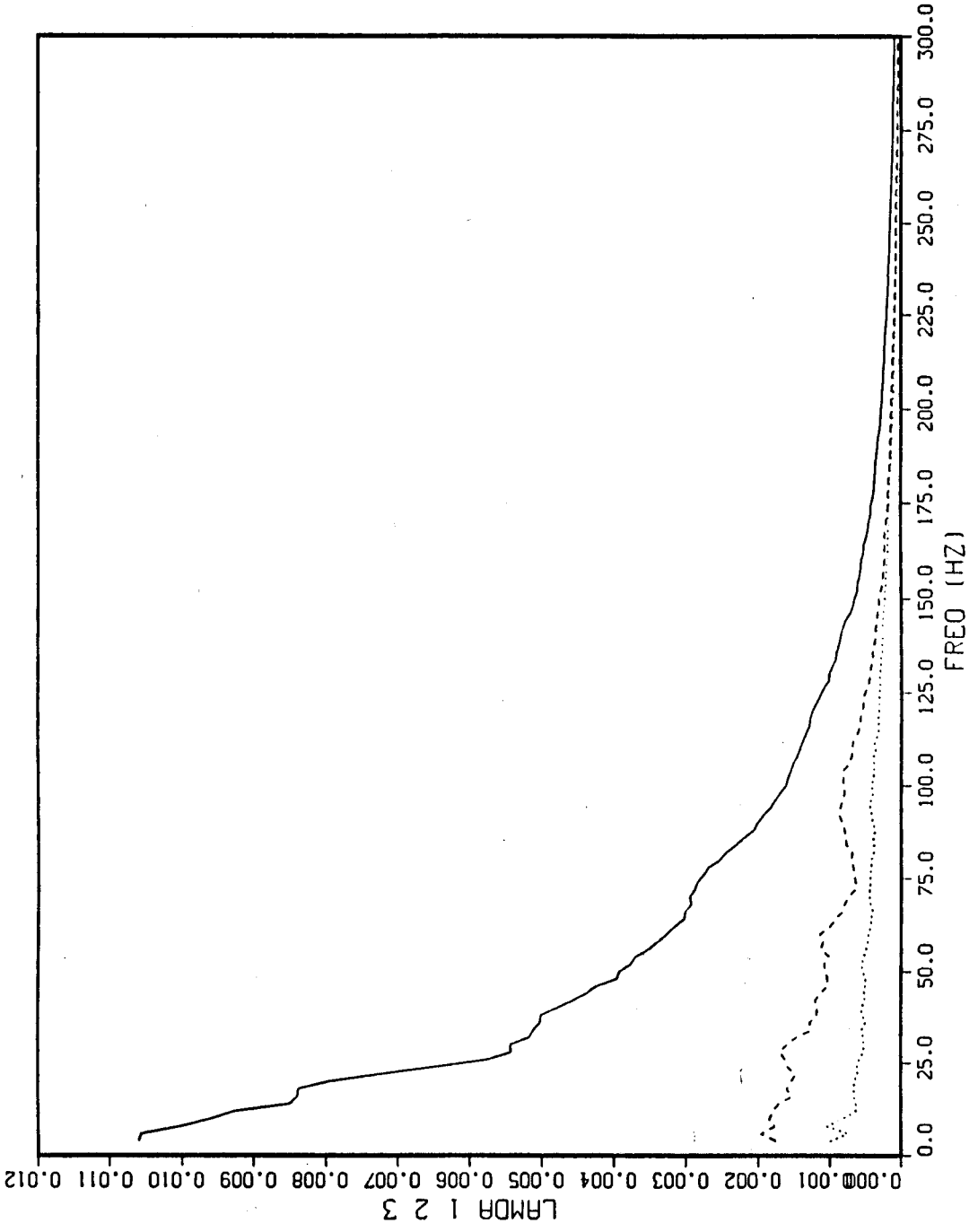


Figure 5.4.13 First 3 eigenspectra, mode 4

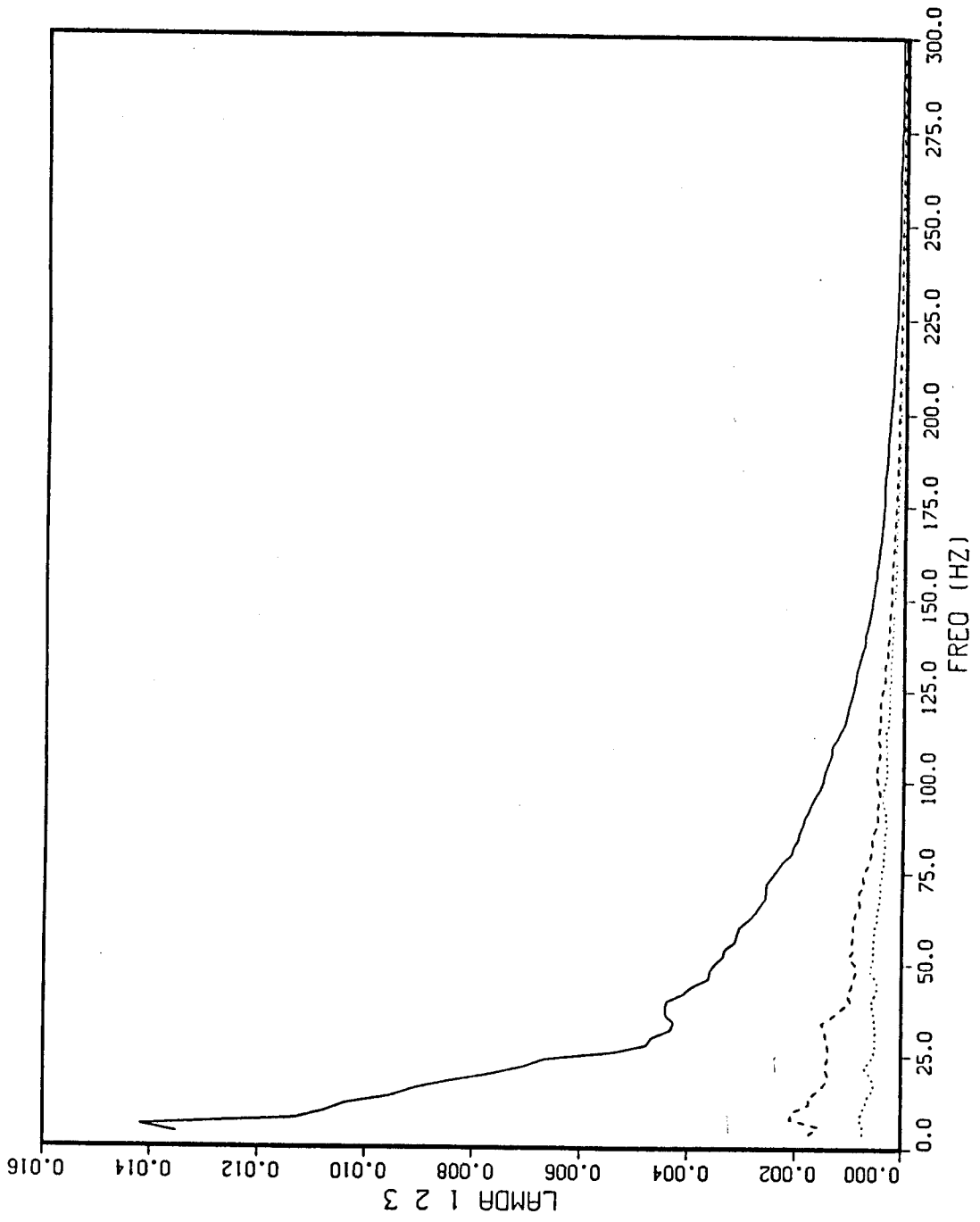


Figure 5.4.14 First 3 eigenspectra, mode 5

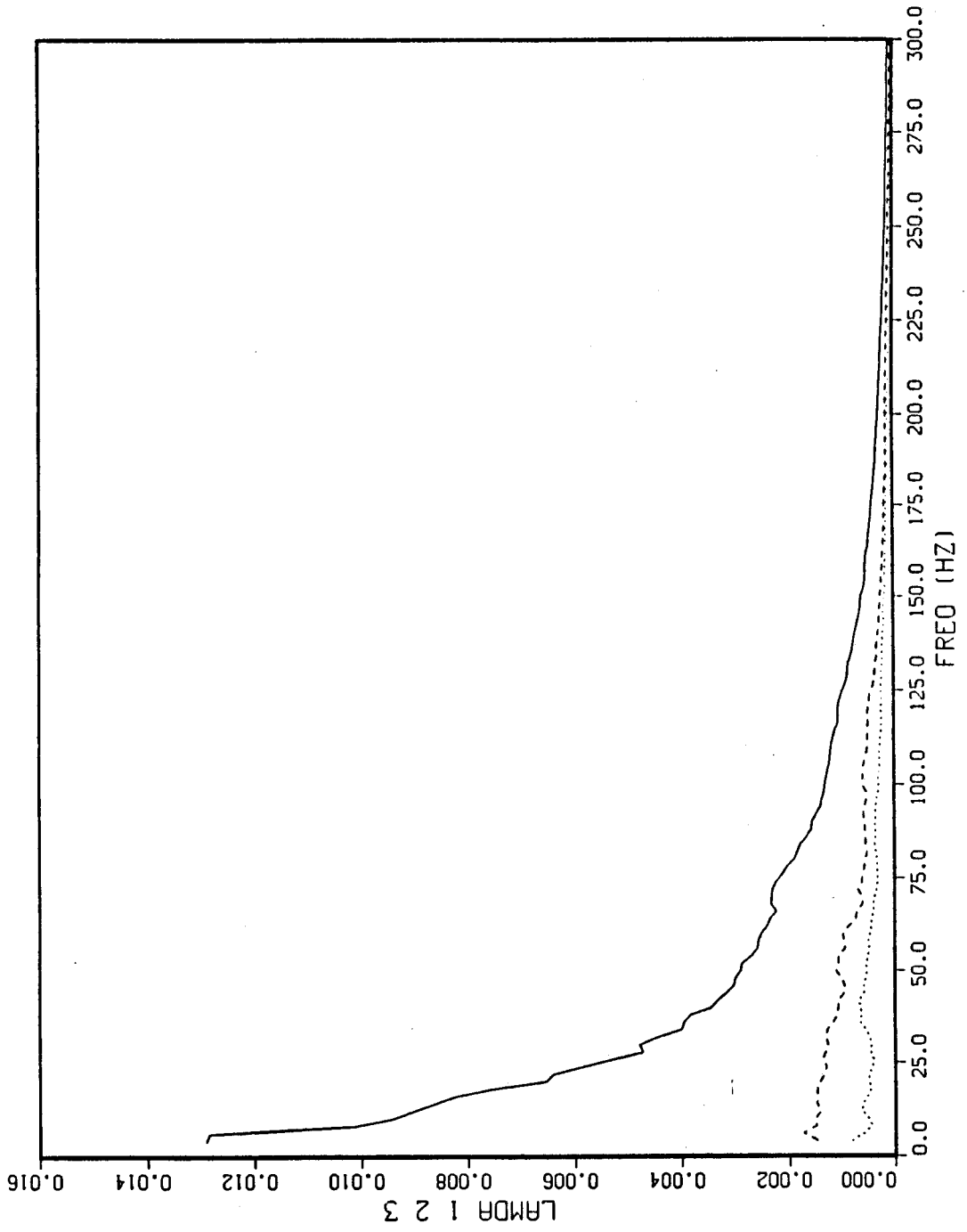


Figure 5.4.15 First 3 eigenspectra, mode 6

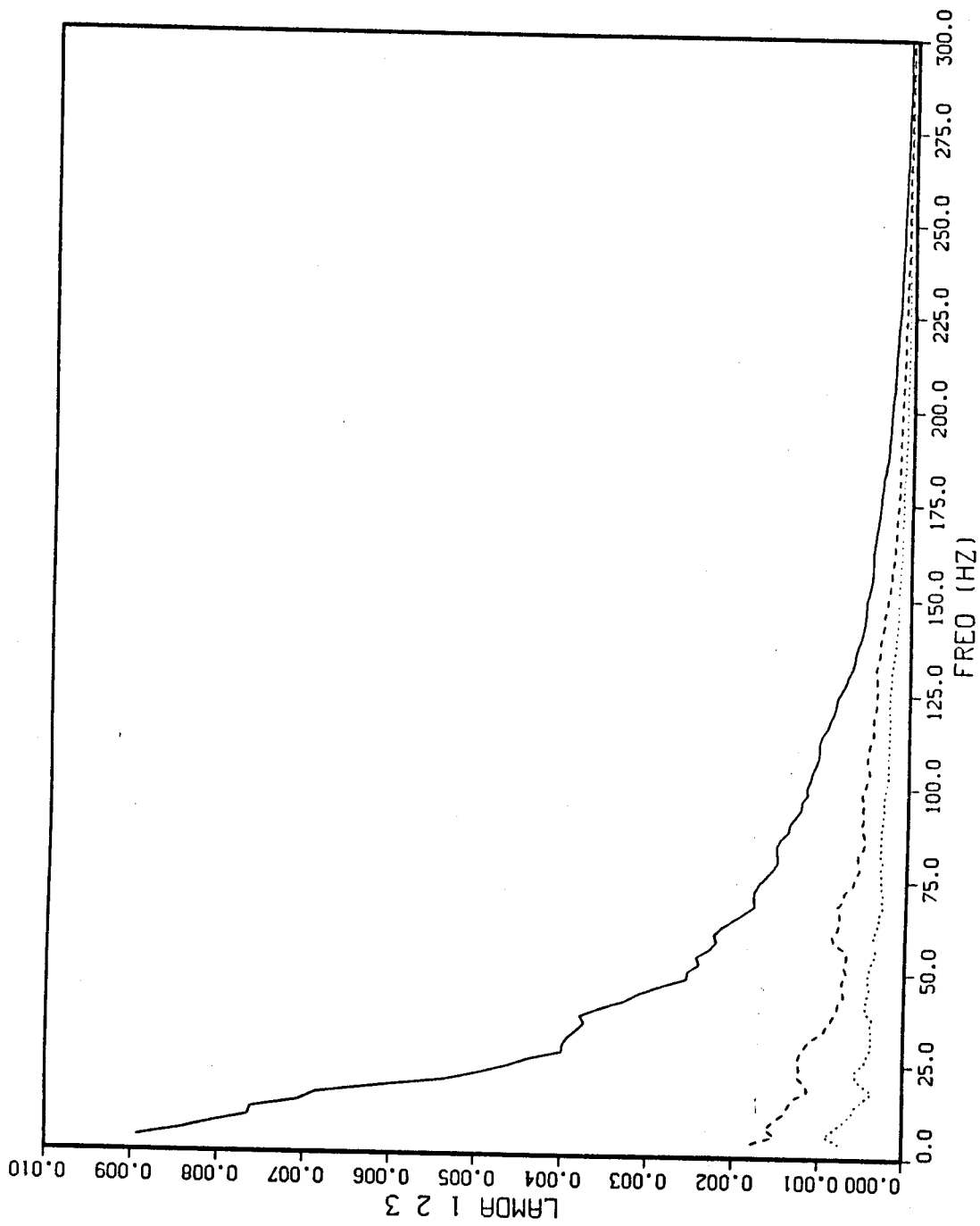


Figure 5.4.16 First 3 eigenspectra, mode 7

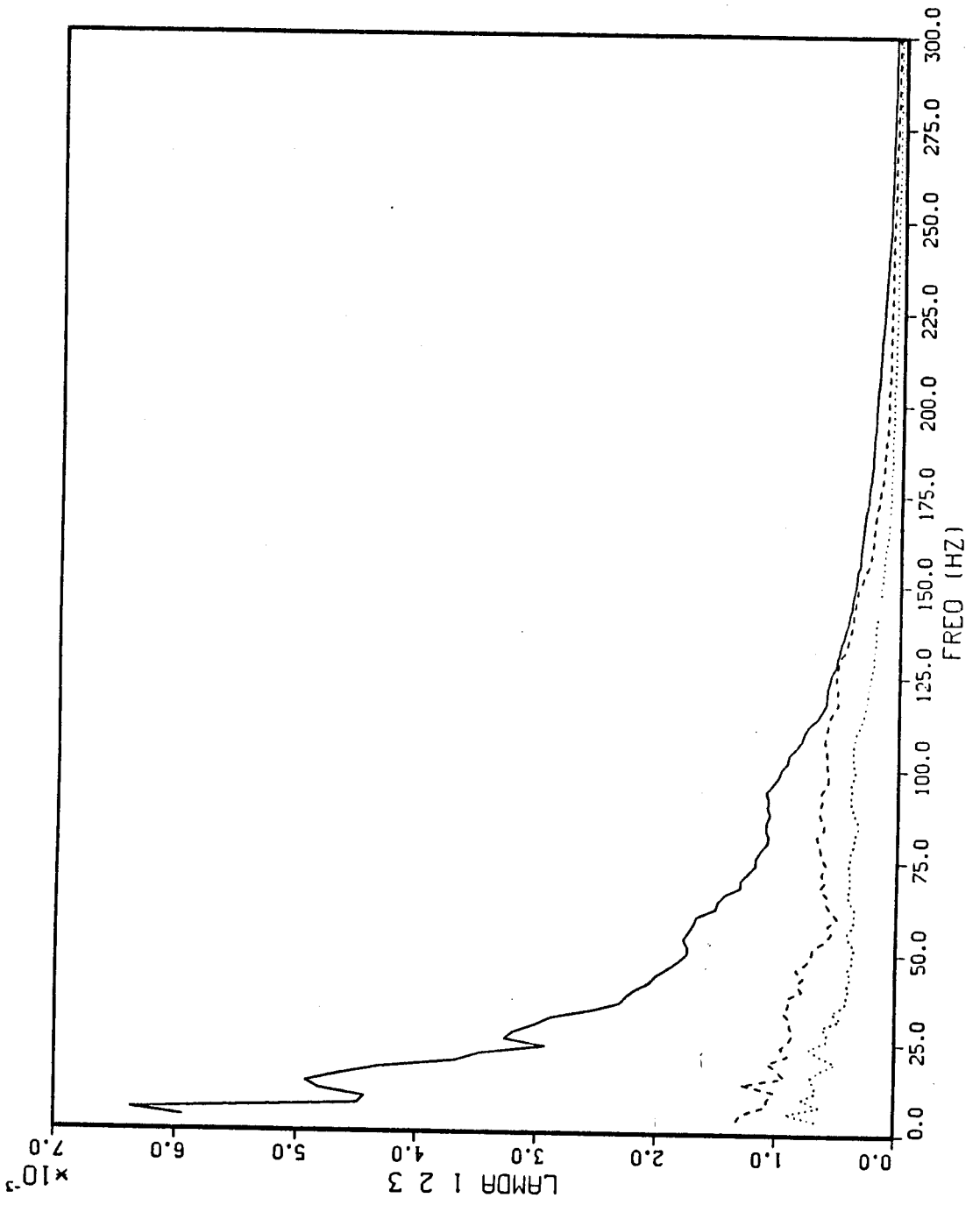


Figure 5.4.17 First 3 eigenspectra, mode 8

5.4.3 Phase 3 and 4 - Discussion

The preference for the 4th, 5th and 6th modes as seen in Figures 5.4.7 and 5.4.8 and in section 5.3 is intriguing. A 6th-lobe preference (although weak) was seen by Sreenivasan (1984) at a position closer to the potential core at $x/D=1$. A detailed stability analysis for vortex rings has been carried out by Widnall and Sullivan (1973). From this analysis the number of preferential lobes is seen to depend on the circulation as well as on the ratio of the vortex core radius to the ring radius. Under certain combinations of the above conditions they noticed a 6th-lobe preference. Thus 6th-lobe preference noticed here is not inconsistent with the results from Widnall and Sullivan (1973).

An additional point of considerable interest is the fact that the uv azimuthal correlation are strongly correlated near the potential core (see Figure 5.4.3), become broadband as one proceeds toward the center of the mixing layer (see Figure 5.4.6), and then become more correlated as one proceeds toward the outside of the shear layer (see Figure 5.4.8). This indicates either that the incoherent turbulence is convected toward the center of the large structure, or is generated there.

5.4.4 A Proposed Mechanism

The previous discussion suggest the following mechanism for turbulence production which consists of four stages. These four stages are shown in Figure 5.4.18. Vortex ring-like concentrations arise from an instability of the base flow, the induced velocities from vortices which have already formed providing the perturbation for those which follow. These pairs of rings then behave like the text-

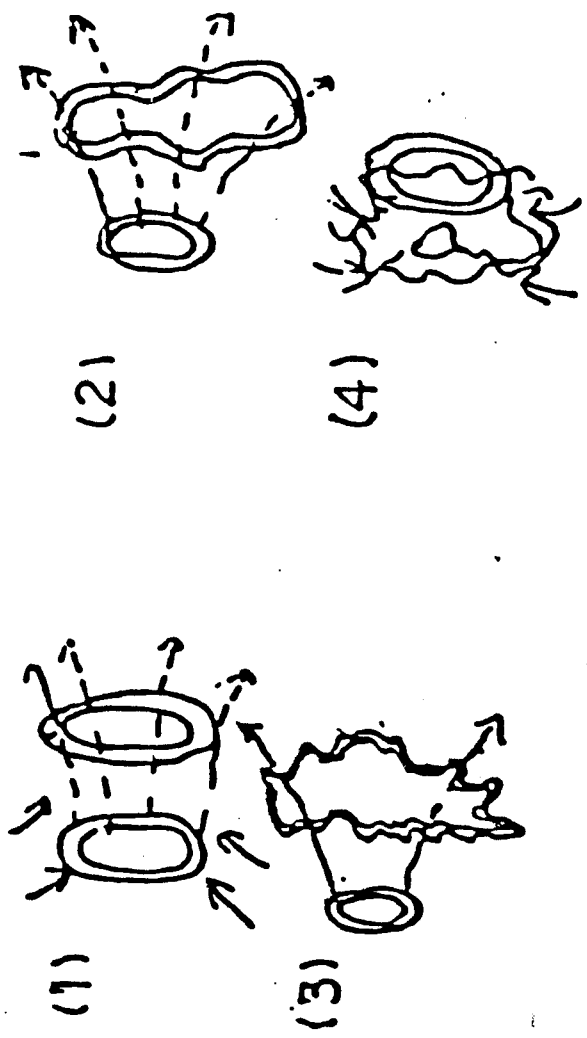


Figure 5.4.18. The Proposed 4 stages of turbulence production.

book examples of inviscid rings, the rear vortex ring overtaking the vortex ring ahead of it, the rearward vortex being reduced in radius and the forward are being expanded by their mutual interaction. The rearward ring is stabilized by the reduction in its vorticity (by compression) thus the predominance of the 0th mode on the high speed side (core region). The forward ring has its vorticity increased by stretching as it expands in radius. This narrowing of its core while the radius is expanding causes the vortex to become unstable (as in the Widnall-Sullivan mechanism mentioned above), thus the predominance of the 4-6 modes from the center of the shear layer outwards. The continued effect of the rearward vortex on the forward one and the now highly distorted ring interaction with itself, accelerates the instability until its vorticity is now entirely in small scale motions, in effect an energy cascade from modes 4-6 all the way to dissipative scales. This incoherent turbulence is swept from the outside where it has been carried, back to the center of the mixing layer as the still-intact rearward vortex passes. It is this collecting of the debris, both small-scale vorticity and fluid material, which has been recognized as "pairing". Thus pairing is not a mechanism as has often been claimed, but simply a phenomenon which marks the end of the life cycle of a large eddy. The entire process is repeated as a new rearward vortex overtakes and destabilizes the one ahead of it.

The above sequence is consistent with all of the observations of this experiment and those of others (v. Hussain 1986). The only missing piece of information is to experimentally establish the sequencing of the events, a task for a future decomposition which

will include the streamwise-variable dependence (i.e. x).

CHAPTER 6

CONCLUSION

The orthogonal decomposition has been shown to be remarkably efficient at organizing data (i.e. 7 x 7 grid appears adequate), and the instantaneous properties of the random signal have not been lost, only organized. So efficient has the scheme been at organizing the energy that only a few terms in the inhomogeneous direction were needed to completely represent the instantaneous signal.

The orthogonal decomposition is seen to require only 3 terms to represent the kernel of the integral in the inhomogeneous direction (across the shear layer) while the harmonic decomposition applied in the azimuthal direction requires considerably more terms. This would suggest that the prevailing view of the large eddy as an axisymmetric vortex be modified somewhat. Instead of only using the 0th azimuthal mode, at least the 4th, 5th and 6th modes should be included in the definition. This would increase the energy content of the big eddy, and give a more realistic physical view of it.

The basic features of the azimuthal large structure obtained in phase 4 were the same as those obtained with the streamwise only correlation (phase 3). In particular the strong correlation and dominance of the 0th mode near the potential core and the preference for the 4th, 5th and 6th modes elsewhere. This would imply that, as far as the large scale structure is concerned, that the streamwise azimuthal correlations would be an adequate description. The addition of the Reynolds stress and radial azimuthal correlations, however, give additional insight into what is happening across the shear layer,

in particular the mechanism of the breakup of the structure.

The eigenspectra extracted using the data base from phase 4 show the same basic characteristics as those extracted from the streamwise only decomposition. The shapes of the particular eigenspectra are essentially identical. The only measurable difference between the eigenspectra is in their respective amplitudes, those from the latest data being higher. This is to be expected because the eigenspectra are essentially the total energy integral across the shear layer, and with this latest data there is the additional contribution to the total energy from the v component of velocity.

A mechanism for the life cycle of coherent structures and for turbulence production in the axisymmetric jet mixing layer has been proposed which accounts for the observed phenomena and is amenable to dynamical analysis using the equations of motion. It will be interesting to see if the details can in fact be confirmed by a direct application of the decomposition to the equations of motion. If so, we may at long last have a detailed example of how Reynolds stress acts to remove energy from the mean flow and distributes it to all scales of motion.

CHAPTER 7

Recommendations for Further Study

Up to this point in the discussions there has not been an attempt to demonstrate how to reconstruct the large eddies in physical space. When the stationary variable time is transformed to frequency using the Fourier transform the visibility of the structure in the Fourier domain depends on the bandwidth of the random coefficients calculated from equation (5.1.4) (v.Arndt and George (1973)). For low Reynolds number flow there are only a few dominant Fourier modes so that the structure is visible or distinct, however, with high Reynolds number flow there are many Fourier coefficients. Since the lifetime of the "groups" is inversely proportional to its bandwidth, the actual structure becomes more fleeting as the Reynolds number increases. Therefore there is a need for some method to organize or sequence the occurrence of these structures in a high Reynolds number flow. Lumley (1967, 1970) suggested using the shot noise decomposition to overcome this problem.

The shot noise effect can be illustrated by the randomly varying intensity of a flow of electrons from cathode to anode in a vacuum tube. The signal produced by this stream of electrons is random in nature. The arrival of a single electron at the anode would, however, result in a signal characteristic of an individual event. The signal which results from the arrival of many electrons at random times is then a random superposition of these characteristic signals. It can be seen then that, while the overall signal is indeed random, it is composed of characteristic signals which are deterministic and occur at random times. The shot noise decomposition provides one means of

determining the nature of hypothesized individual events from measurements of the spectrum of the random signal.

In extending these ideas to a homogeneous or stationary turbulent flow field it is supposed that the random velocity field is composed of characteristic signals or 'eddies', occurring at random times in a stationary flow (or at random positions in a homogeneous flow). Upon randomly superposing (or sprinkling the flow with) these eddies the random velocity field is realized.

These concepts were applied to the time direction using the streamwise velocity measurement from phase 1 (Glauser et al. 1987) where a zero phase reconstruction of the supposed large eddy was performed (see Figure 7.1). . The phase relationship or sequencing of the structure is unobtainable from second order statistics. Lumley (1980) suggested using the bi-spectrum, (Rosenblatt (1966)) to achieve the desired sequencing.

Herzog (1986) has shown, however, that within the domain of the shot noise expansion, there does not exist a description of a typical eddy and its distribution of strength in space and time which represents all third order statistics (in particular of the bi-spectrum) of the random coefficients associated with the dominant eigenmode. He was able though to restrict the functional form of the phase relationship among the Fourier modes by utilizing requirements of real values and symmetry of the large eddy so that the influence of different phase relationships could be investigated. Herzog found that the assumption of zero phase led to the most compact form of the velocity field of the eddy. Any introduction of a moderate phase shift between the Fourier modes lead to attenuation of the eddy but

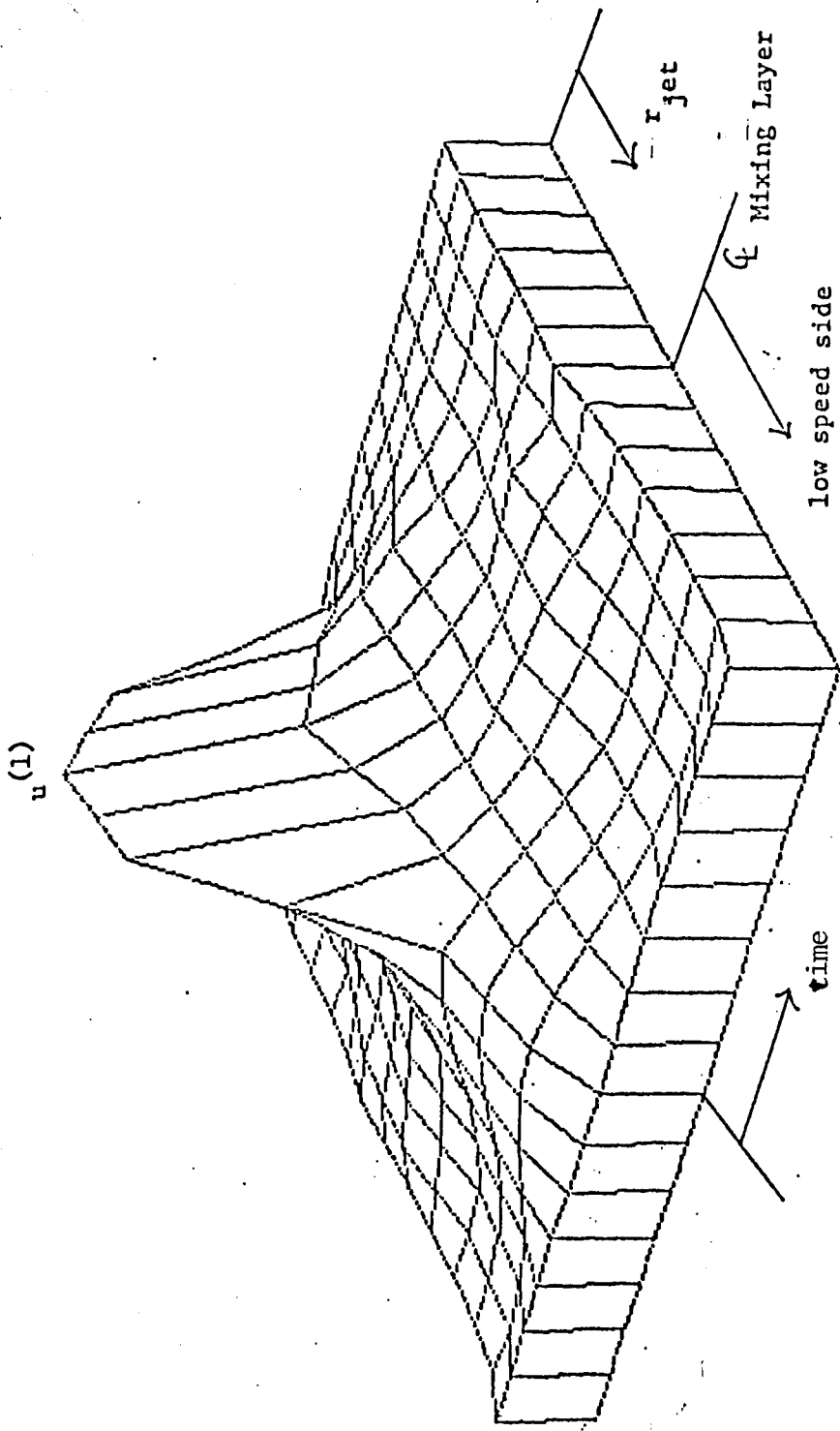


Figure 7.1 Characteristic eddy calculated from shot-noise decomposition(v. Glauser et al.(1987))

did not change its geometric shape.

In an attempt to deal with the phase problem Aubry et al. (1986) suggests a slight modification to the original orthogonal decomposition that leaves the random coefficients (v. equation (5.1.3)) as a function of time. This alternative expansion can then be substituted in the Navier-Stokes equations in order to recover the phase information carried by the coefficients. This approach has been implemented by Aubry et al. (1986) with some success using the eigenfunctions of Herzog (1986). It would be interesting to implement these concepts using the eigenfunctions obtained from the jet, and such studies will be carried out in the future.

To this point it has been assumed that the coherent structure is a unique event. However, the discussion in Section 5.4 (of a possible mechanism) would suggest that these structures interact with one another (how much interaction is still an open question) implying that in order to model the dynamics properly these interactions must be accounted for. The best way to obtain more quantitative information about the interaction of these structures would be to repeat the experiment, only now adding the streamwise variation. This would give the complete space time evolution of these structures. How to properly sequence these interacting structures is not obvious but perhaps an eduction scheme somewhat like that suggested by Hussain (1986) used in conjunction with a velocity field reconstructed from the orthogonal decomposition may be fruitful.

REFERENCES

- Adrian, R. (1985) University of Illinois-Urbana (private communication).
- Arndt, R.E.A. and Lumley, J.L. (1974) Investigation of the Large Scale Coherent Structure in a Jet and Its Relevance to Jet Noise. Proc. Second Interagency Symp. on Univ. Research in Transportation Noise, North Carolina State Univ., Raleigh, NC, June 5-7.
- Aubry, N., Holmes, P., Lumley, J.L. and Stone, E. (1986) The Dynamics of Coherent Structures in the Wall Region of a Turbulent Boundary Layer, Cornell University Report No. SDA8615.
- Baker, T.H. (1977) The Numerical Treatment of Integral Equation. Clarendon, Oxford, New York.
- Bakewell, P. and Lumley, J.L. (1967) Viscous Sublayer and Adjacent Wall Region in Turbulent Pipe Flow. Phys. Fluids 10(3) No. 9: 1880-1889.
- Beuther, P.D., Shabbir, A. and George W.K. (1987) X-wire Response in Turbulent Flows of High Intensity Turbulence and Low Mean Velocities. 1987 ASME Symp. on Thermal Anamometry. June 14-17, Cincinnati, OH. (ed. Stock, D.E.)
- Bradshaw, P., Ferris, D.H., and Johnson, R.F. (1964) Turbulence in the Noise-Producing Region of a Circular Jet. J. Fluid Mech. 19, 591.
- Brown, G.L., Roshko, A. (1974) J. Fluid Mech., 64, 775.

- Buchhave, P. (1979) The Measurement of Turbulence with the Burst-Type Laser Doppler Anemometer—Errors and Correction Methods. PhD Dissertation, University at Buffalo, SUNY.
- Cantwell, B.J. (1981) Organized Motion in Turbulent Flow. *Ann. Rev. Fluid Mech.* 13, 457.
- Champagne, F.H., Sleicher (1967) *JFM*, 28, 177.
- Crow, S.C., Champagne, F.H. (1971) Orderly Structure in Jet Turbulence, *J. Fluid Mech.* 48, 547.
- Davies, P.O.A.L., Barratt, M.J., Fisher, M.J. (1963) The Characteristics of Turbulence in the Mixing Region of a Round Jet, *J. Fluid Mech.* 15, 337.
- George, W.K. (1978) Processing of Random Signals. *Proc. of the Dynamic Flow Conf.*, 1978.
- George, W.K., Beuther, P.D. Shabbir, A. (1987) Polynomial Calibrations for Hot Wires in Thermally-Varying Flows. *ASME Symp. on Thermal Anemometry*, June 14-17, Cincinnati, OH (ed. D. Stock).
- Glauser, M.N. and George, W.K. (1987) Orthogonal Decomposition of the Axisymmetric Jet Mixing Layer Including Azimuthal Dependence. *Advances in Turbulence*, Springer-Verlag (eds. G. Comte-Bellot and J. Mathieu).

- Glauser, M.N. and George, W.K. (1987) An Orthogonal Decomposition of the Axisymmetric Jet Mixing Layer Utilizing Cross-Wire Velocity Measurements. Proc. 6th Symp. Turbulent Shear Flows, Toulouse, France, Sept. 7-9.
- Glauser, M.N., Leib, S.J. and George, W.K. (1987) Coherent Structures in the Axisymmetric Jet Mixing Layer. Turbulent Shear Flows 5, Springer-Verlag.
- Grant, H.L. (1958) The Large Eddies of Turbulent Motion, J. Fluid Mech., 4, 149.
- Herzog, S. (1986) The Large Scale Structure in the Near-Wall Region of Turbulent Pipe Flow. PhD Dissertation, Cornell University.
- Hussain, A.K.M.F., Clark, A.R. (1981) J. Fluid Mech., 109, 263.
- Hussain, A.K.M.F. (1986) Coherent Structure and Turbulence. J. Fluid Mech. V. 173, 303-356.
- Laurence, J.C. (1956) Intensity, Scale and Spectra of Turbulence in Mixing Region of Free Subsonic Jet, NACA Report No. 1292.
- Leib, S.J., Glauser, M.N. and George, W.K. (1984) An Application of Lumley's Orthogonal Decomposition to the Axisymmetric Turbulent Jet Mixing Layer. Proc. 9th Rolla Symp.
- Lemmerman, L.A. (1976) Extraction of the Large Eddy Structure of a Turbulent Boundary Layer. PhD Dissertation, University of Texas at Arlington.

- Lighthill, M.J. (1964) Introduction to Fourier Analysis and Generalized Functions. Cambridge University Press.
- Long, D.F. and Arndt, R.E.A. (1985) The Orthogonal Decomposition of Pressure Fluctuations Surrounding a Turbulent Jet. Proc. 5th Symp. Turbulent Shear Flows, Cornell University.
- Lumley, J.L. (1967) The Structure of Inhomogeneous Turbulent Flows. In Atm. Turb. and Radio Wave. Prop., (Yaglom and Tatarsky, ed.) Nauka, Moscow, 166-1,8.
- Lumley, J.L. (1970) Stochastic Tools in Turbulence, Academic Press, New York.
- Lumley, J.L. (1981) Coherent Structures in Turbulence. Transition and Turbulence, edited by R.E. Meyer, Academic Press, New York, 215-242.
- Lumley, J.L. (1982) Invited Talk, 35th Annual Amer. Phys. Soc., Div. Fluid Dynamics Meeting, Rutgers Univ., New Brunswick, NJ.
- Moin, P. (1984) Probing Turbulence via Large Eddy Simulation. AIAA 22nd Aerospace Sciences Meeting.
- Oppenheim, A.V., Willsky, A.S. and Young, I.T. (1983) Signals and Systems. Prentice-Hall Signal Processing Series.
- Otnes, R.K. and Enochson, L.D. (1978) Applied Time Series Analysis. Wiley Interscience.
- Payne, F.R. (1966) Large Eddy Structure of a Turbulent Wake. PhD Dissertation, Pennsylvania State University.

Rosenblatt, M. (1966) Computation and Interpretation of kth Order Spectra Spectral Analysis of Time series, Wiley (1966); 153-188.

Sreenivasan, K.R. (1984) The Azimuthal Correlations of Velocity and Temperature Fluctuations in an Axisymmetric Jet. Phys. Fluids, 27, (4).

Stromberg, J.L., McLaughlin, D.K. and Troutt, T.R. (1980) Flow Field and Acoustic Properties of a Mach Number 0.9 Jet at a Low Reynolds Number. Journal of Sound and Vibration.

Tan-atichat, J. and George, W.K. (1985) Use of Computer for Data Acquisition and Processing. Handbook of Fluids and Fluid Machinery. John Wiley Sons, Inc. (Allen E. Fuhs, ed.)

Townsend, A.A. (1956) The Structure of Turbulent Shear Flow. Cambridge University Press.

Townsend, A.A. (1976) 2nd Ed. The Structure of Turbulent Shear Flow. Cambridge University Press.

Widnall, S.E. and Sullivan, J.P. (1973) Proc. R. Soc. London Ser. A332, 335.